

Electronic Thesis and Dissertation Repository

10-7-2020 2:30 PM

Chemical Reactions at Metal Surfaces: Functionalization Strategies and Spectroscopic Characterization

Sydney Legge, *The University of Western Ontario*

Supervisor: Lagugné-Labarthet, François, *The University of Western Ontario*

Joint Supervisor: Workentin, Mark, *The University of Western Ontario*

A thesis submitted in partial fulfillment of the requirements for the Master of Science degree in Chemistry

© Sydney Legge 2020

Follow this and additional works at: <https://ir.lib.uwo.ca/etd>

 Part of the [Materials Chemistry Commons](#)

Recommended Citation

Legge, Sydney, "Chemical Reactions at Metal Surfaces: Functionalization Strategies and Spectroscopic Characterization" (2020). *Electronic Thesis and Dissertation Repository*. 7373.
<https://ir.lib.uwo.ca/etd/7373>

This Dissertation/Thesis is brought to you for free and open access by Scholarship@Western. It has been accepted for inclusion in Electronic Thesis and Dissertation Repository by an authorized administrator of Scholarship@Western. For more information, please contact wlsadmin@uwo.ca.

Abstract

Tremendous interest in increasing the control over surface properties has led to high demand for new efficient methods for chemical surface modifications. In this work, several approaches toward surface functionalization are explored, and modified surfaces are subsequently characterized using uniquely suited spectroscopic techniques. In the first part of this thesis, strain-promoted alkyne-azide cycloaddition (SPAAC) reactions are investigated for their potential to precisely tune the surface properties of gold substrates at the monolayer level. The utility of SPAAC reactions in preparing biorecognition interfaces for cell adhesion is then examined. Polarization modulation infrared reflection-absorption spectroscopy is used to characterize adsorbed monolayers and probe the progress of surface SPAAC reactions. In the second section of this thesis, novel plasmonically active metallic substrates are fabricated. These substrates are used to catalyze the plasmon-mediated grafting of diazonium salts onto gold nanoparticle surfaces and are also employed as platforms for surface-enhanced Raman spectroscopy.

Keywords

Surface chemistry, plasmonics, metallic nanostructures, plasmon-mediated chemistry, diazonium salts, surface-enhanced Raman spectroscopy, click chemistry, strain-promoted alkyne-azide cycloaddition, self-assembled monolayers, polarization modulation infrared reflection-absorption spectroscopy

Summary for Lay Audience

The ability to tune the surface properties of materials through chemical modifications is an essential field of study that plays an indispensable role in many applications ranging from nanoelectronics to bioengineering. Fine control over surface chemistry is vital, as the properties and interactions of surfaces on the microscale directly dictate the nature and function of material surface interfaces at the macroscopic level. Thus, there is considerable demand for new and improved surface modification techniques that allow for precise tailoring of material surfaces. Currently, there exists a host of methodologies to manipulate surface chemistry. In this thesis, select surface modification strategies of interest are investigated in detail.

One reaction that has been examined for the development of chemically modified surfaces is a “click” reaction called the strain-promoted alkyne-azide cycloaddition (SPAAC) reaction. Click chemistry, a class of reactions characterized by rapid kinetics, mild reaction conditions, high selectivity, and high efficiency, is well established as a means of surface modification. One of the aims of this research is to employ a variety of SPAAC reactions designed to specifically alter the surface properties of metal substrates, and to explore the applicability of SPAAC reactions in the preparation of surfaces for biochemical applications. Polarization modulation infrared reflection-absorption spectroscopy (PM-IRRAS), a specialized type of infrared spectroscopy developed for the study of monolayers on reflective surfaces, is used to detect and characterize the modified substrates.

Localized surface plasmon resonance (LSPR) occurs when a collective oscillation of free electrons in a metallic nanoparticle (NP) is excited by electromagnetic radiation, often in the range of visible light. As the LSPR decays, high energy electrons are generated at the NP surface. These electrons can participate in and contribute to chemical reactions between organic species on the NP surface. Activation of chemical reactions via plasmon-driven pathways is a relatively new concept that remains largely unexplored. The second portion of this thesis focuses on designing and creating LSPR-supporting substrates and using these substrates to activate chemical reactions via plasmonic catalysis. The substrates are then used to perform surface-enhanced Raman spectroscopy measurements for surface characterization.

Co-Authorship Statement

This thesis contains materials from a published paper. Dr. François Lagugné-Labarhet and Dr. Mark Workentin are the corresponding authors of the paper and were responsible for the supervision of Sydney Legge throughout her studies.

Chapter 3 contains material from a published manuscript that was co-authored by Sydney Legge, Dr. Wilson Luo, Johnny Luo, Dr. François Lagugné-Labarhet, and Dr. Mark Workentin (*Langmuir*, **2020**, *36*, 1014-1022). Sydney Legge and Dr. Wilson Luo contributed equally to the writing and revision of the manuscript. The manuscript was edited by Sydney Legge, Dr. Wilson Luo, Dr. François Lagugné-Labarhet, and Dr. Mark Workentin. All experiments in the publication were performed by Sydney Legge and Dr. Wilson Luo. Sydney Legge was responsible for experimental work including self-assembled monolayer (SAM) assembly, acquisition of polarization modulation infrared reflection-absorption spectroscopy (PM-IRRAS) data, and Au mirror fabrication. Dr. Wilson Luo was responsible for synthesis of organic compounds, acquisition of nuclear magnetic resonance (NMR) spectra, SAM assembly, and contact angle measurements. Cell adhesion studies with human fibroblast cells and fluorescence microscopy measurements of adhered cells were performed through collaboration with Dr. David O’Gorman and Johnny Luo of the Western University Department of Biochemistry.

All experiments in Chapter 4 were performed by Sydney Legge. Chapter 4 was written and revised by Sydney Legge and edited by Dr. François Lagugné-Labarhet and Dr. Mark Workentin. The scanning electron microscopy (SEM) images and visible – near-infrared absorption spectra presented in Chapter 4 were collected by Alex Therien.

Acknowledgments

First and foremost, I must sincerely thank my supervisors Dr. François Lagugné-Labarthe and Dr. Mark Workentin. My graduate studies have been a deeply rewarding and enriching experience and I would not be the researcher that I am today were it not for you both. I have learned an incredible amount from each of you inside and outside of the lab and your advice, mentorship, and guidance has helped me to become a better scientist. You have shown me the value of hard work and dedication, taught me to be confident in my work and in communicating my ideas, and challenged me to pursue new and exciting avenues of research. Thank you very much for the opportunity to conduct this research and for your continued support, patience, and understanding over the years.

I would also like to express my profound gratitude toward all of the past and present members of the Workentin and FLL groups whom I have had the pleasure of knowing. I will extend a special thanks to Workentin group member Dr. Wilson Luo with whom I collaborated closely on research projects before and during my graduate studies. I am deeply grateful for your hard work, optimism, and impressive skills and knowledge as a chemist. I could not have completed this degree without you. I also want to thank Dr. Greg Wallace, veteran FLL group member and my first mentor when I joined the FLL group as an undergraduate student. Your drive and passion for research and your innovative thinking were and continue to be an inspiration to me in my own work. I strive to be a scientist that is up to your standard. Lastly, I must thank Workentin group members Kyle Classen, Justin Park, and Raj Vasdev, and FLL group members Lauren Katz, Alex Therien, Nina Culum, Kara Ly, Leila Mazaheri, Pooneh Farhat, Maria Olivia Avilés, and especially Danielle McRae – Our afternoon teatime breaks (3 PM sharp!) kept me sane. And I'm sure the 10 AM tea breaks would have had the same effect if I had ever bothered to show up in time for them.

I am very grateful to Tim Goldhawk and Dr. Todd Simpson of the Western Nanofabrication Facility for the role that they played in facilitating my research. Thank you for your invaluable expertise and assistance in nanofabrication and imaging.

Over the years I have made many lasting friendships with my fellow group members and with people across the Chemistry Department. Thanks to you I can say that my time in graduate school was never dull. Thank you all for your companionship and special thanks to the Ding group for all the laughs!

Finally, I would like to dedicate this work to all of my family, to my parents, Mark and Christine Legge, to my brother, Milo Legge, to my loving partner, Christian McGhee, and to my best friends, Holly Gilbert and Lucas Toth. With no shortage of kindness and encouraging words, you have all helped me to remember my worth and motivated me to never give up. I turn to you to celebrate my brightest moments and to lighten up my darkest days. You have always believed in me and have always been there when I needed you. All of you have played a part in shaping me into the person that I am today. This work stands as a testament to your unconditional love and support.

Table of Contents

Abstract	ii
Summary for Lay Audience	iii
Co-Authorship Statement.....	iv
Acknowledgments.....	v
Table of Contents	vii
List of Tables	xi
List of Figures	xii
List of Schemes.....	xv
List of Appendices	xvi
List of Abbreviations	xvii
Chapter 1	1
1 General Introduction	1
1.1 Material Surface Modifications: Importance and Applications.....	1
1.2 Methods of Interest for Chemically Modifying Metal Surfaces.....	5
1.2.1 Click Chemistry	5
1.2.2 Plasmon-Mediated Chemistry.....	9
1.3 Scope of Thesis	13
1.4 References.....	14
Chapter 2.....	21
2 Principles of Material Surface Modification and Characterization Techniques	21
2.1 Self-Assembled Monolayers.....	21
2.2 Click Chemistry	23
2.2.1 The Strain-Promoted Alkyne-Azide Cycloaddition.....	25
2.3 Preparation of Patterned Substrates by Microcontact Printing	26

2.4	Plasmons	28
2.4.1	Surface Plasmon Polaritons	29
2.4.2	Localized Surface Plasmon Resonances	30
2.4.3	Plasmon-Mediated Chemistry.....	32
2.5	Raman Spectroscopy.....	37
2.5.1	Surface-Enhanced Raman Spectroscopy	39
2.6	Fourier Transform Infrared Spectroscopy	40
2.6.1	Polarization Modulation Infrared Reflection-Absorption Spectroscopy ..	41
2.7	Summary	43
2.8	References.....	44
Chapter 3.....		58
3	PM-IRRAS Investigation of Photo-Enabled Surface Click Reactions at the Monolayer Level.....	58
3.1	Introduction.....	58
3.2	Methods.....	63
3.2.1	PM-IRRAS Setup and Measurements	63
3.2.2	Gold Substrate Fabrication	64
3.2.3	Synthesis of Organic Molecules	64
3.2.4	SAM Assembly.....	69
3.2.5	Photo-Click Modification of SAMs.....	69
3.2.6	Photopatterning of SAMs	70
3.2.7	Contact Angle Measurements	70
3.2.8	Cell Adhesion Studies.....	70
3.3	Results and Discussion	71
3.3.1	Cyclopropanone SAM Assembly and Characterization	71
3.3.2	Tuning Surface Hydrophobicity by SAM Modification.....	73

3.3.3	Photopatterning of Cyclopropenone SAMs	75
3.3.4	Cell Adhesion Studies on Modified SAMs.....	76
3.4	Conclusions.....	78
3.5	References.....	79
Chapter 4.....		82
4	Plasmon-Mediated Grafting of Diazonium Salts on AuNP-Patterned Surfaces.....	82
4.1	Introduction.....	82
4.2	Methods.....	87
4.2.1	Synthesis of AuNPs	87
4.2.2	Fabrication of PDMS Stamps	88
4.2.3	Patterning of Glass Substrates via Microcontact Printing	88
4.2.4	Visible – Near-Infrared Absorption Measurements.....	90
4.2.5	SAM Formation on AuNP-Patterned Surfaces	91
4.2.6	Plasmon-Mediated Grafting of Aryl Diazonium Salts.....	91
4.2.7	Surface-Enhanced Raman Spectroscopy	92
4.2.8	Scanning Electron Microscopy	93
4.3	Results and Discussion	93
4.3.1	Fabrication of AuNP-Patterned Substrates	93
4.3.2	Validation of AuNP-Patterned Substrates as Plasmonically Active Platforms.....	96
4.3.3	Plasmon-Mediated Grafting of 4-Nitrobenzenediazonium onto AuNP-Patterned Substrates	98
4.4	Conclusions.....	102
4.5	References.....	103
Chapter 5.....		110
5	Conclusions and Outlook.....	110
5.1	References.....	114

Appendix A – Details for PM-IRRAS Spectral Calibration.....	116
References	119
Appendix B – Copyrights	120
Curriculum Vitae	123

List of Tables

Table 3.1: List of important vibrational modes and mode assignments for the PM-IRRAS spectrum of a SAM of cyclopropanone thiol 4 on gold.....	72
Table 4.1: SERS spectral peak assignments for the SAMs of 4-NTP on AuNP-patterned substrates.....	97
Table 4.2: Raman peak assignments for bulk 4-NBD.	100

List of Figures

Figure 1.1: Environmental scanning electron microscopy images of a water droplet on the patterned hydrophobic-hydrophilic hybrid surface (a) before and (b) after evaporation. ¹⁶ (c) High-magnification image of (b). ¹⁶ (d) Diagram of small droplet formation during water evaporation. ¹⁶ The scale bar in (a), (b), and (c) are 10, 10, and 3 μm , respectively. ¹⁶ Adapted with permission from ref. [16]. Copyright 2015 American Chemical Society.....	3
Figure 1.2: (a) Scanning electron microscopy image of triangular gold nanostructures grafted with diazonium salts via plasmonic effects. ⁸² Adapted with permission from ref. [82]. Copyright 2017 American Chemical Society. (b) Schematic representation and scanning electron microscopy image of the gold nanodisk-based two-colour nanoemitter, alongside far-field fluorescence images of the nanoemitter under illumination with X-axis and Y-axis polarization. ⁸³ Adapted with permission from ref. [83]. Copyright 2015 American Chemical Society.....	12
Figure 2.1: Schematic diagram of an ideal SAM of alkanethiolates on a flat gold surface....	23
Figure 2.2: Diagram of the chemical structure of DIBO.	26
Figure 2.3: Schematic illustration of the microcontact printing technique.....	28
Figure 2.4: (a) Illustration of a propagating SPP at the interface between a planar metal surface and a dielectric material; (b) Representation of the strength of the strength of the electric field $ E_z $ decaying exponentially in the z direction, away from the metal surface ...	29
Figure 2.5: Diagram of localized surface plasmon resonance of a metallic nanoparticle induced by incident light.....	31
Figure 2.6: Photoexcitation and subsequent relaxation processes of an LSPR on a metallic nanoparticle.....	33
Figure 2.7: Direct and indirect CT-driven PMCRs.....	35

Figure 2.8: Energy diagram depicting the Rayleigh, Stokes, and anti-Stokes scattering processes.	38
Figure 2.9: Illustration of the phase change of (a) s-polarized light and (b) p-polarized light upon reflection from a metallic surface.	43
Figure 3.1: Schematic diagram of the PM-IRRAS optical setup and electronic processing. .	64
Figure 3.2: (a) Assembly of cyclopropenone SAMs. Water contact angles were measured in triplicate and reported as an average. (b) Overlaid PM-IRRAS spectrum of cyclopropenone SAM and FTIR spectrum of model compound 6; blue spectrum designates FTIR spectrum of model molecule; red spectrum designates PM-IRRAS spectrum of SAM. Arrow indicates respective scale.	72
Figure 3.3: Modification of SAMs via photo-enabled click chemistry with azides A-C. Water contact angles were measured in triplicate and reported as an average. Blue spectra designate FTIR spectra of model molecules; red spectra designate PM-IRRAS spectra of SAMs. Arrow indicates respective scale.	74
Figure 3.4: Photopatterning of SAMs on gold using biotin-N ₃ and streptavidin Alexa Fluor 488.....	76
Figure 3.5: Cell adhesion studies using cyclopropenone SAMs; (a) fluorescence microscopy image of the substrate irradiated and derivatized with cyclic RGDFK peptide at a lower magnification and (b) at a higher magnification; (c) fluorescence microscopy image of the substrate not irradiated in the presence of cyclic RGDFK peptide at a lower magnification and (d) at a higher magnification.	77
Figure 4.1: Top view schematic of the Innostamp 40 TM working areas and experimental apparatus.	89
Figure 4.2: Schematic diagram representing the setup and procedure for plasmon-mediated grafting of diazonium salts under laser irradiation.....	92
Figure 4.3: Schematic diagram of the setup for the measurement of SERS spectra.	93

Figure 4.4:(a) SEM image of raspberry-like AuNPs; (b) SEM image at a higher magnification, to show more accurately the size and morphology of the AuNPs..... 94

Figure 4.5: (a) SEM image of the AuNP-patterned substrate; (b) SEM image of the AuNP-patterned substrate at a higher magnification to show AuNP distribution and line periodicity; (c) Absorbance spectrum of the AuNP-patterned substrate..... 95

Figure 4.6: (a) SERS mapping composed of 20×10 spectra on the AuNP-patterned substrate, showing variation of the SERS peak intensity at 1332 cm^{-1} for 4-NTP SAMs; (b) SEM image of a similar region as the mapped area; (c) SERS spectra from the positions I and II indicated in (a); (d) Raman spectrum of 4-NTP powder on a glass coverslip..... 97

Figure 5.1: (a) SEM image of a substrate with raspberry-like AuNPs printed into a grid pattern; SEM images of a substrate with raspberry-like AuNPs printed into a pattern of concentric rings (b) at a low magnification, to show the curvature of the rings, and (c) at a higher magnification. 113

List of Schemes

Scheme 1.1: (a) “Click-to-release” pathway on gold nanoparticles via strain-promoted alkyne-azide and alkyne-nitrone cycloaddition (SPAAC and SPANC, respectively) reactions, and Staudinger-Bertozzi ligation. ⁶⁵ (b) “Double-click” pathway on gold nanoparticles with biotin and a Rhodamine B derivative. ⁶⁵ Adapted with permission from ref. [65]. Copyright 2019 American Chemical Society.	7
Scheme 2.1: General reaction scheme for the CuAAC reaction.....	24
Scheme 2.2: General reaction scheme for the SPAAC reaction.	26
Scheme 3.1: General strategy for incorporation of strained alkynes onto flat gold substrates and subsequent SPAAC reaction.	61
Scheme 3.2: Synthesis of thiol 4 and model molecules.....	69
Scheme 4.1: : General reaction mechanism for the plasmon-mediated reduction of 4-NBD by hot electron donation and subsequent grafting of the aryl radical species onto an AuNP.....	99

List of Appendices

Appendix A – Details for PM-IRRAS Spectral Calibration.....	116
Appendix B – Copyrights	120

List of Abbreviations

μCP	microcontact printing
λ	wavelength
ω_I	frequency of incident light
ω_R	frequency of Raman-scattered light
4-NDB	4-nitrobenzenediazonium
4-NTP	4-nitrothiophenol
AuNP	gold nanoparticle
BCP	block copolymer
CT	charge transfer
CuAAC	copper (I)-catalyzed Huisgen alkyne-azide cycloaddition
DIBO	4-dibenzocyclooctyne
DMAB	<i>p,p</i> -dimercaptoazobenzene
DMF	dimethylformamide
E_0	incident electric field strength
E_f	Fermi level
E_{loc}	local near-field strength
E_z	electric field strength
EM	electromagnetic
FTIR	fourier transform infrared
HER2	human epidermal receptor protein 2
$h\nu$	light
IR	infrared
IRRAS	infrared reflection-absorption spectroscopy
LSPR	localized surface plasmon resonance
LUMO	lowest unoccupied molecular orbital
M	enhancement factor
n	refractive index
NMR	nuclear magnetic resonance
NP	nanoparticle
<i>p</i> -ATP	<i>p</i> -aminothiophenol

PDMS	polydimethylsiloxane
PEG	polyethylene glycol
PEM	photoelastic modulator
PMCR	plasmon-mediated chemical reaction
PM-IRRAS	polarization modulation infrared reflection-absorption spectroscopy
PS- <i>b</i> -P4VP	polystyrene- <i>block</i> -poly(4-vinylpyridine)
QD	quantum dot
r.t.	room temperature
SAM	self-assembled monolayer
SEM	scanning electron microscope
SERS	surface-enhanced Raman spectroscopy
SPAAC	strain-promoted alkyne-azide cycloaddition
SPP	surface plasmon polariton
SPR	surface plasmon resonance
TFA	trifluoroacetic acid
THF	tetrahydrofuran
UV-vis	ultraviolet-visible
vis-NIR	visible – near-infrared

Chapter 1

1 General Introduction

Surfaces constitute the boundary between a bulk material and its surroundings and thus govern the interactions of a material with its environment. The molecular-level chemical properties of surfaces play a fundamental role in defining the functions and characteristics of material interfaces. Surface chemistry may be altered through chemical reactions to achieve or optimize specific functional properties. Deliberate chemical modifications to surfaces enable control over the physical, chemical, or biochemical properties of surfaces without affecting the bulk material. Refined control over surface properties and interactions is highly desirable as chemical modifications may be used in the construction of novel interfaces and devices for a vast range of applications. Indeed, the exploitation of engineered surfaces has led to great advances in many fields across science and technology. Consequently, there is constant high demand both in academic research and in industry for new and improved surface modification techniques that allow for precise tailoring of surface reactivity, function, and architecture necessary for the development of advanced materials.

1.1 Material Surface Modifications: Importance and Applications

In addition to conferring specific functions and properties on a surface, ideal surface modification techniques are high yielding, robust, cost effective, simple to execute, and utilize straightforward covalent chemistry. Many surface functionalization and modification techniques have been developed to accommodate several different types of substrates and to alter many different properties including but not limited to wettability,¹⁻² adhesion,³⁻⁴ corrosion resistance,⁵⁻⁶ optical properties,⁷⁻⁸ biocompatibility,⁹⁻¹⁰ and specific recognition of biological or biochemical components.¹¹⁻¹² Surface modifications may also be used to produce highly reactive platforms designed to facilitate further modifications. Their broad versatility and ability to enable a high degree of control over surface chemistry often place surface modifications in the vanguard of new developments in functional materials.

There are countless cases in the literature of surface modifications designed to control the interaction between a surface and its environment. In particular, tunable wettability or hydrophilicity is of great interest for engineering anti-corrosive, anti-icing, anti-fogging, and self-cleaning surfaces for many applications.¹³⁻¹⁴ For example, Shin *et al.* have recently demonstrated that the wettability of solution-shearing blades used in the fabrication of halide perovskite solar cells strongly influences the properties of the perovskite thin film, directly impacting the power conversion efficiency of the cells.¹⁵ Vapour-treating the shearing blade with trichloro-(1H,1H,2H,2H-perfluorooctyl)-silane to produce a non-wetting blade was found to increase perovskite film thickness and coverage, significantly improving solar cell efficiency.¹⁵ In another study, Takahara and coworkers utilized focused ion beam irradiation to reduce the fluorine content at the surfaces of self-assembled monolayers to increase their hydrophilicity.¹⁶ They then used the same approach to create submicron-scale hydrophobic-hydrophilic hybrid surfaces, which are expected to enable the fabrication of micro- and nano-structured fluidic devices with applications in nanobiotechnology and high-resolution printing.¹⁶ Microscale water evaporation experiments were performed on the patterned hydrophobic-hydrophilic hybrid surface, revealing that when a water droplet covering the entire patterned area slowly evaporates from the surface, it results in the formation of tiny water droplets left behind on the surface specifically in the patterned rectangular hydrophilic regions. This experiment, illustrated in Figure 1.1, confirms that the hydrophilic dots created using focused ion beam irradiation of monolayers can control the position of water droplets formed following rupture of the liquid film.¹⁶

Surface chemical modification techniques are essential tools in nanotechnology and molecular electronics. The foundation of the field of molecular electronics, motivated by the goal to shrink traditional electrical circuits down to the nanometer scale, is the use of individual organic molecules or ensembles of molecules as working building blocks for the fabrication of electronic devices and components.¹⁷⁻¹⁸ One of the most important concepts in molecular electronics is the molecular junction, wherein one or more molecules are in electrical contact with two conductors (or semi-conductors) in a conductor-molecule-conductor configuration, such that electrons are transmitted through the molecules.¹⁷⁻²⁰ As efficient electron transport across a junction is integral to its

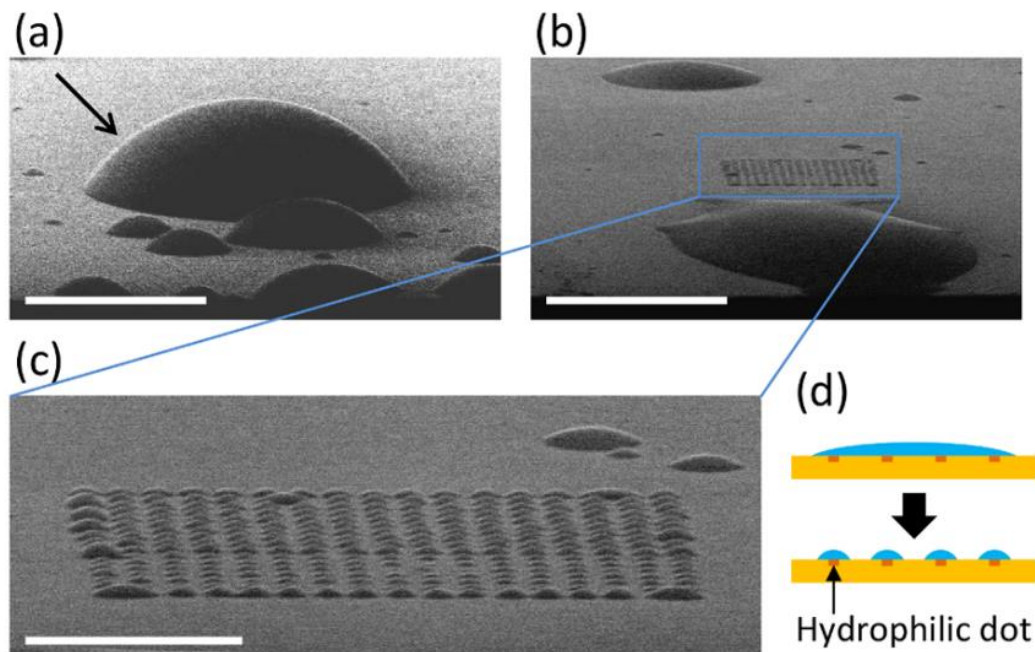


Figure 1.1: Environmental scanning electron microscopy images of a water droplet on the patterned hydrophobic-hydrophilic hybrid surface (a) before and (b) after evaporation.¹⁶ (c) High-magnification image of (b).¹⁶ (d) Diagram of small droplet formation during water evaporation.¹⁶ The scale bar in (a), (b), and (c) are 10, 10, and 3 μm , respectively.¹⁶ Adapted with permission from ref. [16]. Copyright 2015 American Chemical Society.

function, very precise control over the composition, structure, and electronic properties of the organic molecular component is crucial. This fine control is often accomplished using surface modification techniques to alter one or both of the electrodes. Many ensemble molecular junctions are fabricated by forming self-assembled monolayers on one electrode with terminal functional groups that react covalently with the second electrode to form a bridge.²¹⁻²² Langmuir-Blodgett films are also commonly employed as the organic component of molecular junctions.^{20,23} In other cases, electrochemical reactions have been used to covalently graft organic layers onto the electrodes.^{22,24-25} Several functional microelectronic devices have been constructed using ensemble molecular junctions with tailored organic monolayers, including molecular diodes,²⁶⁻²⁷ switches,²⁸⁻²⁹ transistors,³⁰⁻³¹ and molecular memories.³²⁻³³

Controllable chemical modifications of surfaces are also vitally important in biochemistry and medicine. Notably, biosensors and biosensing technologies have seen tremendous improvements in recent years due in part to advances in surface modification techniques. These are devices that combine biological receptors with a physicochemical detector to detect with high sensitivity the presence of specific biological analytes and to monitor their function. Surface modifications are a key step in the fabrication of biosensing devices, as they are used to prepare surfaces for specific recognition of biological or biochemical species by chemical attachment of biological receptor components to surfaces.³⁴⁻³⁶ For example, Girotto and coworkers developed a highly sensitive and specific surface plasmon resonance-based biosensor for the detection of human epidermal receptor protein-2 (HER2) antigen – a protein strongly associated with breast cancer – by functionalizing a plasmonically active metallic surface with HER2 antibodies.³⁷ The sensor was coupled to a microfluidic system and ultraviolet-visible (UV-vis) spectrometer for solution flow and optical measurements, respectively.³⁷ The sensor shows potential to be used for the diagnosis or prognosis of breast cancer. Another group reported the successful development of a nano-biosensor for the detection of α -1 antitrypsin, a biomarker for Alzheimer's disease, through multiple chemical modifications to different surfaces.³⁸ The authors proposed a novel sandwich-type electrochemical biosensor using alkaline phosphatase-labeled α -1 antitrypsin antibody-functionalized silver nanoparticles as signal enhancers and perylene tetracarboxylic acid-treated carbon nanotubes as the sensing platform capable of binding NH_2 -modified α -1 antitrypsin aptamers for immobilizing α -1 antitrypsin.³⁸ The biosensor demonstrated exceptional specificity, stability, reproducibility, and high sensitivity for α -1 antitrypsin, and holds potential for future point-of-care diagnostics of Alzheimer's disease.³⁸ Such methodologies may be applied more broadly to other medical diagnostic biosensing, to surface-based protein-ligand interaction studies, and even to the development of bioelectronics. Further, chemical modifications of solid surfaces with proteins and other biological species play a very important role in mitigating negative biological reactions to medical implants and devices by the body, as the biological response to such objects is governed largely by their surface chemistry.³⁹ Surface modifications allow for the retention of key physical properties and functionalities of the implanted device while

enabling control over the composition and state of surface proteins that actively improve the biological reaction to the tissue-device interface, including coagulation and immune response.³⁹⁻⁴¹ Similar functionalization techniques to increase biocompatibility may also be used to prepare metallic nanoparticles for targeted drug delivery.⁴¹⁻⁴⁴

1.2 Methods of Interest for Chemically Modifying Metal Surfaces

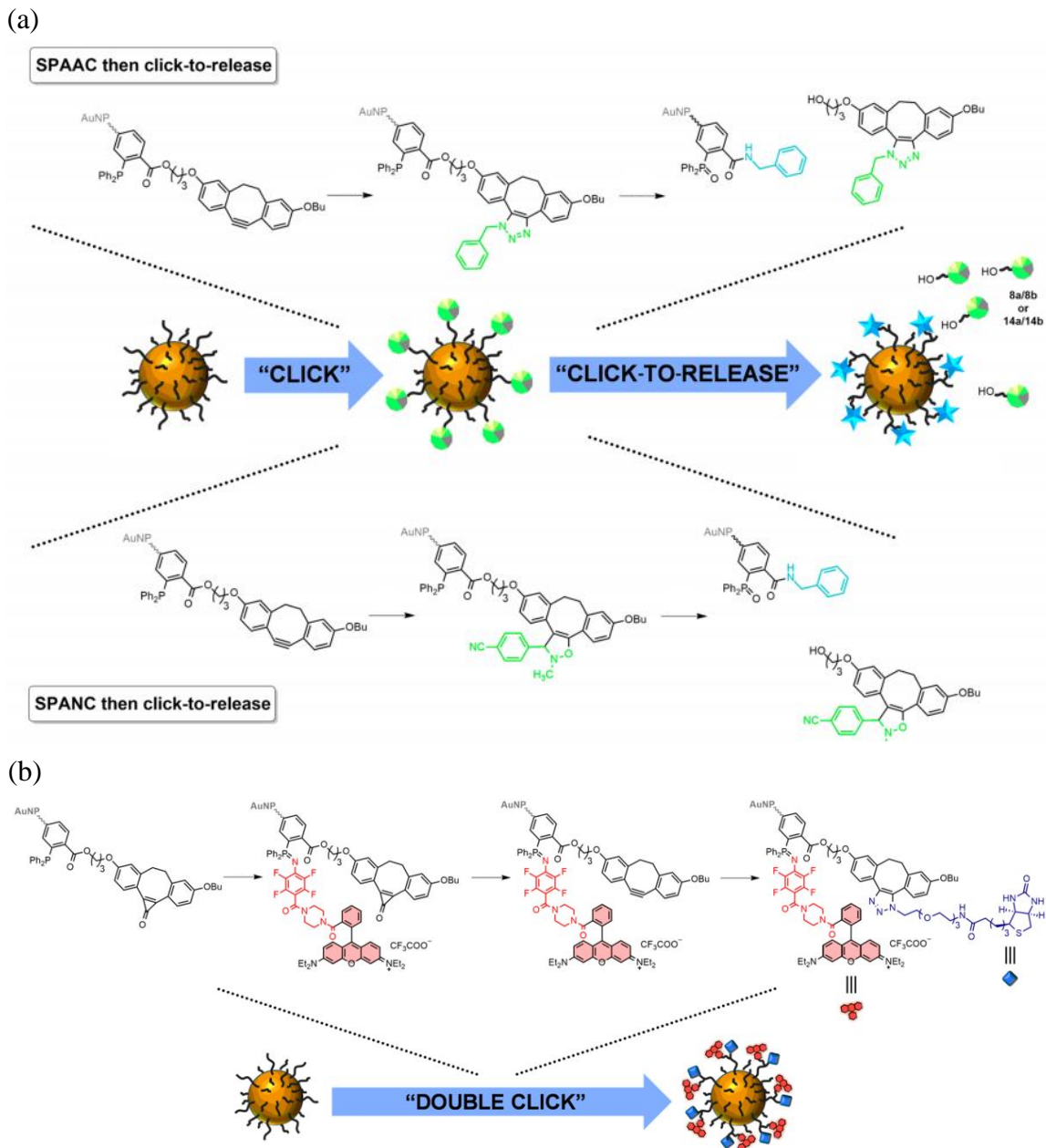
Due to their unique chemical, mechanical, optical, and electronic properties, many metals are materials of great interest for surface modification. Chemical modifications to metallic surfaces are crucial to numerous fields including electronics,⁴⁵ nanotechnology,⁴⁶ lab-on-a-chip technology,⁴⁷ molecular sensing and biosensing,⁴⁸⁻⁴⁹ design and construction of medical implants,⁵⁰⁻⁵² targeted drug delivery,⁵³⁻⁵⁴ and corrosion protection.⁵⁵ One of the most common approaches to control the surface chemistry of metals is through the attachment of organic compounds to the metal surface. A monolayer or thin film of organic molecules bound to a metal may be used to completely alter the surface chemistry of the metal, depending on the identity and chemical properties of the molecule. In this thesis, select strategies for chemically modifying metallic surfaces using organic species are investigated in detail. Namely, click chemistry and plasmon-mediated chemistry are each explored as a means to change the surface chemistry of metals.

1.2.1 Click Chemistry

Click chemistry refers to a group of reactions that are modular, rapid, high yielding, stereospecific, versatile, robust, insensitive to water and oxygen, wide in scope, simple to perform, based on readily available starting materials, run in mild or easily removed solvents, and generate easily purified products.⁵⁶ Due to their broad applicability and their ability to link reactants together with high efficiency, many click reactions have been established as excellent tools for material surface modifications. Click reactions present the possibility to attach manifold chemical functionalities to surfaces, and thus have found widespread applications in the functionalization and modification of metal surfaces. Collman *et al.* in 2004 were the first to report the use of Huisgen 1,3-dipolar

cycloadditions to modify the surface chemistry of gold electrodes coated with self-assembled monolayers.⁵⁷ Gold electrodes were functionalized with self-assembled monolayers of azidoundecanethiol, and the terminal azide groups were reacted with either ethynyl ferrocene or propynone ferrocene in the presence of Cu(I) catalyst as a model reaction system for this proof-of-concept study to demonstrate the applicability of Huisgen 1,3-dipolar cycloaddition click reactions as a general methodology for modifying metal electrode surfaces.⁵⁷ In a more recent example of click chemistry performed on metal surfaces, Takahara and coworkers demonstrated the effective post-modification of various polymer-coated metal surfaces, including aluminum, nickel, titanium, and stainless steel, using photoinitiated thiol-ene click chemistry.⁵⁸

One of the most attractive properties of many click chemistry reactions is their biocompatibility. Bioorthogonal reactions – that is, any reaction that can occur within a living system without interfering with native biological or biochemical functions – have become increasingly important for a wealth of applications in biochemistry and biology, including *in vivo* imaging,⁵⁹ bioconjugation,⁶⁰ protein labelling,⁶¹ and even the *in vivo* assembly of functional therapeutics.⁶² The combination of bioorthogonal click chemistry with functional metallic nanomaterials has been the subject of rising interest for its potential applications in targeted drug delivery systems.⁶³⁻⁶⁴ The Workentin group recently reported the development of multi-functional gold nanoparticles functionalized with a dual-orthogonal molecular tool that enables the interchangeable use of four distinct bioorthogonal transformations (the strain promoted alkyne-azide (SPAAC) and alkyne-nitrone (SPANIC) cycloaddition click reactions, the perfluoroaryl azide Staudinger reaction, and the Staudinger Bertozzi ligation) capable of following both “double-click” and “click-to-release” pathways to easily attach, release, and replace functionalities.⁶⁵ Each of these pathways are shown in Scheme 1.1. They further presented a proof-of-concept model for gold nanoparticle-based pretargeted delivery of a fluorophore, specifically a Rhodamine B derivative, to human fibroblast cells with biotin as the targeting agent using their dual-orthogonal molecular tool via the “double click” strategy.⁶⁵ This system has potential applications in the development of nanocarriers for targeted drug delivery.



Scheme 1.1: (a) “Click-to-release” pathway on gold nanoparticles via strain-promoted alkyne-azide and alkyne-nitrone cycloaddition (SPAAC and SPANC, respectively) reactions, and Staudinger-Bertozzi ligation.⁶⁵ (b) “Double-click” pathway on gold nanoparticles with biotin and a Rhodamine B derivative.⁶⁵ Adapted with permission from ref. [65]. Copyright 2019 American Chemical Society.

In addition to targeted drug delivery, click chemistry reactions are also often employed on metallic nanostructured surfaces for biosensing applications.⁶⁶ Bioorthogonal click reactions offer better control over the bioconjugation process, significantly increased chemoselectivity, and shortened reaction times compared to more traditional bioconjugation techniques for the fabrication of biosensors.⁶⁶⁻⁶⁸ There are a multitude of examples in literature of biosensors incorporating click reactions either as a surface modification step in biosensor preparation, or as the mechanism of bioanalyte detection. In an example of the former, Chiari *et al.* utilized the Cu(I)-catalyzed alkyne-azide cycloaddition (CuAAC) click reaction to functionalize polymer-coated gold nanoparticles with anti-mouse IgG antibodies as a proof-of-concept study to show the general applicability of the click chemistry approach to preparing biosensors, as antibodies are often essential components in the development of labels in biosensing techniques.⁶⁹ In this approach, gold nanoparticles were coated with an alkyne-bearing polymer to stabilize and prevent aggregation of the nanoparticles, and to enable alkyne-azide click chemistry at the nanoparticle surface.⁶⁹ Azide-modified anti-mouse IgG antibodies were “clicked” onto the nanoparticles in the presence of Cu(I) catalyst, and their ability to specifically recognize the complementary anti-CD63 antibody in a biosensing assay was successfully tested.⁶⁹ In another study, Li and coworkers presented a novel click chemistry-based colorimetric biosensor for microbial detection.⁷⁰ In this work, a mixture was prepared of gold nanoparticles functionalized with either azide- or alkyne-terminated long chain thiols, in solution with Cu²⁺ ions.⁷⁰ This method of biosensing exploited the microbial copper homeostasis mechanisms that allowed some bacteria to reduce Cu²⁺ to Cu⁺.⁷⁰ *Escherichia coli*, a model bacteria, was added to the gold nanoparticle solution and immediately reduced Cu²⁺ to Cu⁺, which enabled CuAAC click reactions to occur between the azide- and alkyne-coated nanoparticles, resulting in nanoparticle aggregation.⁷⁰ Nanoparticle aggregation caused an immediate visible colour change in solution, indicating the successful colorimetric detection of bacteria.⁷⁰

1.2.2 Plasmon-Mediated Chemistry

Plasmons are collective oscillations of free electrons in a conductive material. When visible light is incident upon a metallic nanostructure, excitation of the electron oscillations may result in confinement of the electric field to nanoscale domains on the nanostructure surface, leading to “hotspots” of highly intense near-field enhancement. This phenomenon is referred to as localized surface plasmon resonance. This intense electromagnetic near-field enhancement is often exploited for plasmon-enhanced spectroscopies. However, one of the most exciting new developments in plasmonics has been the discovery that surface plasmon resonances may also be used to catalyze a variety of chemical processes. Excited localized surface plasmons can initiate or catalyze chemical processes either through localized electric field enhancement, local heating effects, or the donation of high-energy electrons and holes, generated through plasmon decay, to chemical species. Chemical reactions may also be facilitated by several of these factors synergistically. To date, some of the most impactful reactions with societal interest for which plasmon-driven catalysis has been achieved are photoelectrochemical water splitting,⁷¹⁻⁷² which is employed as a means to create and store energy in the form of hydrogen fuel, and photocatalytic CO₂ reduction,⁷³ an important reaction for lowering atmospheric CO₂ levels to diminish pollution and combat climate change.

The field of plasmonics has become a subject of heightened interest in the surface chemistry community. Over the past few years, the integration of plasmonics into chemical surface modification techniques has become a rapidly growing research area with wide-ranging applications. It utilizes the localized field enhancements, local heating, and electron excitation associated with localized surface plasmon resonances to catalyze surface functionalization or modification reactions with a high degree of spatial control down to the nanoscale. Plasmon-mediated surface chemistry offers the potential for a fast and cost-effective means to site-selective surface modifications by catalyzing reactions at specific localized reactive areas on nanostructure surfaces. One of the most well-known and well-studied plasmon-mediated reactions is the dimerization of *p*-aminothiophenol (*p*-ATP) into *p,p*-dimercaptoazobenzene (DMAB). While it is often used as a model reaction to gain insight into plasmon-mediated reaction mechanisms,⁷⁴⁻⁷⁶ it has also been

employed to modify the surface chemistry of metallic nanoparticles. Hildebrandt *et al.* made use of the simple and rapid plasmon-induced coupling of *p*-ATP into DMAB to create reversible molecular photoswitches on Ag/AgCl nanoparticles.⁷⁷ Ag/AgCl substrates were functionalized with *p*-ATP and then laser irradiated to activate the formation of DMAB. Continued irradiation induced the photoisomerization of the adsorbed DMAB from its *cis* configuration to *trans*, and subsequent isolation of the substrate in the dark for several minutes resulted in the recovery of *cis*-DMAB.⁷⁷ Such photoswitchable platforms have many applications in micro- and nanopatterning of material surfaces.⁷⁸ Another group also employed the plasmon-induced *p*-ATP/DMAB transformation for patterning on the nanoscale; Fang and coworkers proposed a novel method for nanoscale molecular patterning of a planar gold surface functionalized with a self-assembled monolayer of *p*-ATP.⁷⁹ The molecular patterning of these molecules involved placing a silver-coated scanning probe microscopy tip located a few nanometers above an ATP-functionalized flat gold substrate and irradiating the tip with a laser, yielding the localized transformation of *p*-ATP into DMAB on the substrate only in the area under the tip.⁷⁹ By moving the tip across the functionalized surface under laser irradiation, DMAB can potentially be site-specifically patterned into the surface with a precise control and high spatial resolution at the nanoscale.

Initiation of click reactions via irradiation with visible light, which is more readily available than other means of catalysis and is not harmful to biological samples, is an under-explored field. Localized surface plasmon resonances represent a convenient method of coupling visible light energy to the initiation of chemical reactions. Lyutakov and coworkers present a novel approach for plasmon-mediated alkyne-azide cycloaddition reaction activation, in the absence of the typically required Cu(I) catalyst, wherein diazonium salts with alkyne moieties are grafted onto a plasmonically active gold grating surface, then azide-bearing molecules are introduced to the surface and the click reaction is triggered by laser irradiation of the grating surface.⁸⁰ Reaction progress is monitored dynamically via surface-enhanced Raman spectroscopy (SERS) of the “clicked” molecules on the grating surface, and a reaction mechanism is proposed involving the injection of high energy electrons from the plasmonic surface into the organic species.⁸⁰ Plasmon-mediated click chemistry has also been demonstrated by

Lamy de la Chapelle *et al.*, who reported successful thiol-ene coupling reactions induced by nanoplasmonic effects on the surfaces of gold nanostructures under visible light irradiation.⁸¹

One of the greatest draws of plasmon-mediated chemistry is the potential for highly controllable nanolocalization of surface reactions, as this introduces the possibility of nanoscale patterning and multi-functionalization. For example, Lacroix *et al.* showed the plasmon-mediated reduction of aryl diazonium salts which resulted in the grafting of poly(aryl) films specifically at the vertices of triangular gold nanostructures, aligning precisely with the plasmonic “hotspots” of the nanostructures, as can be seen in Figure 1.2a.⁸² Furthermore, by utilizing different polarizations of light, different plasmon modes may be excited on a given metallic nanostructure allowing for the activation of different reactions at different areas around the nanostructure. Bachelot *et al.* utilized this property to develop two-colour plasmonic nanoemitters, depicted in Figure 1.2b, that enable the selection of the dominant emitting wavelength by rotating the polarization of incident light.⁸³ The nanoemitters were fabricated by immersing gold nanodisks in a solution of green-emitting quantum dot (QD)-grafted pentaerythritol triacrylate, irradiating with a linearly polarized laser to achieve plasmon-driven two-photon polymerization of the QD-grafted pentaerythritol triacrylate along one axis of the nanodisk, then immersing the gold nanodisks in a solution of red-emitting QD-grafted pentaerythritol triacrylate and irradiating with a linearly polarized laser orthogonal to the first to polymerize the QD-grafted pentaerythritol triacrylate along the opposite axis of the nanodisk.⁸³ The two different colours of the QDs could then be optically selected by the polarization of the incident light.⁸³ Further discussion of plasmon-mediated reactions, and specifically the plasmon-driven reduction of diazonium salts, will be realized in Chapter 4 of this thesis.

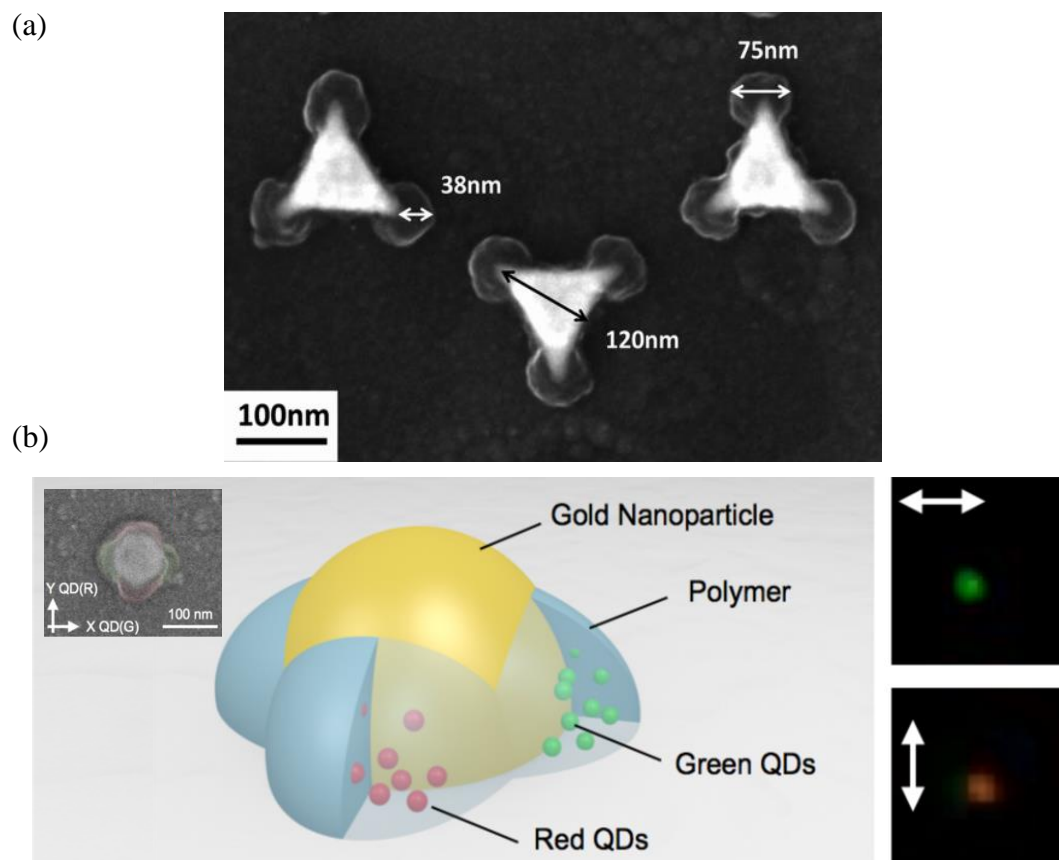


Figure 1.2: (a) Scanning electron microscopy image of triangular gold nanostructures grafted with diazonium salts via plasmonic effects.⁸² Adapted with permission from ref. [82]. Copyright 2017 American Chemical Society. (b) Schematic representation and scanning electron microscopy image of the gold nanodisk-based two-colour nanoemitter, alongside far-field fluorescence images of the nanoemitter under illumination with X-axis and Y-axis polarization.⁸³ Adapted with permission from ref. [83]. Copyright 2015 American Chemical Society.

1.3 Scope of Thesis

In this work, two projects were pursued relating to the functionalization, chemical modification, and spectroscopic characterization of metallic surfaces. This thesis is organized into five chapters, each summarized as follows:

Chapter 2 delves into the physical and theoretical principles underlying several key surface chemistry and spectroscopy techniques that feature in thesis. Self-assembled monolayers, microcontact printing, click chemistry, and plasmon-mediated chemistry are each discussed with respect to their applications in surface functionalization and modification. Essential theoretical background and fundamentals for plasmonics, Raman spectroscopy, SERS, and polarization modulation infrared reflection-absorption spectroscopy are provided.

Chapter 3 investigates the possibility of using SPAAC reactions as a tool to finely control the surface chemistry of flat gold substrates and to prepare flat gold substrates for biochemical applications. Thiolated, cyclopropenone-caged strained alkyne precursors are functionalized onto gold through self-assembly and then photochemically deprotected to reveal a reactive template for surface modifications via SPAAC reaction. Polarization modulation infrared reflection-absorption spectroscopy is used to detect and characterize monolayers of protected strained alkynes adsorbed onto gold substrates, and to probe the progress of the alkyne photo-deprotection and subsequent surface SPAAC reactions.

Chapter 4 focuses on the design and construction of new plasmonically active substrates using soft lithography techniques, and then employing these substrates to catalyze plasmon-driven surface reactions and to characterize these surface modifications via SERS. Specifically, nitrobenzenediazonium-derived aryl thin films are chemically grafted onto spatially patterned gold nanoparticles via the plasmon-mediated reduction of aryl diazonium salts, and then the reaction products are identified through both SERS and scanning electron microscopy.

Chapter 5 concludes this work with final remarks and a brief discussion of the potential future directions of this research and its wider applications.

1.4 References

1. Lee, H. J.; Park, K. *Materials* **2016**, *9*.
2. Sun, T.; Feng, L.; Gao, X.; Jiang, L. *Acc. Chem. Res.* **2005**, *38*, 644-652.
3. Miller, D. J.; Araujo, P. A.; Correia, P. B.; Ramsey, M. M.; Kruithof, J. C.; van Loosdrecht, M. C.; Freeman, B. D.; Paul, D. R.; Whiteley, M.; Vrouwenvelder, J. S. *Water Res.* **2012**, *46*, 3737-3753.
4. Noeske, M.; Degenhardt, J.; Strudthoff, S.; Lommatzsch, U. *Int. J. Adhes. Adhes.* **2004**, *24*, 171-177.
5. Chou, T. P.; Chandrasekaran, C.; Limmer, S. J.; Seraji, S.; Wu, Y.; Forbess, M. J.; Nguyen, C.; Cao, G. Z. *J. Non-Cryst. Solids* **2001**, *290*, 153-162.
6. Ishizaki, T.; Hieda, J.; Saito, N.; Saito, N.; Takai, O. *Electrochim. Acta* **2010**, *55*, 7094-7101.
7. John, R. E.; Chandran, A.; Thomas, M.; Jose, J.; George, K. C. *Appl. Surf. Sci.* **2016**, *367*, 43-51.
8. Park, Y.-S.; Choi, S.-E.; Kim, H.; Lee, J. S. *ACS Appl. Mater. Interfaces* **2016**, *8*, 11788-11795.
9. Meyers, S. R.; Grinstaff, M. W. *Chem. Rev.* **2012**, *112*, 1615-1632.
10. Raval, N.; Kalyane, D.; Maheshwari, R.; Tekade, R. K. Chapter 17 - Surface Modifications of Biomaterials and Their Implication on Biocompatibility. In *Biomaterials and Bionanotechnology*, Tekade, R. K. Ed. Academic Press: 2019; pp 639-674.
11. Brolo, A. G. *Nat. Photon.* **2012**, *6*, 709-713.

12. Voon, C. H.; Sam, S. T. 2 - Physical Surface Modification on the Biosensing Surface. In *Nanobiosensors for Biomolecular Targeting*, Gopinath, S. C. B.; Lakshmi Priya, T. Eds. Elsevier: 2019; pp 23-50.
13. Eijkel, J. *Lab Chip* **2007**, *7*, 299-301.
14. Gao, L.; McCarthy, T. J.; Zhang, X. *Langmuir* **2009**, *25*, 14100-14104.
15. Lee, H. S.; Kim, M. K.; Pae, S. R.; Kim, D.; Seo, H.; Boonmongkolras, P.; Gereige, I.; Park, S.; Shin, B. *Nano Energy* **2020**, *74*, 104830.
16. Yamada, Y.; Takahashi, K.; Ikuta, T.; Nishiyama, T.; Takata, Y.; Ma, W.; Takahara, A. *J. Phys. Chem. C* **2016**, *120*, 274-280.
17. Huang, X.; Li, T. *J. Mater. Chem. C* **2020**, *8*, 821-848.
18. Mathew, P. T.; Fang, F. *Engineering* **2018**, *4*, 760-771.
19. Komoto, Y.; Fujii, S.; Iwane, M.; Kiguchi, M. *J. Mater. Chem C* **2016**, *4*, 8842-8858.
20. McCreery, R. L. *Chem. Mater.* **2004**, *16*, 4477-4496.
21. Chabynyc, M. L.; Chen, X.; Holmlin, R. E.; Jacobs, H.; Skulason, H.; Frisbie, C. D.; Mujica, V.; Ratner, M. A.; Rampi, M. A.; Whitesides, G. M. *J. Am. Chem. Soc.* **2002**, *124*, 11730-11736.
22. Martin, P.; Della Rocca, M. L.; Anthore, A.; Lafarge, P.; Lacroix, J.-C. *J. Am. Chem. Soc.* **2012**, *134*, 154-157.
23. Stewart, D. R.; Ohlberg, D. A. A.; Beck, P. A.; Chen, Y.; Williams, R. S.; Jeppesen, J. O.; Nielsen, K. A.; Stoddart, J. F. *Nano Lett.* **2004**, *4*, 133-136.
24. Ru, J.; Szeto, B.; Bonifas, A.; McCreery, R. L. *ACS Appl. Mater. Interfaces* **2010**, *2*, 3693-3701.

25. Santos, L. M.; Ghilane, J.; Fave, C.; Lacaze, P.-C.; Randriamahazaka, H.; Abrantes, L. M.; Lacroix, J.-C. *J. Am. Chem. Soc.* **2008**, *112*, 16103-16109.
26. Yuan, L.; Nerngchamng, N.; Cao, L.; Hamoudi, H.; del Barco, E.; Roemer, M.; Sriramula, R. K.; Thompson, D.; Nijhuis, C. A. *Nat. Commun.* **2015**, *6*, 6324.
27. Seminario, J. M.; Zacarias, A. G.; Tour, J. M. *J. Am. Chem. Soc.* **2000**, *122*, 3015-3020.
28. Kudernac, T.; Katsonis, N.; Browne, W. R.; Feringa, B. L. *J. Mater. Chem.* **2009**, *19*, 7168-7177.
29. Irie, M. *Chem. Rev.* **2000**, *100*, 1685-1716.
30. Kubatkin, S.; Danilov, A.; Hjort, M.; Cornil, J.; Brédas, J.-L.; Stuhr-Hansen, N.; Hedegård, P.; Bjørnholm, T. *Nature* **2003**, *425*, 698-701.
31. Meng, L.; Xin, N.; Hu, C.; Wang, J.; Gui, B.; Shi, J.; Wang, C.; Shen, C.; Zhang, G.; Guo, H.; Meng, S.; Guo, X. *Nat. Commun.* **2019**, *10*, 1450.
32. Min, M.; Seo, S.; Lee, S. M.; Lee, H. *Adv. Mater.* **2013**, *25*, 7045-7050.
33. Kumar, S.; Merelli, M.; Danowski, W.; Rudolf, P.; Feringa, B. L.; Chiechi, R. C. *Adv. Mater.* **2019**, *31*, 1807831.
34. Bañuls, M.-J.; Puchades, R.; Maquieira, Á. *Anal. Chim. Acta* **2013**, *777*, 1-16.
35. Hou, S.; Zhang, A.; Su, M. *Nanomaterials* **2016**, *6*, 58.
36. Yüce, M.; Kurt, H. *RSC Adv.* **2017**, *7*, 49386-49403.
37. Monteiro, J. P.; de Oliveira, J. H.; Radovanovic, E.; Brolo, A. G.; Girotto, E. M. *Plasmonics* **2016**, *11*, 45-51.
38. Zhu, G.; Lee, H. J. *Biosens. Bioelectron.* **2017**, *89*, 959-963.

39. Ratner, B. D.; Allan S. Hoffman, B. D. R. F. J. S. J. E. L.; Knovel; Biomaterials, S. f.; Hoffman, A. S.; Schoen, F. J.; Lemons, J. E. *Biomaterials Science: An Introduction to Materials in Medicine*. Elsevier Science: 2004.
40. Thevenot, P.; Hu, W.; Tang, L. *Curr. Top. Med. Chem.* **2008**, *8*, 270-280.
41. Narayana, P. S. V. V. S.; Srihara, P, S. V. V. *Regen. Eng. Transl. Med.* **2019**,
42. Liu, J.; Wei, T.; Zhao, J.; Huang, Y.; Deng, H.; Kumar, A.; Wang, C.; Liang, Z.; Ma, X.; Liang, X.-J. *Biomaterials* **2016**, *91*, 44-56.
43. Daraee, H.; Eatemadi, A.; Abbasi, E.; Fekri Aval, S.; Kouhi, M.; Akbarzadeh, A. *Artif. Cell. Nanomed. B.* **2016**, *44*, 410-422.
44. Lim, W. Q.; Gao, Z. *Nano Today* **2016**, *11*, 168-188.
45. Gopinath, S. C. B.; LakshmiPriya, T.; Md Arshad, M. K.; Uda, M. N. A.; Al-Douri, Y. 9 - Nanoelectronics in Biosensing Applications. In *Nanobiosensors for Biomolecular Targeting*, Gopinath, S. C. B.; LakshmiPriya, T. Eds. Elsevier: 2019; pp 211-224.
46. Nagarajan, R. Nanoparticles: Building Blocks for Nanotechnology. In *Nanoparticles: Synthesis, Stabilization, Passivation, and Functionalization*, American Chemical Society: 2008; Vol. 996, pp 2-14.
47. Sengupta, P.; Khanra, K.; Chowdhury, A. R.; Datta, P. 4 - Lab-on-a-chip sensing devices for biomedical applications. In *Bioelectronics and Medical Devices*, Pal, K.; Kraatz, H.-B.; Khasnobish, A.; Bag, S.; Banerjee, I.; Kuruganti, U. Eds. Woodhead Publishing: 2019; pp 47-95.
48. Kulkarni, S.; Pandey, A.; Mutalik, S. *Nanomed.-Nanotechnol.* **2020**, *26*, 102175.
49. Suyan, Q.; Fusheng, Z.; Jingting, L.; Wei-Chuan, S. In *Portable SERS sensor for malachite green and other small dye molecules*, Proceedings of Optical Diagnostics and Sensing XVII: Toward Point-of-Care Diagnostics, San Francisco, California, USA, 30-31

January 2017, Cote, G.L.; SPIE International Society for Optics and Photonics, 2017; 1007202.

50. Bai, L.; Gong, C.; Chen, X.; Sun, Y.; Zhang, J.; Cai, L.; Zhu, S.; Xie, S. Q. *Metals* **2019**, *9*.

51. Sinha, S. K. Surface Modifications in Ti-Based Orthopaedic Implants. In *Biomedical Engineering and its Applications in Healthcare*, Paul, S. Ed. Springer Singapore: Singapore, 2019; pp 275-293.

52. Valiev, R. Z.; Parfenov, E. V.; Parfenova, L. V. *Mater. Trans.* **2019**, *60*, 1356-1366.

53. Palanisamy, S.; Wang, Y.-M. *Dalton Trans.* **2019**, *48*, 9490-9515.

54. Mugaka, B. P.; Hu, Y.; Ma, Y.; Ding, Y. Surface Modification of Gold Nanoparticles for Targeted Drug Delivery. In *Surface Modification of Nanoparticles for Targeted Drug Delivery*, Pathak, Y. V. Ed. Springer International Publishing: Cham, 2019; pp 391-403.

55. Chen, G.; Xue, L.; Wang, J.; Tang, Z.; Li, X.; Dong, H. *Corros. Sci.* **2020**, *174*, 108836.

56. Kolb, H. C.; Finn, M. G.; Sharpless, K. B. *Angew. Chem. Int. Ed.* **2001**, *40*, 2004-2021.

57. Collman, J. P.; Devaraj, N. K.; Chidsey, C. E. D. *Langmuir* **2004**, *20*, 1051-1053.

58. Zhang, Y.; Chu, C.-W.; Ma, W.; Takahara, A. *ACS Omega* **2020**, *5*, 7488-7496.

59. Agarwal, P.; Beahm, B. J.; Shieh, P.; Bertozzi, C. R. *Angew. Chem. Int. Ed.* **2015**, *54*, 11504-11510.

60. McKay, Craig S.; Finn, M. G. *Chem. Biol.* **2014**, *21*, 1075-1101.

61. Gong, Y.; Pan, L. *Tetrahedron Lett.* **2015**, *56*, 2123-2132.

62. Devaraj, N. K. *ACS Cent. Sci.* **2018**, *4*, 952-959.
63. Luo, W.; Gobbo, P.; Gunawardene, P. N.; Workentin, M. S. *Langmuir* **2017**, *33*, 1908-1913.
64. Yi, G.; Son, J.; Yoo, J.; Park, C.; Koo, H. *Biomater. Res.* **2018**, *22*, 13-13.
65. Luo, W.; Luo, J.; Popik, V. V.; Workentin, M. S. *Bioconjugate Chem.* **2019**, *30*, 1140-1149.
66. Chen, Y.; Xianyu, Y.; Wu, J.; Yin, B.; Jiang, X. *Theranostics* **2016**, *6*, 969-985.
67. Walper, S. A.; Turner, K. B.; Medintz, I. L. *Curr. Opin. Biotechnol.* **2015**, *34*, 232-241.
68. Neef, A. B.; Pernot, L.; Schreier, V. N.; Scapozza, L.; Luedtke, N. W. *Angew. Chem. Int. Ed. Engl.* **2015**, *54*, 7911-7914.
69. Finetti, C.; Sola, L.; Pezzullo, M.; Prospero, D.; Colombo, M.; Riva, B.; Avvakumova, S.; Morasso, C.; Picciolini, S.; Chiari, M. *Langmuir* **2016**, *32*, 7435-7441.
70. Mou, X.-Z.; Chen, X.-Y.; Wang, J.; Zhang, Z.; Yang, Y.; Shou, Z.-X.; Tu, Y.-X.; Du, X.; Wu, C.; Zhao, Y.; Qiu, L.; Jiang, P.; Chen, C.; Huang, D.-S.; Li, Y.-Q. *ACS Appl. Mater. Interfaces* **2019**, *11*, 23093-23101.
71. Liu, Z.; Hou, W.; Pavaskar, P.; Aykol, M.; Cronin, S. B. *Nano Lett.* **2011**, *11*, 1111-1116.
72. Naya, S.-i.; Kume, T.; Akashi, R.; Fujishima, M.; Tada, H. *J. Am. Chem. Soc.* **2018**, *140*, 1251-1254.
73. Kumari, G.; Zhang, X.; Devasia, D.; Heo, J.; Jain, P. K. *ACS Nano* **2018**, *12*, 8330-8340.

74. Zhan, C.; Wang, Z.-Y.; Zhang, X.-G.; Chen, X.-J.; Huang, Y.-F.; Hu, S.; Li, J.-F.; Wu, D.-Y.; Moskovits, M.; Tian, Z.-Q. *J. Am. Chem. Soc.* **2019**, *141*, 8053-8057.
75. Sarhan, R. M.; Koopman, W.; Schuetz, R.; Schmid, T.; Liebig, F.; Koetz, J.; Bargheer, M. *Sci. Rep.* **2019**, *9*, 3060.
76. Zhan, C.; Chen, X.-J.; Huang, Y.-F.; Wu, D.-Y.; Tian, Z.-Q. *Acc. Chem. Res.* **2019**, *52*, 2784-2792.
77. Song, W.; Querebillo, C. J.; Götz, R.; Katz, S.; Kuhlmann, U.; Gernert, U.; Weidinger, I. M.; Hildebrandt, P. *Nanoscale* **2017**, *9*, 8380-8387.
78. Fahrenbach, A. C.; Warren, S. C.; Incorvati, J. T.; Avestro, A.-J.; Barnes, J. C.; Stoddart, J. F.; Grzybowski, B. A. *Adv. Mater.* **2013**, *25*, 331-348.
79. Zeng, Z.; Qi, X.; Li, X.; Zhang, L.; Wang, P.; Fang, Y. *Appl. Surf. Sci.* **2019**, *480*, 497-504.
80. Guselnikova, O.; Postnikov, P.; Chehimi, M. M.; Kalachyovaa, Y.; Svorcik, V.; Lyutakov, O. *Langmuir* **2019**, *35*, 2023-2032.
81. Tijunelyte, I.; Guenin, E.; Lidgi-Guigui, N.; Colas, F.; Ibrahim, J.; Toury, T.; Lamy de la Chapelle, M. *Nanoscale* **2016**, *8*, 7105-7112.
82. Nguyen, V.-Q.; Ai, Y.; Martin, P.; Lacroix, J.-C. *ACS Omega* **2017**, *2*, 1947-1955.
83. Zhou, X.; Wenger, J.; Viscomi, F. N.; Le Cunff, L.; Béal, J.; Kochtcheev, S.; Yang, X.; Wiederrecht, G. P.; Colas des Francs, G.; Bisht, A. S.; Jradi, S.; Caputo, R.; Demir, H. V.; Schaller, R. D.; Plain, J.; Vial, A.; Sun, X. W.; Bachelot, R. *Nano Lett.* **2015**, *15*, 7458-7466.

Chapter 2

2 Principles of Material Surface Modification and Characterization Techniques

This chapter focuses on developing a thorough understanding of relevant surface functionalization strategies and key spectroscopic characterization techniques to serve as a basis for the research presented in this thesis. Various methods for surface modification, including self-assembled monolayer formation, click chemistry, and plasmon-mediated reactions, are discussed, and details regarding the optical and spectroscopic principles of polarization modulation infrared reflection-absorption spectroscopy and surface-enhanced Raman spectroscopy are provided.

2.1 Self-Assembled Monolayers

Self-assembled monolayers (SAMs) are well-defined and organized single-layer assemblies of organic molecules formed by spontaneous adsorption of organic species from solution or the gas phase onto solid surfaces.¹ This adsorption occurs spontaneously due to a chemical affinity between the adsorbates and the substrate, and because the close-packed monolayer lowers the free energy of the interface between the solid surface and the ambient environment.² The initial self-assembly is followed by spontaneous reorganization into densely packed, uniform, long-range, two-dimensional crystalline structures.³⁻⁴ This is commonly achieved by immersing the substrate in a dilute (1-10 mM) solution of the molecule of choice, washing the substrate with the same solvent, and then drying. Organic species that are suitable for SAM formation typically comprise a headgroup, which binds the molecule to the surface, a backbone, generally composed of alkyl chains, polyethylene glycol (PEG) chains, or aromatic oligomers, and a terminal group, which occupies the outer interface of the SAM and defines the topography and chemistry of the surface.³⁻⁵ The self-assembly process is strongly influenced by the affinity of the head group for the substrate, and by the lateral van der Waals interactions between backbone components, which are largely responsible for the molecular reordering and structural stabilization of the SAM following the initial chemisorption to

the surface.⁶ Careful selection of the head, backbone, and terminal groups can be used to specifically control the structural and chemical properties of the SAM.

Owing to their customizability and ease of use, SAMs provide a simple, flexible, and convenient system for creating highly ordered organic interfaces that allow specific tailoring and fine-tuning of surface properties. As a result, SAMs have been exploited extensively in research for an enormous range of practical applications in materials chemistry, biochemistry, and nanotechnology. Specifically, they have been employed as a means to control surface properties such as wettability,⁷ friction,⁸⁻⁹ adhesion,¹⁰ corrosion protection,¹¹ and lubrication;¹²⁻¹³ they have also been utilized in devices designed for molecular sensing,¹⁴ biosensing,¹⁵⁻¹⁶ and conjugation of biomolecules,¹⁷ and in nanofabrication techniques including microcontact printing¹⁸ and constructive lithography.¹⁹⁻²⁰

One of the most well-studied and commonly used SAM systems is the functionalization of gold surfaces with alkanethiols. Initially reported by Nuzzo and Allara in 1983,²¹ SAMs of thiolates on gold present a robust, versatile, and effective means of surface functionalization. Thiol SAMs form easily and rapidly, exhibit high stability and reproducibility, and allow a high degree of control over the macroscopic interfacial properties of surfaces through specific tailoring of their microscopic structure and composition.^{5,22} The foundation of all alkanethiol SAMs on gold is the strong and stable Au–thiol bond (40-50 kcal mol⁻¹) that anchors thiolated species to the gold surface.²³ This bond has been confirmed and studied by X-ray photoelectron spectroscopy, Fourier transform infrared spectroscopy, mass spectrometry, and Raman spectroscopy.⁴ The Au-S bond is generally considered to be covalent in nature, although the exact geometric and electronic configurations of the bond are still a topic of some debate.²³⁻²⁵ Alkanethiol SAMs typically arrange themselves with a surface density of approximately 4.5×10^{14} molecules per cm² and an average tilt angle between 20 – 30°,^{5,26} as shown in Figure 2.1; however, the overall arrangement of SAMs on a surface depends on a wide variety of factors, including the backbone and terminal group identities, substrate surface morphology, and the concentration and purity of the adsorbate during functionalization.

Surface properties may be controlled either by careful selection of the thiolated molecule itself, or via chemical modification of the SAM terminal groups post-assembly.²⁷⁻³¹

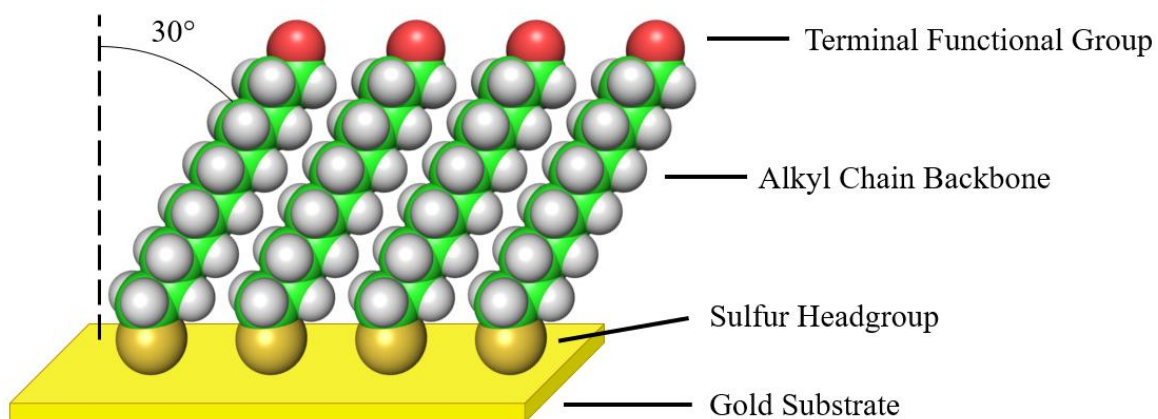


Figure 2.1: Schematic diagram of an ideal SAM of alkanethiolates on a flat gold surface.

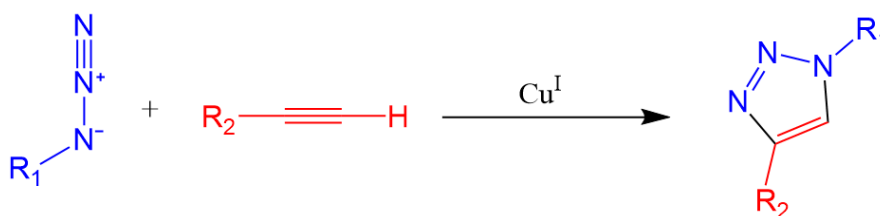
2.2 Click Chemistry

The term “click chemistry” describes a class of reactions characterized by their high yields, easily removable byproducts or no byproducts, versatility, stereospecificity, insensitivity to water and oxygen, readily available starting materials, and mild reaction conditions.³² The phrase “click” refers to the simple joining together of two molecular species that occurs in click chemistry processes. There are four general classifications of click chemistry reactions. The first and most widely used among the four classes are cycloadditions, specifically 1,3-dipolar and hetero-Diels Alder cycloadditions.³²⁻³⁴ Another popular class of click reactions are additions to carbon-carbon double and triple bonds, including epoxidations, aziridinations, and certain Michael addition reactions.³³⁻³⁴ The third class of click chemistry is non-aldol type carbonyl chemistry, such as the formation of ureas, hydrazones, oxime ethers, and amides.³²⁻³³ Lastly, the fourth category of click reactions are nucleophilic ring openings, in particular ring openings of strained heterocycles, including aziridines, epoxides, and cyclic sulfates.³⁵⁻³⁶

The unique properties of click reactions have led them to become invaluable tools across chemistry, biology, and medicinal sciences.³⁷ More specifically, they have found applications in synthetic chemistry, drug discovery and pharmaceuticals,³⁸ polymer

chemistry,³⁹ and biochemistry.⁴⁰ Furthermore, click chemistry has generated considerable interest in the field of material surface modifications, as it presents an efficient strategy for coupling organic species to surfaces. For example, various click chemistry reactions have been used to modify the surfaces of metallic nanoparticles⁴¹⁻⁴³ and silica particles,⁴⁴ the bilayer surfaces of mosaic viruses,⁴⁵ and the surfaces of large polymers,⁴⁶⁻⁴⁷ graphene sheets,⁴⁸ nanocrystalline diamond films,⁴⁹ and planar metallic substrates.⁵⁰⁻⁵¹

One click reaction in particular has garnered much attention for its utility in surface reactions. Since its introduction in the landmark review by Sharpless and coworkers in 2001,³² the copper (I)-catalyzed Huisgen alkyne-azide cycloaddition (CuAAC)⁵²⁻⁵³ has emerged as the quintessential example of click chemistry; currently one of the most commonly used click reactions available, the CuAAC has a diversity of applications in fields such as drug synthesis,³⁸ polymer functionalization,³⁹ biomolecule conjugation,⁴⁰ and surface modifications.⁵⁴ The CuAAC converts azide groups and terminal alkynes into biostable 1,4-disubstituted 1,2,3-triazole linkages via a copper-catalyzed mechanism at room temperature, as shown in Scheme 2.1. The reaction is rapid, efficient, regioselective, and is chemoselective against reactive species common to biological systems, meaning that, in the context of biochemical studies, unwanted side reactions with reactive chemical components native to biological environments may be avoided.⁵⁵ Because of its general usability and its compatibility with biochemical species, the CuAAC can provide the means to modifying SAMs of thiols on metallic surfaces with target biomolecules.



Scheme 2.1: General reaction scheme for the CuAAC reaction.

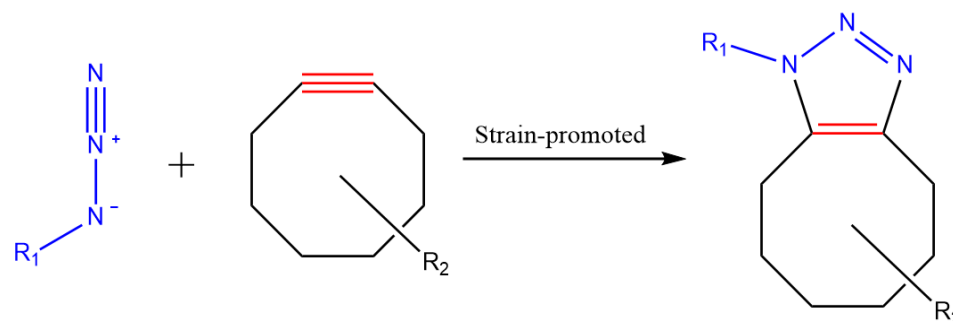
Such experiments have been previously published by several groups. For example, Brust and coworkers reported conjugation of lipase enzymes modified with acetylene to azide-functionalized gold nanoparticles (AuNPs) via CuAAC for the purpose of creating hybrid AuNP bioconjugates.⁵⁶ Jiang and coworkers presented a CuAAC-based assay for the

quantitative determination of protein concentrations, using azide- and alkyne-functionalized AuNPs.⁵⁷ Epple *et al.* reported synthesis of fully water-dispersible ultrasmall AuNPs functionalized with azide groups, and subsequent “click” of alkyne-bearing peptides.⁵⁸ Furthermore, they showed that their functionalized and “clicked” nanoparticles were able to penetrate the cell membrane, providing the opportunity for *in vivo* protein targeting and labelling.⁵⁸

Although the CuAAC is an effective and widely applicable reaction across multiple disciplines, there are some drawbacks associated with this method of surface functionalization. Most notably, the catalytically active Cu(I) ion is highly cytotoxic, which is detrimental to cell viability even if present in trace amounts.⁵⁹⁻⁶¹ This issue may be circumvented by employing the interfacial strain-promoted alkyne-azide cycloaddition (SPAAC), a version of the [3+2] Huisgen cycloaddition that occurs at room temperature and without the need for a copper catalyst.

2.2.1 The Strain-Promoted Alkyne-Azide Cycloaddition

The SPAAC reaction is an incredibly useful bio-orthogonal click process due to its chemoselectivity, biocompatibility, clean reactivity, and rapid kinetics.⁶² It can be described as a [3+2] Huisgen cycloaddition between an azide group and a cyclooctyne, as illustrated in Scheme 2.2. Although it had previously been shown that cyclooctynes, the smallest of the stable cycloalkynes, react rapidly with azides to form the triazole product,⁶³ Bertozzi and coworkers first showcased the SPAAC reaction as an alternative to the CuAAC in 2004 in a series of model reactions for the selective modification of biomolecules under physiological conditions, both *in vitro* and on living cells.⁶⁴ The driving force behind the SPAAC reaction is the strain imposed on the alkyne moiety by the eight-membered ring. The deformation of the acetylene bond angle to 163° in cyclooctyne⁶⁵ from its ideal 180° is responsible for approximately 18 kcal mol⁻¹ of ring strain energy.⁶⁶ This bond angle distortion destabilizes the carbon-carbon triple bond, lending the cyclooctyne its high reactivity and rapid rate acceleration compared to unstrained alkynes.⁶⁷



Scheme 2.2: General reaction scheme for the SPAAC reaction.

In the years since Bertozzi and coworkers' first use of the SPAAC reaction in a biological system, a wide range of cyclooctyne structural derivatives have been developed for the purpose of further enhancing the SPAAC reaction rate.⁶⁸⁻⁷⁰ For example, the addition of two aryl rings flanking the cyclooctyne to create 4-dibenzocyclooctyne (DIBO), as shown in Figure 2.2, has been found to drastically improve SPAAC reaction rates.⁷¹⁻⁷³ The aromatic rings on either side of the cyclooctyne in DIBO and DIBO analogues increase the ring strain and conjugate with the alkyne, boosting the reactivity of the alkyne in the SPAAC process.⁷³

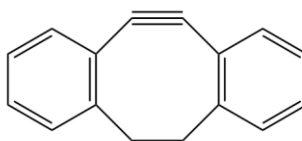


Figure 2.2: Diagram of the chemical structure of DIBO.

2.3 Preparation of Patterned Substrates by Microcontact Printing

In recent decades, great advances in microfabrication technology have revolutionized the fields of biotechnology, microelectronics, optoelectronics, and nanotechnology. Photolithography, the paragon example of microfabrication, is a highly developed and well-established technique that has contributed to all of these applications. However, conventional photolithography suffers from several drawbacks; the sophisticated equipment, complex facilities, and expensive materials required for photolithography make it an inherently expensive and, for some, inaccessible process. Furthermore, it is

limited to the use of only certain specific materials, providing very little control over the surface chemistry of the patterned substrates. Lastly, it is not applicable to nonplanar surfaces.

As a complementary system to photolithography, soft lithography extends the possibilities of photolithography to include a broader range of substrates and materials. So-called because of its use of mechanically soft and flexible components, soft lithography describes a family of techniques for microfabrication that employ patterned elastomeric molds, or “stamps”, to impart microstructures and patterns onto a variety of surfaces.⁷⁴⁻⁷⁶ Soft lithography, originally developed by Whitesides and Xia in 1998,⁷⁴⁻⁷⁶ presents a low cost, simple, and accessible means to produce chemically patterned surfaces. Amenable to a diverse range of materials and surfaces, these techniques deliver fine control over molecular-level detail and surface chemistry while enabling large-scale surface area coverage (up to several tens of cm²) with well-defined microscale and sub-micron patterning.⁷⁶⁻⁷⁸

One of the most common soft lithography methods is microcontact printing (μ CP). It is known for its simplicity, low cost, versatility, and ability to chemically pattern surfaces with high precision.^{74,76-78} The μ CP process, illustrated in Figure 2.3, is analogous to printing ink onto paper with a rubber stamp. In this methodology, microscale-patterned “stamps” of an elastomeric material, most often polydimethylsiloxane (PDMS), are used to transfer a pattern of functionalization onto a given substrate with a solution of the target molecule acting as the “ink”. PDMS is most commonly used for the stamp material because it is well-studied, non-toxic, readily commercially available and affordable, and, most importantly, its elastomeric character allows it to conform very well to a surface, achieving atomic-level contact.⁷⁷ This is an important feature for both the making of the stamp and its ability to effectively transfer its pattern. To create the stamp, liquid PDMS prepolymer is poured over a master pattern and then allowed to cure, as shown in Figure 2.3. Once cured, the PDMS stamp is peeled off the master pattern, revealing a complementary replica of the master. The stamp is then dipped in the molecular ink of choice to allow adsorption of the molecules to the PDMS. The inked stamp is dried and then brought into conformal contact with the substrate. The ink molecules are transferred

from the stamp to the substrate. The primary limitation of μ CP is that transfer efficiency is often less than 100%, resulting in some variation between experiments.

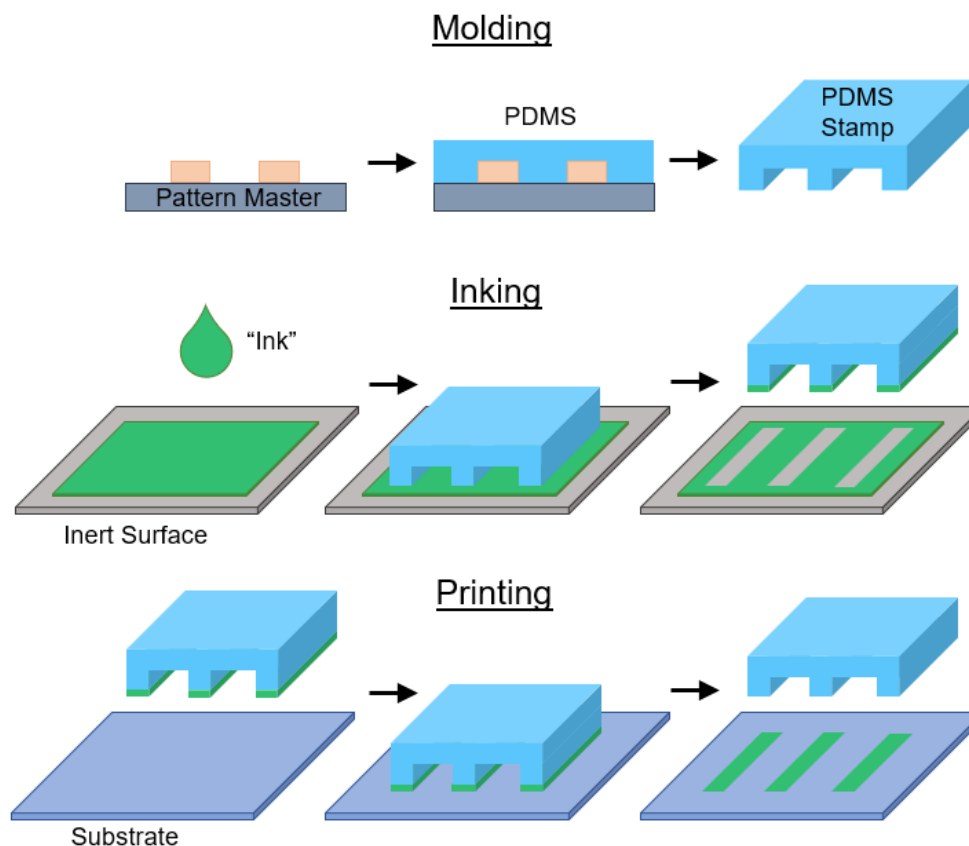


Figure 2.3: Schematic illustration of the microcontact printing technique.

As a simple and cost-effective method for microscale patterning, microcontact printing has found applications in optics⁷⁹, microelectronics⁸⁰, DNA⁸¹⁻⁸² and protein⁸³⁻⁸⁴ patterning, patterned cell adhesion,⁸⁵⁻⁸⁷ patterning of SAMs,⁸⁸⁻⁹⁰ and patterning of metallic nanostructures.⁹¹⁻⁹²

2.4 Plasmons

A plasmon is defined as the collective oscillation of delocalized electrons in a conductive material. This may alternatively be described as the concerted displacement of a negatively charged electron "cloud" with respect to a positively charged lattice. Plasmons that exist at the surface of a conductive material can interact with and absorb electromagnetic (EM) radiation with wavelengths corresponding to the frequency of the

oscillation, resulting in surface plasmon resonance (SPR). Because they can interact with external EM radiation, SPRs strongly influence the optical properties of some metals. The field of plasmonics, which seeks to control the coupling of light with free oscillating electrons at metal surfaces, takes advantage of optically excited surface plasmons and their properties for a variety of applications including optics,⁹³ photovoltaics,⁹⁴ spectroscopy and imaging, molecular sensing,⁹⁵ electronics,⁹⁶ and, most recently, the activation and catalysis of plasmon-mediated reactions.⁹⁷

2.4.1 Surface Plasmon Polaritons

The light-induced excitation of surface plasmons at the interface between a dielectric medium and a smooth planar metal surface results in the generation of surface plasmon polaritons (SPPs). This phenomenon was first observed by Wood in 1902, who reported uneven distribution of light in optical reflection measurements on metal diffraction gratings.⁹⁸ SPPs are a combination of surface EM waves that propagate along the metal-dielectric interface and associated surface charges,⁹⁹ as depicted in Figure 2.4a. Coupling between the surface plasmons and the oscillating electric field of light is most effective when the wavevector of the incident light is nearly parallel to the surface.¹⁰⁰

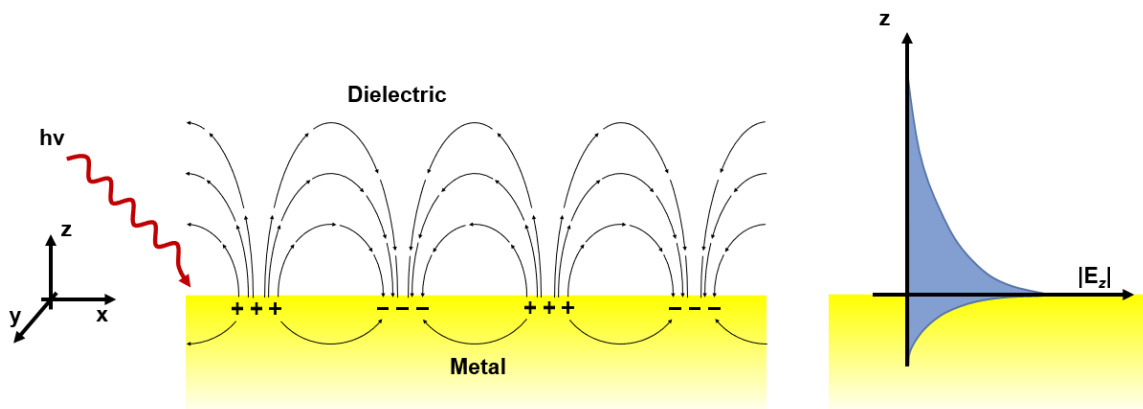


Figure 2.4: (a) Illustration of a propagating SPP at the interface between a planar metal surface and a dielectric material; (b) Representation of the strength of the electric field $|E_z|$ decaying exponentially in the z direction, away from the metal surface

The oscillation frequency of the electron density, and thus the wavelength of light that is able to excite surface plasmons, is highly dependent upon the type of metal, the surrounding dielectric material, and the size and shape of the metallic structure. SPP waves are tightly confined to the metal-dielectric interface, causing significant enhancement of the electric field at and very near the metal surface. The intensity of this electric field decays exponentially away from the metal surface,¹⁰¹ as shown in Figure 2.4b. The decay length into the dielectric medium is estimated by $\lambda/2n$ where λ is the wavelength of incident light and n is the refractive index of the dielectric.¹⁰²

Due to their unique and interesting properties, SPP-based structures and devices have found wide-ranging applications in optics,¹⁰⁰ biosensing and molecular sensing,¹⁰³ solar cells,¹⁰⁴ data storage,⁹⁹ and spectroscopy.

2.4.2 Localized Surface Plasmon Resonances

Light impinging on a metallic structure that is smaller than the photon wavelength may generate surface plasmon resonance that is non-propagating and confined to the vicinity of the metal structure. This localized surface plasmon resonance (LSPR) occurs when the collective oscillation of free electrons in a metallic nanoparticle (NP) is excited by EM radiation with a wavelength that corresponds to the frequency of electron oscillation.¹⁰⁵ The oscillation of conduction electrons with respect to the incident electric field creates an accumulation of charges at the surface of the NP. This process is shown in Figure 2.5. Metallic NPs are able to collect photons with wavelengths much larger than the NP itself and concentrate that energy into a very small area. Just as for SPPs, the intensity of the resulting electric field decays exponentially away from the metal surface. Confinement of the electric field to nanoscale regions on the metallic NP leads to “hotspots” of high intensity near-field enhancement. Furthermore, by placing a metallic NP within nanoscale distances of a metallic surface or another nanoparticle, even greater enhancement of the electric field may be produced in the nanogaps between structures.

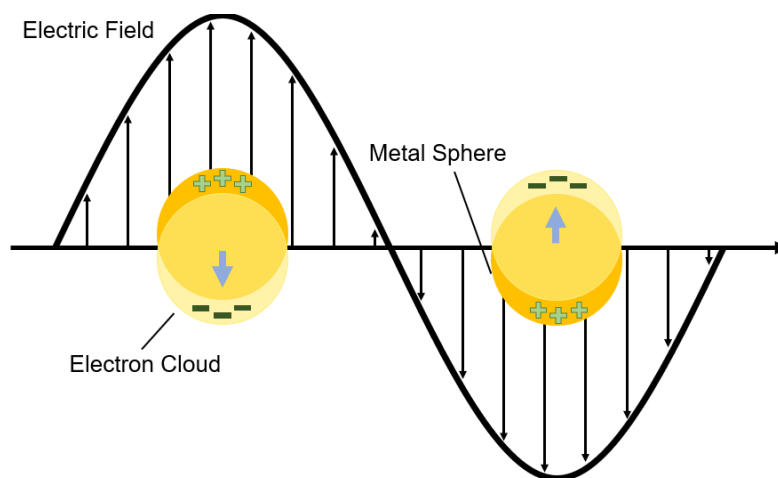


Figure 2.5: Diagram of localized surface plasmon resonance of a metallic nanoparticle induced by incident light.

The optical and plasmonic properties of metallic NPs depend heavily on the dielectric constants of the metal and the surroundings, as well as on the size and shape of the NPs. In 1857, Faraday discovered that by varying the diameters of spherical AuNPs in aqueous solution, it was possible to alter their resonance positions to afford AuNP solutions in an assortment of vibrant colours.¹⁰⁶ This serves to demonstrate the sensitivity of plasmonic NPs to changes in geometry. By fine-tuning the geometries of metallic NPs, their plasmonic properties may be tightly controlled. LSPR positions may also be controlled through choice of metal; plasmonic nanostructures are often made from coinage metals, in particular gold or silver, because the LSPR modes of nanostructures of these materials typically fall within the range of visible light.

Enhanced spectroscopy techniques such as surface-enhanced Raman spectroscopy, tip-enhanced Raman spectroscopy, surface-enhanced infrared absorption, and surface-enhanced fluorescence, each rely on the localized enhancement of incident electric fields and precise tunability of LSPR modes achievable with metallic NPs. LSPR-active NPs have also found use in lab-on-a-chip technology,¹⁰⁷ medical diagnostics,¹⁰⁸ and optical fiber sensors.¹⁰⁹ Over the past decade, however, the scope of LSPR applications has expanded to include plasmon-mediated chemical reactions (PMCRs) and processes.¹¹⁰

2.4.3 Plasmon-Mediated Chemistry

The concept of using optically excited surface plasmons to influence chemical reactions was first proposed and computationally modelled in 1981,¹¹¹ and then demonstrated experimentally for the first time in 1983.¹¹² Despite these early findings, the field of PMCRs did not truly burgeon until the late 2000's when studies by Tian and coworkers revealed that *p*-aminothiophenol (*p*-ATP) could be selectively oxidized into dimercaptoazobenzene (DMAB) on plasmonically active substrates under laser irradiation at room temperature.¹¹³⁻¹¹⁴ To date, this dimerization, as well as that of 4-nitrothiophenol (4-NTP) into DMAB, remain the most well-studied PMCRs and are often used as model systems for investigating plasmon-mediated reaction mechanisms.¹¹⁵⁻¹¹⁹

Although research interests in PMCRs have expanded in the last decade, the field is still relatively young and our physicochemical understanding of PMCRs and their reaction pathways is still very much incomplete. Growth in this field is strongly reliant on a thorough fundamental understanding of surface plasmons and the ways in which LSPRs can interact with chemical species. In addition to interacting with excited plasmons directly, PMCRs also often occur as a consequence of LSPR decay.¹²⁰ An excited surface plasmon only maintains its coherence for 1-10 fs,¹²¹ and relaxation of the LSPR follows one of two pathways: radiative decay or non-radiative decay.¹²² The LSPR relaxation process is illustrated in Figure 2.6. The radiative decay pathway simply involves re-emission of an absorbed photon by the plasmonic material.¹²² This is a rapid process, occurring within the first 1-100 fs of plasmon decay.¹¹⁰ Non-radiative decay of an excited surface plasmon generally occurs in three stages.¹²³⁻¹²⁴ In the first 1-100 fs, dephasing of the LSPR leads to the generation of excited, high-energy electron-hole pairs, or “hot carriers” with energies far above the Fermi level of the material.¹²⁵⁻¹²⁶ The hot electrons subsequently undergo electron-electron scattering interactions on the timescale of 100-1000 fs into the plasmon decay process, wherein the hot electrons transfer some of their energy to lower-energy electrons, creating multiple excited carriers. At this stage, hot carriers contain energies at or below the Fermi level of the material.¹²⁷⁻¹²⁸ Finally, the hot carriers relax fully through electron-phonon interactions, culminating in the release of thermal energy and local heat dissipation.¹²⁹⁻¹³⁰

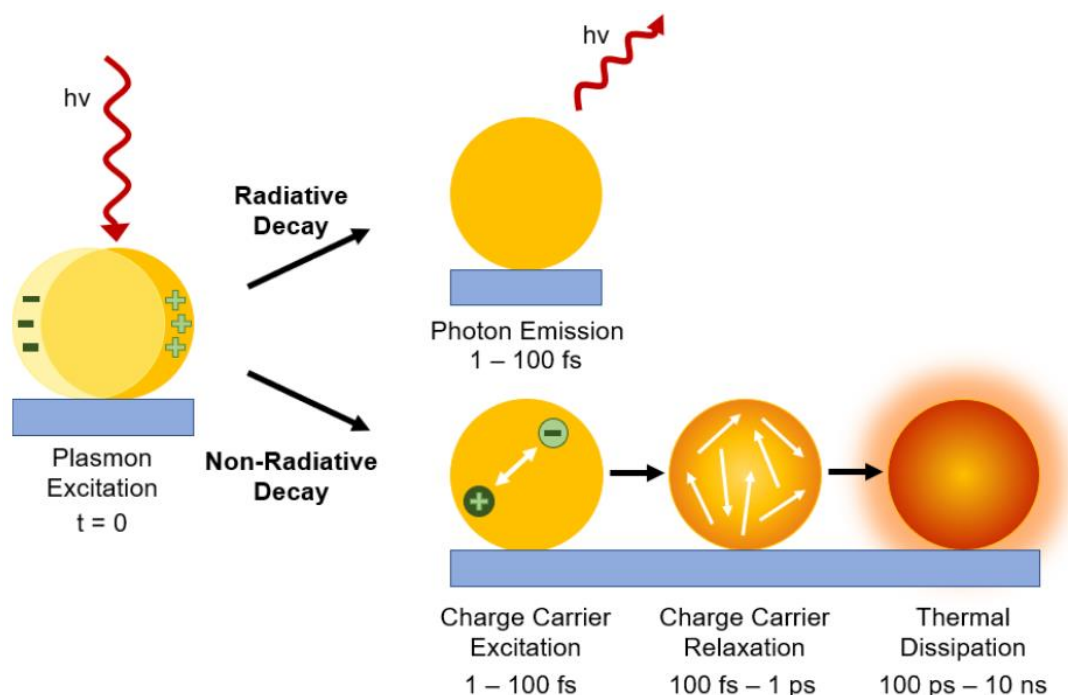


Figure 2.6: Photoexcitation and subsequent relaxation processes of an LSPR on a metallic nanoparticle.

Excited surface plasmons are able to mediate chemical processes either through local EM field enhancement, local heating effects, or injection of hot carriers into chemical species. While the local EM near-field enhancements associated with LSPRs are most commonly exploited for plasmon-enhanced spectroscopies, they have also been reported to contribute to the catalysis of some photoinduced reactions.¹³¹⁻¹³² The approach of using the near-field enhancement of LSPRs to catalyze reactions is generally applied to chemical processes that are triggered by light, as they are expected to benefit most from the localized concentration of light intensity.¹³³ The enhanced EM near-field enables increased light absorption as a result of increased light intensity, which in turn increases the probability of excitation of the reactants.¹³⁴ The most notable example of this is the 66-fold enhancement of photocatalytic water splitting, assisted by the plasmonic near-field under visible light irradiation.¹³⁵ Importantly, overlap of the plasmon resonance position, *i.e.* absorption of the plasmonic material, and the absorption spectrum of the reaction precursor is essential for EM field-mediated reactions to proceed efficiently.¹¹⁰

The local increase in temperature that occurs as a side effect of late-stage LSPR relaxation has frequently been used as a means to provide localized energy for chemical reactions.¹³² The ability of plasmonically active materials to generate heat in response to incident visible light presents many unique advantages, as it allows nanoscale heating confined to specific locations, and also enables the possibility of solvent superheating through efficient heat transfer to solution.¹³³ For example, Branda and coworkers employed the photothermal effects of AuNPs for the controlled release of fluorescein dye via a retro Diels-Alder reaction,¹³⁶ a process for which temperature control is crucial for proper initiation.¹³⁷ The photothermal effects of LSPR decay have also been utilized by Scaiano and coworkers for the decomposition of dicumyl peroxide.¹³⁸ LSPR photothermal enhancement was pursued for this reaction because of the relatively harsh thermal conditions required for the reaction to proceed otherwise (~ 140 °C).¹³⁸ Scaiano also later demonstrated the LSPR photothermally enhanced Friedel-Crafts alkylation of anisole using AuNPs supported by Nb₂O₅.¹³⁹

Transfer of hot carriers, either directly or indirectly, from a plasmonic material to nearby chemical species is among the most prevalent of the proposed mechanisms for PMCRs. The first steps of non-radiative LSPR decay involve the excitation of hot electrons and hot holes, and the subsequent generation of multiple hot electrons through electron-electron interactions.¹²⁵⁻¹²⁸ In the direct charge transfer (CT) process, LSPR decay takes an alternative pathway wherein, instead of producing a hot electron at the surface of the plasmonic nanostructure, decay occurs through an interfacial electron transfer directly from the nanostructure to the lowest unoccupied molecular orbital (LUMO) of the nearby chemical species.¹⁴⁰⁻¹⁴¹ Direct injection of hot carriers into molecules at the instant of plasmon dephasing requires a strong interaction between the molecular species and the metallic nanostructure.¹⁴⁰ The direct transfer mechanism is not often observed, as this strong interaction between the metal and chemical species is not common.¹³² More common than this is the indirect transfer mechanism. This pathway involves the donation of electrons from the first and second stages of non-radiative LSPR decay, once hot electrons have been excited on the metal surface and some have relaxed to lower energies through electron-electron interactions. Like in the direct transfer process, hot electrons are donated to the LUMO of the molecule. The direct and indirect CT processes are

portrayed in Figure 2.7. Each pathway requires the metal nanostructures and the chemical reactants to overlap both spatially and energetically to allow transfer of charges. The donation of high-energy hot electrons to the empty orbitals of molecules can lead to the breaking of bonds or to the formation of new bonds.

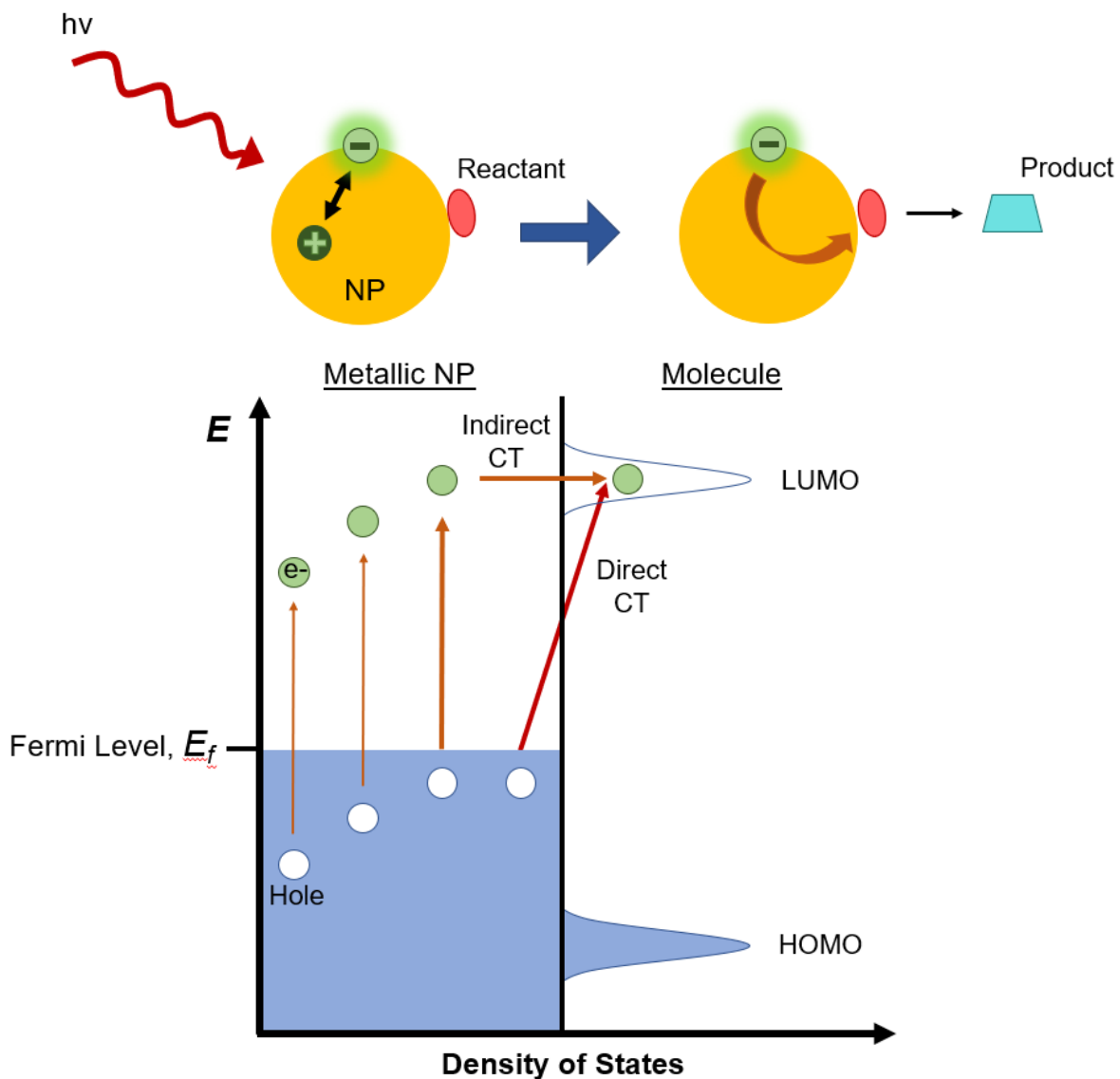


Figure 2.7: Direct and indirect CT-driven PMCRs.

There are numerous examples of known CT-driven chemical reactions. The previously mentioned dimerizations of *p*-ATP and 4-NTP into DMAB have both been shown to proceed via transfer of hot electrons from the metallic nanostructure to the adsorbed molecules.^{110,113-114} Yoon and coworkers recently reported the plasmon-driven

decarboxylation of 4-mercaptobenzoic acid into benzenethiol on AuNPs, and deduced a mechanism that involves the transfer of both hot electrons and hot holes to the organic species.¹⁴² One chemical mechanism for CT-driven PMCRs that is commonly proposed suggests that some PMCRs may actually be induced by reactive oxygen species that are generated through hot electron donation to O₂ at the plasmonic surface.¹⁴³⁻¹⁴⁴ For example, Takeyasu *et al.* performed the plasmon-mediated oxidation of 1-butanethiol to introduce an alkene moiety, and indicated that plasmon-generated reactive oxygen species are critical for this PMCR to proceed.¹⁴⁵ A prominent PMCR of interest is the plasmon-mediated grafting of various diazonium salts to plasmonically-active metal nanostructures, as it allows controllable and highly localized surface modification of nanostructures, and diazonium salts offer a wide range of terminal functional groups.¹⁴⁶⁻¹⁴⁷ This reaction also grants the opportunity for multi-functionalization by exploiting different plasmon modes of the nanostructures.¹⁴⁶ These reactions will be discussed in further detail in Chapter 4 of this thesis.

Because the near-field enhancement, local heating, and hot carrier injection mechanisms for PMCRs are each so closely related and not necessarily mutually exclusive, it can be challenging to determine which process or processes are responsible for driving a particular plasmon-mediated reaction forward. Furthermore, short-lived reaction intermediates for these reactions are not easy to isolate or detect. For this reason, critical information on the chemical reaction steps mediated by hot carriers is largely unknown and difficult to study.¹²⁰ However, there are some spectroscopic methods that may be employed to probe PMCRs. Conveniently, the same plasmonic platforms on which PMCRs can be performed may also be used simultaneously for plasmon-enhanced detection methods, such as surface-enhanced Raman spectroscopy. Surface-enhanced Raman spectroscopy is a vibrational spectroscopic technique that, under the proper conditions, can deliver structural information on longer-lived reaction intermediates and the vibrational states of molecules, and in some cases can provide time-resolved characterization of PMCRs through simultaneous spectral acquisition and plasmon-mediated activation of the reaction under study.¹⁴⁸⁻¹⁴⁹

2.5 Raman Spectroscopy

Interactions between light and matter can give rise to a host of different physical and chemical processes. Typically, light that strikes matter is either transmitted, reflected, absorbed, or scattered. When light is scattered by a molecule or particle of interest, the oscillating EM field of the incident photon induces an oscillating dipole in the molecule which promotes the molecule to a high-energy virtual state.¹⁵⁰ This virtual state is unstable, so the photon is immediately re-emitted as scattered light.¹⁵⁰ In the vast majority of scattering events, the light is scattered elastically, meaning that the re-emitted photon has the same energy as that of the incident photon. The elastic scattering process is known as Rayleigh scattering. However, one in every 10^8 scattered photons is scattered inelastically, such that there is a transfer of energy between the photon and the molecule resulting in a re-emitted photon that is of a different wavelength than the incident light.¹⁵¹ This phenomenon is known as the Raman effect, first observed by Sir C.V. Raman in 1928 – a discovery that earned him the Nobel Prize in Physics in 1930.¹⁵²⁻¹⁵³ When the photon loses energy to the molecule, the molecule relaxes from its virtual state to an excited vibrational energy level, and the re-emitted photon of lower energy is referred to as Stokes shifted. Conversely, when the photon gains energy from the molecule, the molecule relaxes from its virtual state down to a lower vibrational energy level, and the re-emitted higher-energy photon is referred to as anti-Stokes shifted. Each of these three scattering processes are illustrated in Figure 2.8.

Raman spectroscopy is an analytical technique that collects information on the chemical and structural properties of materials using inelastically scattered light. Because the energy differences between the incident and inelastically scattered photons correspond to the vibrational energy levels of the irradiated species, Raman spectroscopy allows observation of the vibrational modes of molecules and characterization of molecules through their vibrational fingerprints. In this way, Raman spectroscopy is a complementary system to Fourier Transform Infrared (FTIR) spectroscopy; while FTIR spectroscopy is based on light absorption and detects vibrational modes associated with a change in the dipole moment of a molecule, Raman spectroscopy collects inelastically scattered light and detects vibrational modes associated with a change in polarizability.

Raman spectroscopy allows investigation of molecular vibrations that are not visible in FTIR spectra due to these different selection rules.

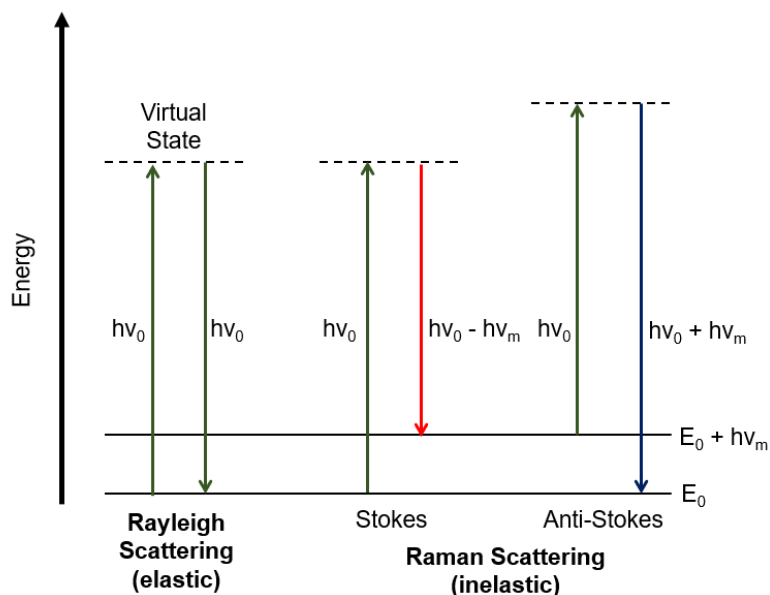


Figure 2.8: Energy diagram depicting the Rayleigh, Stokes, and anti-Stokes scattering processes.

Generally, Raman spectroscopy measures Stokes shifts rather than anti-Stokes shifts. This is because anti-Stokes shifts require the irradiated molecule to already occupy an excited vibrational energy level in order to have energy available for transfer to the incident photon. Since the great majority of molecules exist in their ground state under ambient conditions according to the Boltzmann distribution,¹⁵⁴ Stokes scattering is statistically much more likely to occur than anti-Stokes scattering, and so the Stokes scattering is always more intense. Although Raman spectroscopy is a useful technique for materials characterization, Rayleigh scattering is by far the more dominant scattering process over Stokes and anti-Stokes. The greatest limitation of Raman spectroscopy is its intrinsic weak signal intensity and low sensitivity caused by the poor scattering cross section of materials for Raman scattering. One way to overcome this limitation is to enhance the Raman signal using surface-enhanced Raman spectroscopy (SERS).

2.5.1 Surface-Enhanced Raman Spectroscopy

SERS is a spectroscopic technique that exploits the plasmonic properties of metallic nanostructures in order to enhance the Raman scattering of materials near or at the metal surface. The first recorded instance of the SERS effect was an accidental discovery by McQuillan and coworkers in 1974 in an experiment involving Raman spectroscopic measurements on pyridine molecules adsorbed onto a roughened silver electrode.¹⁵⁵⁻¹⁵⁶ At the time, the mechanism behind the observed dramatic enhancement of the Raman signal intensity was not fully understood. Subsequent similar experiments by Creighton¹⁵⁷ and Van Duyne¹⁵⁸ in the late 70's served to elucidate the true processes by which the Raman signal enhancement occurred. Today, SERS has emerged as a powerful analytical tool for the highly sensitive detection of molecules adsorbed onto metallic nanostructures.

The total SERS enhancement comprises two primary contributions: the EM enhancement mechanism and the chemical enhancement mechanism.¹⁵⁹ The EM mechanism stems directly from the LSPRs of metallic nanostructures. LSPR arises when a metallic nanostructure is irradiated with light of a frequency that corresponds to the frequency of electron oscillations in the metal.¹⁰⁵ This ultimately results in hotspots of strong near-field enhancement collecting at the edges of the metallic nanostructure. The Raman scattering cross section of materials is dependent on the strength of the local field, $|E_{loc}|$, which is the near-field at the location of molecules on the nanostructure surface.¹⁶⁰ This enhanced local field acts on both the incident and scattered rays; thus, the overall Raman scattering cross section is elastically enhanced by enhancement factor M which may be expressed as a product of the two enhancements, as shown in equation (2.1):¹⁶¹

$$M = \frac{|E_{loc}(\omega_I)|^2}{|E_0|^2} \cdot \frac{|E_{loc}(\omega_R)|^2}{|E_0|^2} \quad (2.1)$$

Here, E_{loc} is the local near-field, ω_I is the frequency of the incident light, ω_R is the frequency of the Raman scattered light, and E_0 is the electric field of the incident beam. Since the frequencies of molecular vibrations are generally much smaller than the frequency of visible light, $|E_{loc}(\omega_R)|^2$ can be considered similar enough to $|E_{loc}(\omega_I)|^2$ that the following approximation can be made:¹⁶²

$$M = \frac{|E_{loc}(\omega_I)|^4}{|E_0|^4} \quad (2.2)$$

The scaling of M to the fourth power dramatically increases the sensitivity of the SERS technique for molecules located near plasmonic hotspots, even down to single molecule detection.¹⁶³ As the main contributor to SERS intensity, the EM enhancement factor is responsible for enhancement of the Raman signal by a factor of up to 10^{10} .¹⁶⁴ Meanwhile, the chemical enhancement mechanism of SERS can increase the Raman signal by a factor of 10^2 to 10^4 .¹⁶⁵⁻¹⁶⁶

Unlike the EM enhancement mechanism, which relies on the plasmonic properties of the SERS substrate, the chemical enhancement mechanism of SERS is dependent upon the molecule under study.¹⁶⁷ What is referred to as the “chemical mechanism” is in fact a combination of three different enhancement processes: direct or indirect charge transfer, resonance Raman, and non-resonance Raman enhancements.¹⁶⁸ In each case, interactions between the metallic nanostructure and the absorbed species serve to influence the polarizability of the molecule, which in turn affects its Raman scattering cross section, enabling enhancement of the overall SERS signal.^{160,169} Whether these mechanisms occur and to what degree they enhance the SERS signal is dependent on the properties of the molecular species.¹⁶⁸ These interactions, particularly charge transfers from the substrate to the adsorbed material, are closely related to PMCR processes.¹¹⁰ The major difference is that in PMCRs, the hot carriers are donated completely to the chemical species, whereas in the SERS chemical enhancement mechanism, the excited carriers that are transferred to the adsorbed species quickly decay back to the metal surface, causing resonance-like enhancement of the Raman signal.¹¹⁹

2.6 Fourier Transform Infrared Spectroscopy

FTIR spectroscopy is a technique of high spectral resolution used extensively in all branches of chemistry to characterize and identify molecules through their vibrational fingerprints. Vibrational modes that are associated with a change in the dipole moment of a given dipole mode with respect to the normal coordinates of the bond will selectively absorb wavelengths of infrared (IR) light that correspond to the frequency of the

vibration. The IR spectrum of a given sample can provide information on the molecular orientation, conformational regularity, and types of atoms and bonds in the molecule.¹⁷⁰

While FTIR spectroscopy is a very common analytical technique with widespread use in many fields, it can sometimes require large quantities of sample, up to several milligrams, to obtain a quality spectrum. This is a severe limitation for research at the nanoscale, as some configurations for FTIR spectroscopy lack the sensitivity to study thin films. Fortunately, there are a number of different FTIR setup arrangements designed for the study of surface adsorbates with high sensitivity down to the single monolayer. One such variation of classical FTIR spectroscopy is polarization modulation infrared-reflection absorption spectroscopy (PM-IRRAS), a powerful chemical analysis technique dedicated specifically for the qualitative and quantitative study of organic monolayers and thin films.

2.6.1 Polarization Modulation Infrared Reflection-Absorption Spectroscopy

In conventional FTIR studies, the IR beam incident upon the sample is randomly polarized. When the beam is linearly polarized, however, only vibrational modes of the sample with a component of their dipole moment oriented parallel to the plane of polarization will be able to absorb the IR light and contribute to the spectrum. Samples that are gaseous, liquid, or in solution possess a rotational degree of freedom, and as a result the orientation of all dipole moments in the sample are constantly changing; their polarized spectra are therefore identical, independent of the orientation of the linearly polarized IR light incident upon the sample.¹⁷¹ Conversely, molecules that are deposited as thin films adsorbed onto a surface maintain a fixed orientation over time. Furthermore, SAMs often tend to adopt a particular molecular conformation and uniform bond orientations at surfaces and interfaces.^{5,172} This phenomenon lends SAMs a directional dependence and an overall uniform macroscopic conformation. Such samples exhibit anisotropy, wherein their physical properties differ when measured along different molecular axes. Thus, anisotropic thin films and monolayers can be characterized in terms of the chemical composition and bond orientations of the system using distinct orientations of linearly polarized IR light. One particular technique that takes advantage

of this property is infrared reflection-absorption spectroscopy (IRRAS), an established and reliable method for characterizing thin films adsorbed onto highly reflective metallic substrates.¹⁷³ IRRAS experiments are typically carried out by collecting the reflectance spectrum of a thin film with IR light that is linearly polarized parallel to the plane of incidence and then normalizing this measurement with respect to the reflectance spectrum of the “bare” (non-functionalized) substrate.¹⁷⁴ This technique offers relatively high sensitivity, and the use of linearly polarized IR light provides information about the bond orientations of surface molecules.

PM-IRRAS is based on some of the same principles as IRRAS experiments, but with several crucial improvements. While IRRAS uses light that is linearly polarized along one direction, PM-IRRAS utilizes a polarized beam of light that is modulated between two states. During acquisition, the orientation of the linearly polarized IR beam is rapidly modulated between two orthogonal polarizations, parallel (p-polarized) and perpendicular (s-polarized) to the plane of incidence. This rapid modulation is achieved using a photoelastic modulator (PEM) placed between a linear polarizer and the substrate.

One of the greatest advantages of this modulation technique is the surface selection rule. This rule states that only p-polarized light may interact with surface molecules, and only vibrational modes with a component of the transition dipole moment aligned parallel to the plane of incidence may contribute to the absorbance spectrum.^{173,175} This is a direct result of the physics of the reflection of light from a metal surface. In PM-IRRAS experiments, the IR beam is directed at the substrate at a grazing incidence of 80° . S-polarized light undergoes a phase change of 180° regardless of the angle of incidence.^{173,175} This creates a node in the electromagnetic field at the substrate surface that prevents surface molecules from interacting with this polarization of light.¹⁴ However, when light is p-polarized and the angle of incidence is high, the electric field vector undergoes a phase change of less than 90° .^{173,175} This allows the incident and reflected rays to constructively interfere to form a standing wave at the substrate surface.¹⁷⁵ Vibrational modes that are parallel to this standing wave can contribute to the absorbance spectrum. This surface selection rule is illustrated in Figure 2.9. PM-IRRAS does not collect the individual polarized spectra, but instead takes the difference between

the p-polarized and s-polarized reflectances and normalizes this with respect to the sum of these reflectances. This differential measurement not only contributes to the high sensitivity of this technique and provides information about the orientation of the vibrational modes of surface molecules, but also allows measurements to be taken in atmosphere. Because they have no macroscopic uniform orientation, non-surface molecules absorb the p- and s-polarized light equally and thus when the difference is taken, the absorbances are cancelled. For this reason, PM-IRRAS is insensitive to the surrounding atmospheric gases since they absorb IR light isotropically. Furthermore, PM-IRRAS measurements are made quantitative through use of a spectral calibration procedure developed by Buffeteau *et al.*,¹⁷⁶⁻¹⁷⁷ details for which can be found in Appendix A.

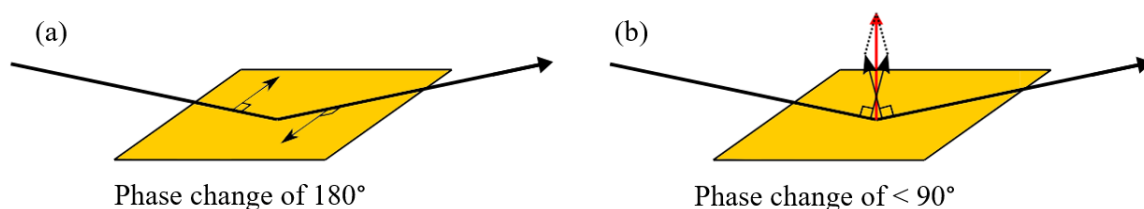


Figure 2.9: Illustration of the phase change of (a) s-polarized light and (b) p-polarized light upon reflection from a metallic surface.

2.7 Summary

This chapter outlines key relevant approaches to surface modification, including click chemistry, plasmon-mediated chemistry, and microcontact printing. Also provided in this chapter is detailed exposition on the physical principles underlying select vibrational spectroscopic techniques, namely SERS and PM-IRRAS, for the characterization of monolayers and thin films.

2.8 References

1. Schwartz, D. K. *Annu. Rev. Phys. Chem.* **2001**, *52*, 107-137.
2. Buschow, K. H. J.; Cahn, R. W.; Flemings, M. C.; Ilshner, B.; Kramer, E. J.; Mahajan, S.; Veyssi re, P. *Encyclopedia of Materials: Science and Technology*, Elsevier: Oxford, 2001; pp 9332-9344.
3. Casalini, S.; Bortolotti, C. A.; Leonardi, F.; Biscarini, F. *Chem. Soc. Rev.* **2017**, *46*, 40-71.
4. Ulman, A. *Chem. Rev.* **1996**, *96*, 1533-1554.
5. Love, J. C.; Estroff, L. A.; Kriebel, J. K.; Nuzzo, R. G.; Whitesides, G. M. *Chem. Rev.* **2005**, *105*, 1103-1169.
6. Ferretti, S.; Paynter, S.; Russell, D. A.; Sapsford, K. E.; Richardson, D. J. *Trends Anal. Chem.* **2000**, *19*, 530-540.
7. Cho, W. K.; Park, S.; Jon, S.; Choi, I. S. *Nanotechnology* **2007**, *18*, 395602.
8. Nakano, M.; Ishida, T.; Sano, H.; Sugimura, H.; Miyake, K.; Ando, Y.; Sasaki, S. *Appl. Surf. Sci.* **2008**, *255*, 3040-3045.
9. Vericat, C.; Vela, M. E.; Benitez, G.; Carro, P.; Salvarezza, R. C. *Chem. Soc. Rev.* **2010**, *39*, 1805-1834.
10. Bhushan, B.; Kasai, T.; Kulik, G.; Barbieri, L.; Hoffmann, P. *Ultramicroscopy* **2005**, *105*, 176-188.
11. Rajkumar, G.; Sethuraman, M. G. *Thin Solid Films* **2014**, *562*, 32-36.
12. Huo, L.; Du, P.; Zhang, K.; Liu, P.; Zhou, H. *Appl. Surf. Sci.* **2019**, *477*, 96-103.
13. Paul, J.; Meltzer, C.; Braunschweig, B.; Peukert, W. *Langmuir* **2016**, *32*, 8298-8306.

14. Huisman, B.-H.; Kooyman, R. P. H.; van Veggel, F. C. J. M.; Reinhoudt, D. N. *Adv. Mater.* **1996**, *8*, 561-564.
15. Wang, Y.-S.; Yau, S.; Chau, L.-K.; Mohamed, A.; Huang, C.-J. *Langmuir* **2019**, *35*, 1652-1661.
16. Wink, T.; van Zuilen, S. J.; Bult, A.; van Benkom, W. P. *Analyst* **1997**, *122*, 43R-50R.
17. Raigoza, A. F.; Fies, W.; Lim, A.; Onyirioha, K.; Webb, L. J. *Appl. Surf. Sci.* **2017**, *394*, 288-296.
18. Wilbur, J. L.; Kumar, A.; Biebuyck, H. A.; Kim, E.; Whitesides, G. M. *Nanotechnology* **1996**, *7*, 452-457.
19. Maoz, R.; Frydman, E.; Cohen, S. R.; Sagiv, J. *Adv. Mater.* **2000**, *12*, 424-429.
20. Zeira, A.; Berson, J.; Feldman, I.; Maoz, R.; Sagiv, J. *Langmuir* **2011**, *27*, 8562-8575.
21. Nuzzo, R. G.; Allara, D. L. *J. Am. Chem. Soc.* **1983**, *105*, 4481-4483.
22. Bain, C. D.; Troughton, E. B.; Tao, Y. T.; Evall, J.; Whitesides, G. M.; Nuzzo, R. G. *J. Am. Chem. Soc.* **1989**, *111*, 321-335.
23. Pensa, E.; Cortés, E.; Corthey, G.; Carro, P.; Vericat, C.; Fonticelli, M. H.; Benítez, G.; Rubert, A. A.; Salvarezza, R. C. *Acc. Chem. Res.* **2012**, *45*, 1183-1192.
24. Burgi, T. *Nanoscale* **2015**, *7*, 15553-15567.
25. Häkkinen, H. *Nat. Chem.* **2012**, *4*, 443-455.
26. Laibinis, P. E.; Whitesides, G. M.; Allara, D. L.; Tao, Y. T.; Parikh, A. N.; Nuzzo, R. G. *J. Am. Chem. Soc.* **1991**, *113*, 7152-7167.

27. Cheng, F.; Li, M.; Zhao, X.; Wang, H.; He, W.; Hua, X.; Wang, Q.; Qu, J. *Biointerphases* **2018**, *13*, 06E407.
28. Holzer, B.; Manoli, K.; Ditaranto, N.; Macchia, E.; Tiwari, A.; Di Franco, C.; Scamarcio, G.; Palazzo, G.; Torsi, L. *Adv. Biosyst.* **2017**, *1*, 1700055.
29. Raigoza, A. F.; Onyirioha, K.; Webb, L. J. *Appl. Surf. Sci.* **2017**, *396*, 1831-1839.
30. Schmaltz, T.; Sforazzini, G.; Reichert, T.; Frauenrath, H. *Adv. Mater.* **2017**, *29*, 1605286.
31. Zheng, H.; Zhang, F.; Zhou, N.; Sun, M.; Li, X.; Xiao, Y.; Wang, S. *Org. Electron.* **2018**, *56*, 89-95.
32. Kolb, H. C.; Finn, M. G.; Sharpless, K. B. *Angew. Chem. Int. Ed.* **2001**, *40*, 2004-2021.
33. Hein, C. D.; Liu, X. M.; Wang, D. *Pharm. Res.* **2008**, *25*, 2216-2230.
34. Kolb, H. C.; Sharpless, K. B. *Drug Discov. Today* **2003**, *8*, 1128-1137.
35. Chandrasekhar, M.; Sekar, G.; Singh, V. K. *Tetrahedron Lett.* **2000**, *41*, 10079-10083.
36. Kashemirov, B. A.; Bala, J. L.; Chen, X.; Ebetino, F. H.; Xia, Z.; Russell, R. G.; Coxon, F. P.; Roelofs, A. J.; Rogers, M. J.; McKenna, C. E. *Bioconjugate Chem.* **2008**, *19*, 2308-2310.
37. Moses, J. E.; Moorhouse, A. D. *Chem. Soc. Rev.* **2007**, *36*, 1249-1262.
38. Lee, L. V.; Mitchell, M. L.; Huang, S. J.; Fokin, V. V.; Sharpless, K. B.; Wong, C. H. *J. Am. Chem. Soc.* **2003**, *125*, 9588-9589.
39. Binder, W. H.; Sachsenhofer, R. *Macromol. Rapid Commun.* **2008**, *29*, 1097-1103.

40. Nwe, K.; Brechbiel, M. W. *Cancer Biother. Radiopharm.* **2009**, *24*, 289-302.
41. Li, M.; Xu, L. Q.; Wang, L.; Wu, Y. P.; Li, J.; Neoh, K.-G.; Kang, E.-T. *Polym. Chem.* **2011**, *2*, 1312-1321.
42. White, M. A.; Johnson, J. A.; Koberstein, J. T.; Turro, N. J. *J. Am. Chem. Soc.* **2006**, *128*, 11356-11357.
43. Zhou, Y.; Wang, S.; Zhang, K.; Jiang, X. *Angew. Chem. Int. Ed.* **2008**, *47*, 7454-7456.
44. Ranjan, R.; Brittain, W. J. *Macromolecules* **2007**, *40*, 6217-6223.
45. Bruckman, M. A.; Kaur, G.; Lee, L. A.; Xie, F.; Sepulveda, J.; Breitenkamp, R.; Zhang, X.; Joralemon, M.; Russell, T. P.; Emrick, T.; Wang, Q. *ChemBiochem* **2008**, *9*, 519-523.
46. Belbekhouche, S.; Guerrouache, M.; Carbonnier, B. *Macromol. Chem. Phys.* **2016**, *217*, 997-1006.
47. Pauloehrl, T.; Delaittre, G.; Winkler, V.; Welle, A.; Bruns, M.; Borner, H. G.; Greiner, A. M.; Bastmeyer, M.; Barner-Kowollik, C. *Angew. Chem. Int. Ed.* **2012**, *51*, 1071-1074.
48. Wang, H. X.; Zhou, K. G.; Xie, Y. L.; Zeng, J.; Chai, N. N.; Li, J.; Zhang, H. L. *Chem. Commun.* **2011**, *47*, 5747-5749.
49. Davydova, M.; de los Santos Pereira, A.; Bruns, M.; Kromka, A.; Ukraintsev, E.; Hirtz, M.; Rodriguez-Emmenegger, C. *RSC Adv.* **2016**, *6*, 57820-57827.
50. Williams, M. G.; Teplyakov, A. V. *Appl. Surf. Sci.* **2018**, *447*, 535-541.
51. Xu, L. Q.; Wan, D.; Gong, H. F.; Neoh, K.-G.; Kang, E.-T.; Fu, G. D. *Langmuir* **2010**, *26*, 15376-15382.

52. Rostovtsev, V. V.; Green, L. G.; Fokin, V. V.; Sharpless, K. B. *Angew. Chem. Int. Ed.* **2002**, *41*, 2596-2599.
53. Tornøe, C. W.; Christensen, C.; Meldal, M. *J. Org. Chem.* **2002**, *67*, 3057-3064.
54. Orski, S. V.; Sheppard, G. R.; Arumugam, S.; Arnold, R. M.; Popik, V. V.; Locklin, J. *Langmuir* **2012**, *28*, 14693-14702.
55. Lallana, E.; Sousa-Herves, A.; Fernandez-Trillo, F.; Riguera, R.; Fernandez-Megia, E. *Pharm. Res.* **2012**, *29*, 1-34.
56. Brennan, J. L.; Hatzakis, N. S.; Tshikhudo, T. R.; Razumas, V.; Patkar, S.; Vind, J.; Svendsen, A.; Nolte, R. J. M.; Rowan, A. E.; Brust, M. *Bioconjugate Chem.* **2006**, *17*, 1373-1375.
57. Zhu, K.; Zhang, Y.; He, S.; Chen, W.; Shen, J.; Wang, Z.; Jiang, X. *Anal. Chem.* **2012**, *84*, 4267-4270.
58. van der Meer, S. B.; Loza, K.; Wey, K.; Heggen, M.; Beuck, C.; Bayer, P.; Epple, M. *Langmuir* **2019**, *35*, 7191-7204.
59. Lallana, E.; Riguera, R.; Fernandez-Megia, E. *Angew. Chem. Int. Ed.* **2011**, *50*, 8794-8804.
60. Li, S.; Cai, H.; He, J.; Chen, H.; Lam, S.; Cai, T.; Zhu, Z.; Bark, S. J.; Cai, C. *Bioconjugate Chem.* **2016**, *27*, 2315-2322.
61. Li, S.; Wang, L.; Yu, F.; Zhu, Z.; Shobaki, D.; Chen, H.; Wang, M.; Wang, J.; Qin, G.; Erasquin, U. J.; Ren, L.; Wang, Y.; Cai, C. *Chem. Sci.* **2017**, *8*, 2107-2114.
62. Patterson, D. M.; Prescher, J. A. *Curr. Opin. Chem. Biol.* **2015**, *28*, 141-149.
63. Wittig, G.; Krebs, A. *Chem. Ber.* **1961**, *94*, 3260-3275.

64. Agard, N. J.; Prescher, J. A.; Bertozzi, C. R. *J. Am. Chem. Soc.* **2004**, *126*, 15046-15047.
65. Meier, H.; Petersen, H.; Kolshorn, H. *Chem. Ber.* **1980**, *113*, 2398-2409.
66. Turner, R. B.; Jarrett, A. D.; Goebel, P.; Mallon, B. J. *J. Am. Chem. Soc.* **1973**, *95*, 790-792.
67. Shea, K. J.; Kim, J. S. *J. Am. Chem. Soc.* **1992**, *114*, 4846-4855.
68. Debets, M. F.; van Berkel, S. S.; Schoffelen, S.; Rutjes, F. P.; van Hest, J. C.; van Delft, F. L. *Chem. Commun.* **2010**, *46*, 97-99.
69. Sletten, E. M.; Nakamura, H.; Jewett, J. C.; Bertozzi, C. R. *J. Am. Chem. Soc.* **2010**, *132*, 11799-11805.
70. Varga, B. R.; Kallay, M.; Hegyi, K.; Beni, S.; Kele, P. *Chemistry* **2012**, *18*, 822-828.
71. Debets, M. F.; Prins, J. S.; Merckx, D.; van Berkel, S. S.; van Delft, F. L.; van Hest, J. C.; Rutjes, F. P. *Org. Biomol. Chem.* **2014**, *12*, 5031-5037.
72. Jewett, J. C.; Sletten, E. M.; Bertozzi, C. R. *J. Am. Chem. Soc.* **2010**, *132*, 3688-3690.
73. Ning, X.; Guo, J.; Wolfert, M. A.; Boons, G. J. *Angew. Chem. Int. Ed.* **2008**, *47*, 2253-2255.
74. Xia, Y.; Whitesides, G. M. *Angew. Chem. Int. Ed. Engl.* **1998**, *37*, 550-575.
75. Xia, Y.; Whitesides, G. M. *Annu. Rev. Mater. Sci.* **1998**, *28*, 153-184.
76. Zhao, X.-M.; Xia, Y.; Whitesides, G. M. *J. Mater. Chem.* **1997**, *7*, 1069-1074.
77. Qin, D.; Xia, Y.; Whitesides, G. M. *Nat. Protoc.* **2010**, *5*, 491-502.
78. Whitesides, G. M. *Nat. Biotechnol.* **2003**, *21*, 1161-1165.

79. Moench, W.; Zappe, H. *J. Opt. A Pure Appl. Opt.* **2004**, *6*, 330-337.
80. Yalcintas, E. P.; Ozutemiz, K. B.; Cetinkaya, T.; Dalloro, L.; Majidi, C.; Ozdoganlar, O. B. *Adv. Funct. Mater.* **2019**, *29*, 1906551.
81. Lange, S. A.; Benes, V.; Kern, D. P.; Horber, J. K.; Bernard, A. *Anal. Chem.* **2004**, *76*, 1641-1647.
82. Fredonnet, J.; Foncy, J.; Cau, J. C.; Severac, C.; Francois, J. M.; Trevisiol, E. *Microarrays* **2016**, *5*.
83. Hu, S.; Chen, T. H.; Zhao, Y.; Wang, Z.; Lam, R. H. W. *Langmuir* **2018**, *34*, 1750-1759.
84. Coyle, B. L.; Baneyx, F. *Chem. Commun.* **2016**, *52*, 7001-7004.
85. Hondrich, T. J. J.; Deussen, O.; Grannemann, C.; Brinkmann, D.; Offenhausser, A. *Micromachines* **2019**, *10*.
86. Kilian, K. A.; Bugarija, B.; Lahn, B. T.; Mrksich, M. *Proc. Natl. Acad. Sci. USA* **2010**, *107*, 4872-4877.
87. Khadpekar, A. J.; Khan, M.; Sose, A.; Majumder, A. *Sci. Rep.* **2019**, *9*, 1024.
88. Benor, A.; Tamang, A.; Wagner, V.; Salleo, A.; Knipp, D. *MRS Adv.* **2019**, *4*, 2441-2451.
89. Lee, S. H.; Rho, W. Y.; Park, S. J.; Kim, J.; Kwon, O. S.; Jun, B. H. *Sci. Rep.* **2018**, *8*, 16763.
90. Vonhoren, B.; Roling, O.; Buten, C.; Korsgen, M.; Arlinghaus, H. F.; Ravoo, B. J. *Langmuir* **2016**, *32*, 2277-2282.
91. Santhanam, V.; Andres, R. P. *Nano Lett.* **2004**, *4*, 41-44.

92. Zhuang, J.-L.; Zhang, Y.; Liu, X.-Y.; Wang, C.; Mao, H.-L.; Du, X.; Tang, J. *Appl. Surf. Sci.* **2019**, *469*, 90-97.
93. Hess, O.; Pendry, J. B.; Maier, S. A.; Oulton, R. F.; Hamm, J. M.; Tsakmakidis, K. L. *Nat. Mater.* **2012**, *11*, 573-584.
94. Green, M. A.; Pillai, S. *Nat. Photonics* **2012**, *6*, 130-132.
95. Anker, J. N.; Hall, W. P.; Lyandres, O.; Shah, N. C.; Zhao, J.; Van Duyne, R. P. *Nat. Mater.* **2008**, *7*, 442-453.
96. Ozbay, E. *Science* **2006**, *311*, 189-193.
97. Lauchner, A.; Schlather, A. E.; Manjavacas, A.; Cui, Y.; McClain, M. J.; Stec, G. J.; Garcia de Abajo, F. J.; Nordlander, P.; Halas, N. J. *Nano Lett.* **2015**, *15*, 6208-6214.
98. Wood, R. W. *Proc. Phys. Soc.* **1902**, *18*, 269-275.
99. Zhang, J.; Zhang, L.; Xu, W. *J. Phys. D Appl. Phys.* **2012**, *45*, 113001.
100. Zayats, A. V.; Smolyaninov, I. I.; Maradudin, A. A. *Phys. Rep.* **2005**, *408*, 131-314.
101. Barnes, W. L.; Dereux, A.; Ebbesen, T. W. *Nature* **2003**, *424*, 824-830.
102. Törmä, P.; Barnes, W. L. *Rep. Prog. Phys.* **2014**, *78*, 013901.
103. Wu, L.; Guo, J.; Xu, H.; Dai, X.; Xiang, Y. *Photonics Res.* **2016**, *4*, 262-266.
104. Heidel, T. D.; Mapel, J. K.; Singh, M.; Celebi, K.; Baldo, M. A. *Appl. Phys. Lett.* **2007**, *91*, 093506.
105. Willets, K. A.; Van Duyne, R. P. *Annu. Rev. Phys. Chem.* **2007**, *58*, 267-297.
106. Faraday, M. *Philos. T. R. Soc.* **1857**, *147*, 145-181.

107. Gerardo, A. L.; Estevez, M.-C.; Maria, S.; Laura, M. L. *Nanophotonics* **2017**, *6*, 123-136.
108. Haes, A. J.; Van Duyne, R. P. *Expert Rev. Mol. Diagn.* **2004**, *4*, 527-537.
109. Tu, M. H.; Sun, T.; Grattan, K. T. V. *Sensor. Actuat. B Chem.* **2014**, *191*, 37-44.
110. Zhan, C.; Chen, X.-J.; Yi, J.; Li, J.-F.; Wu, D.-Y.; Tian, Z.-Q. *Nat. Rev. Chem.* **2018**, *2*, 216-230.
111. Nitzan, A.; Brus, L. E. *J. Chem. Phys.* **1981**, *75*, 2205-2214.
112. Chen, C. J.; Osgood, R. M. *Phys. Rev. Lett.* **1983**, *50*, 1705-1708.
113. Huang, Y.-F.; Zhu, H.-P.; Liu, G.-K.; Wu, D.-Y.; Ren, B.; Tian, Z.-Q. *J. Am. Chem. Soc.* **2010**, *132*, 9244-9246.
114. Wu, D.-Y.; Liu, X.-M.; Huang, Y.-F.; Ren, B.; Xu, X.; Tian, Z.-Q. *J. Phys. Chem. C* **2009**, *113*, 18212-18222.
115. da Silva, A. G. M.; Rodrigues, T. S.; Correia, V. G.; Alves, T. V.; Alves, R. S.; Ando, R. A.; Ornellas, F. R.; Wang, J.; Andrade, L. H.; Camargo, P. H. C. *Angew. Chem. Int. Ed.* **2016**, *55*, 7111-7115.
116. Zhan, C.; Wang, Z. Y.; Zhang, X. G.; Chen, X. J.; Huang, Y. F.; Hu, S.; Li, J. F.; Wu, D. Y.; Moskovits, M.; Tian, Z. Q. *J. Am. Chem. Soc.* **2019**, *141*, 8053-8057.
117. Sarhan, R. M.; Koopman, W.; Schuetz, R.; Schmid, T.; Liebig, F.; Koetz, J.; Bargheer, M. *Sci. Rep.* **2019**, *9*, 3060.
118. Dong, B.; Fang, Y.; Chen, X.; Xu, H.; Sun, M. *Langmuir* **2011**, *27*, 10677-10682.
119. Zhan, C.; Chen, X.-J.; Huang, Y.-F.; Wu, D.-Y.; Tian, Z.-Q. *Acc. Chem. Res.* **2019**, *52*, 2784-2792.

120. Shin, H.-H.; Koo, J.-J.; Lee, K. S.; Kim, Z. H. *Appl. Mater. Today* **2019**, *16*, 112-119.
121. Hartland, G. V. *Chem. Rev.* **2011**, *111*, 3858-3887.
122. Link, S.; El-Sayed, M. A. *J. Phys. Chem. B* **1999**, *103*, 8410-8426.
123. Frischkorn, C.; Wolf, M. *Chem. Rev.* **2006**, *106*, 4207-4233.
124. Cho, G. C.; Dekorsy, T.; Bakker, H. J.; Hövel, R.; Kurz, H. *Phys. Rev. Lett.* **1996**, *77*, 4062-4065.
125. Manjavacas, A.; Liu, J. G.; Kulkarni, V.; Nordlander, P. *ACS Nano* **2014**, *8*, 7630-7638.
126. Khurgin, J. B. *Nat. Nanotechnol.* **2015**, *10*, 2-6.
127. James, L. B.; Christopher, L. W.; Dayeeta, S.; Emily, L. K.; Renee, R. F. *Nanophotonics* **2018**, *7*, 1697-1724.
128. Sönnichsen, C.; Franzl, T.; Wilk, T.; von Plessen, G.; Feldmann, J.; Wilson, O.; Mulvaney, P. *Phys. Rev. Lett.* **2002**, *88*, 077402.
129. Ahmadi, T. S.; Logunov, S. L.; El-Sayed, M. A. *J. Phys. Chem.* **1996**, *100*, 8053-8056.
130. Aruda, K. O.; Tagliazucchi, M.; Sweeney, C. M.; Hannah, D. C.; Schatz, G. C.; Weiss, E. A. *Proc. Natl. Acad. Sci. USA* **2013**, *110*, 4212-4217.
131. Mori, K.; Kawashima, M.; Che, M.; Yamashita, H. *Angew. Chem. Int. Ed.* **2010**, *49*, 8598-8601.
132. Gelle, A.; Jin, T.; de la Garza, L.; Price, G. D.; Besteiro, L. V.; Moores, A. *Chem. Rev.* **2020**, *120*, 986-1041.

133. Long, R.; Li, Y.; Song, L.; Xiong, Y. *Small* **2015**, *11*, 3873-3889.
134. Atwater, H. A.; Polman, A. *Nat. Mater.* **2010**, *9*, 205-213.
135. Liu, Z.; Hou, W.; Pavaskar, P.; Aykol, M.; Cronin, S. B. *Nano Lett.* **2011**, *11*, 1111-1116.
136. Bakhtiari, A. B.; Hsiao, D.; Jin, G.; Gates, B. D.; Branda, N. R. *Angew. Chem. Int. Ed.* **2009**, *48*, 4166-4169.
137. Lemieux, V.; Gauthier, S.; Branda, N. R. *Angew. Chem. Int. Ed.* **2006**, *45*, 6820-6824.
138. Fasciani, C.; Alejo, C. J. B.; Grenier, M.; Netto-Ferreira, J. C.; Scaiano, J. C. *Org. Lett.* **2011**, *13*, 204-207.
139. Dos Santos, C. G.; Marquez, D. T.; Crites, C.-O. L.; Netto-Ferreira, J. C.; Scaiano, J. C. *Tetrahedron Lett.* **2017**, *58*, 427-431.
140. Bauer, C.; Abid, J.-P.; Fermin, D.; Girault, H. H. *J. Phys. Chem.* **2004**, *120*, 9302-9315.
141. Douglas-Gallardo, O. A.; Berdakin, M.; Sánchez, C. G. *J. Phys. Chem. C* **2016**, *120*, 24389-24399.
142. Huh, H.; Trinh, H. D.; Lee, D.; Yoon, S. *ACS Appl. Mater. Interfaces* **2019**, *11*, 24715-24724.
143. Pasparakis, G. *Small* **2013**, *9*, 4130-4134.
144. Vankayala, R.; Sagadevan, A.; Vijayaraghavan, P.; Kuo, C.-L.; Hwang, K. C. *Angew. Chem. Int. Ed.* **2011**, *50*, 10640-10644.
145. Takeuchi, Y.; Fujita, T.; Takeyasu, N. *Phys. Chem. Chem. Phys.* **2019**, *21*, 7502-7507.

146. Tijunelyte, I.; Kherbouche, I.; Gam-Derouich, S.; Nguyen, M.; Lidgi-Guigui, N.; Lamy de la Chapelle, M.; Lamouri, A.; Levi, G.; Aubard, J.; Chevillot-Biraud, A.; Mangeney, C.; Felidj, N. *Nanoscale Horiz.* **2018**, *3*, 53-57.
147. Nguyen, V. Q.; Ai, Y.; Martin, P.; Lacroix, J. C. *ACS Omega* **2017**, *2*, 1947-1955.
148. Choi, H.-K.; Lee, K. S.; Shin, H.-H.; Kim, Z. H. *J. Phys. Chem. Lett.* **2016**, *7*, 4099-4104.
149. Choi, H.-K.; Park, W.-H.; Park, C.-G.; Shin, H.-H.; Lee, K. S.; Kim, Z. H. *J. Am. Chem. Soc. Lett.* **2016**, *138*, 4673-4684.
150. Etchegoin, P. G.; Le Ru, E. C. *Phys. Chem. Chem. Phys.* **2008**, *10*, 6069-6200.
151. Dent, G.; Smith, E. *Modern Raman Spectroscopy – A Practical Approach*, John Wiley & Sons Ltd.: Chichester, 2004, pp 1-21
152. Raman, C. V. *Indian J. Phys.* **1928**, *2*, 387-398.
153. Raman, C. V. *P. Natl. A. Sci. India A* **1953**, *37*, 342-349.
154. Mishchenko, E. G. *Phys. Rev. B* **1999**, *59*, 14892-14895.
155. Hendra, P. *Analyst* **2016**, *141*, 4996-4999.
156. Fleischmann, M.; Hendra, P. J.; McQuillan, A. J. *Chem. Phys. Lett.* **1974**, *26*, 163-166.
157. Albrecht, M. G.; Creighton, J. A. *J. Am. Chem. Soc.* **1977**, *99*, 5215-5217.
158. Jeanmaire, D. L.; Van Duyne, R. P., *J. Electroanal. Chem.* **1977**, *84*, 1-20.
159. Moskovits, M., *Rev. Mod. Phys.* **1985**, *57*, 783-826.

160. Maystre, D.; Lalanne, P.; Greffet, J.-J.; Aizpurua, J.; Hillenbrand, R.; McPhedran, R.; Quidant, R.; Bouhelier, A.; Colas des Francs, G.; Grandidier, J.; Lerondel, G.; Plain, J.; Kostcheev, S. *Plasmonics: From Basics to Advanced Topics*, Springer, 2012.
161. Mayer, K. M.; Hafner, J. H. *Chem. Rev.* **2011**, *111*, 3828-3857.
162. Le Ru, E. C.; Etchegoin, P. G. *Chem. Phys. Lett.* **2006**, *423*, 63-66.
163. Etchegoin, P. G.; Le Ru, E. C. *Phys. Chem. Chem. Phys.* **2008**, *10*, 6079-6089.
164. Le Ru, E. C.; Galloway, C.; Etchegoin, P. G. *Phys. Chem. Chem. Phys.* **2006**, *8*, 3083-3087.
165. Bantz, K. C.; Meyer, A. F.; Wittenberg, N. J.; Im, H.; Kurtuluş, Ö.; Lee, S. H.; Lindquist, N. C.; Oh, S.-H.; Haynes, C. L. *Phys. Chem. Chem. Phys.* **2011**, *13*, 11551-11567.
166. Lombardi, J. R.; Birke, R. L. *Acc. Chem. Res.* **2009**, *42*, 734-742.
167. Maitani, M. M.; Ohlberg, D. A. A.; Li, Z.; Allara, D. L.; Stewart, D. R.; Williams, R. S. *J. Am. Chem. Soc.* **2009**, *131*, 6310-6311.
168. Jensen, L.; Aikens, C. M.; Schatz, G. C. *Chem. Soc. Rev.* **2008**, *37*, 1061-1073.
169. Pilot, R.; Signorini, R.; Durante, C.; Orian, L.; Bhamidipati, M.; Fabris, L. *Biosensors* **2019**, *9*, 57.
170. Wang, H.; Graff, D. K.; Schoonover, J. R.; Palmer, R. A. *Appl. Spectrosc.* **1999**, *53*, 687-696.
171. Dann, S. E. *Reactions and characterization of solids*. The Royal Society of Chemistry: Cambridge, 2000.
172. Bain, C. D.; Whitesides, G. M. *Science* **1988**, *240*, 62.

173. Greenler, R. G. *J. Chem. Phys.* **1966**, *44*, 310-315.
174. Kestell, J. D.; Mudiyansele, K.; Ye, X.; Nam, C.-Y.; Stacchiola, D.; Sadowski, J.; Boscoboinik, J. A. *Rev. Sci. Instrum.* **2017**, *88*, 105109.
175. Finke, S. J.; Schrader, G. L. *Spectrochim. Acta A* **1990**, *46*, 91-96.
176. Buffeteau, T.; Desbat, B.; Blaudez, D.; Turlet, J. M. *Appl. Spectrosc.* **2000**, *54*, 1646-1650.
177. Ramin, M. A.; Le Bourdon, G.; Daugey, N.; Bennetau, B.; Vellutini, L.; Buffeteau, T. *Langmuir* **2011**, *27*, 6076-6084.

Chapter 3

3 PM-IRRAS Investigation of Photo-Enabled Surface Click Reactions at the Monolayer Level

Adapted with permission from *Langmuir*, **2020**, *36*, 1014-1022. This chapter investigates the utility of the SPAAC reaction in precisely tuning the surface properties of gold substrates at the monolayer level, and explores its applicability in the preparation of biorecognition interfaces on metallic surfaces. Polarization modulation infrared reflection-absorption spectroscopy (PM-IRRAS) has been used to detect and characterize monolayers adsorbed onto gold substrates, and to probe the progress of the surface SPAAC reactions.

3.1 Introduction

In recent years, growing interest in the modification of material surfaces has cultivated a demand for modification techniques that enable precise control over chemical functionality, polarity, hydrophobicity, reactivity, and other properties of surfaces. SAMs of thiolates on gold represent a convenient, bottom-up approach towards preparing chemically and structurally well-defined organic interfaces. The capacity of these SAMs to fine-tune surface properties has led to their emergence as key elements for biochemical research.

The structurally complex and dynamic nature of biological systems, such as proteins and cell membranes, can make detailed analysis of such samples difficult. In this respect, SAMs of thiols on gold have proven useful as model surfaces for the study of biochemical molecules, interactions, and processes. Thiol-containing molecules quickly and readily self-assemble on gold surfaces into consistently reproducible monolayers through the formation of the Au-S bond, a strong and highly stable bond generally considered to be covalent in nature.¹ In addition to their controllable ligand density, homogeneity, orientation, and surface properties,² and their ability to present specific organic molecules with a range of chemical functionalities, the high degree of order and tightly-packed surface density of alkane-thiol SAMs on gold reasonably mimic the

natural environment of the lipid bilayer structures of cell membranes.^{1,3} As a result, SAMs have been utilized in a variety of biochemical applications, including in biosensor development, as cell culture substrates, and as platforms to study biomolecular interactions.⁴⁻⁸

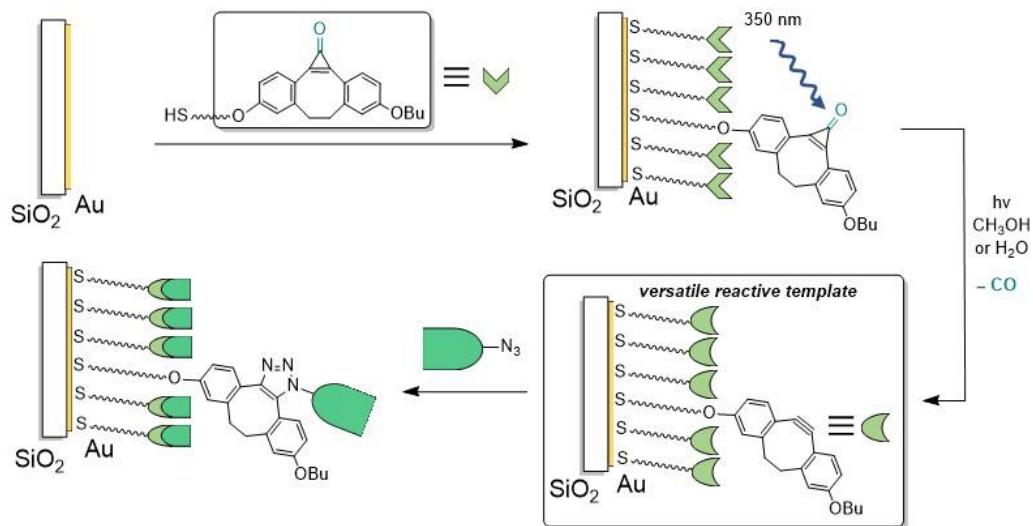
Substrates designed for studying biochemical events, such as protein interactions, biomolecule detection, or cell adhesion, often require the presentation of specific ligands or biochemical species at the substrate interface for effective target immobilization.⁴⁻⁸ The most obvious way to construct such interfaces using SAMs on gold is to prepare ligand molecules with thiol groups and incorporate them onto the gold surface directly by self-assembly. However, this method poses several difficulties; firstly, functionalizing the desired ligand molecules with thiol groups can be synthetically challenging, time-consuming, and expensive, as biomolecules are often large and complex. Secondly, if this molecule contains multiple thiol groups, as biomolecules often do, it can exhibit multiple binding modes at the surface with different structural conformations that may have a significant impact on biorecognition. An alternative approach to preparing surfaces functionalized for biological studies is to create SAMs of small molecules with reactive functional groups that are capable of covalently conjugating biomolecules to the substrate.

In this context, click chemistry, such as the CuAAC,⁹⁻¹⁰ can provide the means to SAM derivatization with biomolecules via the formation of stable triazole linkages. For example, Murphy and coworkers showed that an alkyne-bearing RGDSP peptide can be immobilized using the CuAAC on azide-terminated SAMs, which provided a modified platform for adhesion studies of human mesenchymal stem cells.¹¹⁻¹² Yeo and coworkers demonstrated on-demand electrochemical activation of the CuAAC on SAMs to afford a dynamic substrate to study cell migration.¹³ Lee and coworkers modified SAMs to display terminal maleimide groups using CuAAC, which was subsequently used for a thiol-Michael addition as a secondary click reaction to immobilize poly(L-lysine) as a model for polypeptide surfaces.¹⁴ More recently, Rubinstein and coworkers reported reactivity between azide-terminated SAMs and terminal alkyne-containing biological receptors via the CuAAC, and demonstrated LSPR biosensing on the modified

substrates.¹⁵ Although effective, these methods suffer from the cytotoxicity of Cu(I), which can have an effect on cell viability even in trace amounts if not properly removed.¹⁶⁻¹⁸ Furthermore, the introduction of alkynes into target molecules, although synthetically simpler than thiolation, can still be challenging and time-consuming. To circumvent these drawbacks, a complementary system is proposed that utilizes a strained cyclooctyne as the SAM terminal group, which can undergo SPAAC reactions with azido molecules to afford the triazole linkage.¹⁹ The advantages of using the SPAAC reaction with cyclooctyne-terminated SAMs as opposed to the CuAAC on azide-terminated SAMs are two-fold: first, the Cu(I) catalyst is no longer required, which makes this reaction suitable for use even with live samples; second, azido molecules are easily synthesized and widely commercially available – azide-bearing biomolecules in particular are readily commercially obtained. However, the strained alkyne is unstable in the presence of many nucleophilic groups.²⁰⁻²¹ One limitation of this click reaction with regard to its utility in surface functionalization is that thiolated strained alkynes cannot be easily incorporated onto metallic surfaces through the metal-thiol bond due to self-reactivity of the alkyne via thiol-yne addition.

Recently, the Workentin and Popik groups have developed a novel approach to functionalize AuNPs with thiol-terminated strained alkynes by masking the alkyne with a cyclopropanone moiety.²²⁻²³ Once incorporated onto the surface, the cyclopropanone is cleanly decarbonylated by irradiation with ultraviolet (UV) light to reveal the strained alkyne.²²⁻²³ This chemical system is adapted from Popik *et al.* who first utilized cyclopropanone-masked dibenzocyclooctynes (DIBOs) to label living cells,²⁴ and then to functionalize polymer brushes and immobilize azido molecules via SPAAC.²³ This method allowed for the synthesis of a thiolated alkyne precursor and its direct assembly onto AuNPs.²² Following decarbonylation, the DIBO-terminated SAM may be used as a versatile reactive template to immobilize any azide-containing molecules of choice. In this work, we have applied this strategy to SAMs on flat gold, enabling a similar approach to effectively introduce new functionalities, as depicted in Scheme 3.1. As the surface chemistry, preparation, and applications of SAMs on flat, solid-state Au substrates differ significantly from solution-dispersible colloidal Au, we sought to

investigate the feasibility of implementing this cyclopropenone-based strategy on this new material, as well as explore methods of validating the molecular reactivity.



Scheme 3.1: General strategy for incorporation of strained alkynes onto flat gold substrates and subsequent SPAAC reaction.

In addition to conferring surface functionality on SAMs, this photochemical deprotection strategy allows for spatial and temporal control over the unmasking of the alkyne, which grants the unique opportunity for photopatterning of the functionalized surface. Such surface modifications have the potential to alter a host of physical and chemical surface characteristics. Thus, these surface SPAAC reactions have a range of applications in the development of chemical sensors, biosensors, and other nanotechnologies that rely on the precise tunability of surface properties.^{23, 25} In this study, we attempt to investigate the use of a photomask to produce photopatterned, spatially resolved derivatization of the SAM with fluorescent dye molecules.

SAMs of thiolates on gold are amenable to a number of analytical techniques that enable our understanding of their surface chemistry, including X-ray photoelectron spectroscopy, FTIR spectroscopy, and surface plasmon resonance spectroscopy. One technique that is particularly interesting and ideally suited for the investigation of SAMs is PM-IRRAS, a well-established FTIR spectroscopic technique specifically developed to study monolayers of molecules adsorbed onto metallic surfaces.²⁶⁻²⁷ PM-IRRAS allows highly sensitive measurements of Au SAMs, yielding strong IR signals from a single

monolayer of molecules, while also providing information about the orientation of functional groups at the surface. Furthermore, PM-IRRAS measurements are made quantitative through use of a spectral calibration procedure.²⁶ The cyclopropenone-caged alkyne precursor possesses strong and distinct stretching vibrations in the mid-IR range, and the flat Au substrate is highly compatible with the PM-IRRAS technique. Hence, in this work, these SAMs were characterized by PM-IRRAS for the first time through collection of the vibrational fingerprints of key functional groups to provide important information on chemical composition and orientation of the SAM, and to monitor SPAAC reaction progress at each step of the chemical modifications to confirm successful reactivity. The high sensitivity and resolution of the PM-IRRAS technique also allowed assessment of the purity of monolayers at each step of the process to ensure that the SPAAC reactions proceeded cleanly, i.e. without producing unwanted side products or contaminants. PM-IRRAS spectra were accompanied with contact angle measurements of the SAMs to further validate successful surface modification.

In this work we have realized a facile and clean one-step protocol for the assembly of alkane-thiol SAMs with terminal cyclopropenone-masked DIBO groups on gold and their modification via photo-enabled SPAAC with azide reagents, as illustrated in Scheme 3.1. The unmasked strained alkyne SAMs were derivatized with a series of model azides with varied hydrophobicity to demonstrate the generality of this chemical system for the modification and fine-tuning of the surface chemistry, specifically hydrophobicity, on gold substrates. Photopatterning of the cyclopropenone SAMs with fluorescent dye molecules was also investigated. Furthermore, as a proof-of-concept study to show SAMs can be derivatized with larger biomolecules via SPAAC, we have prepared peptide-modified SAMs using this protocol and demonstrated their applicability for creating cell adhesion platforms and live imaging of human fibroblast cells. This derivatization method, as applied to flat Au, addresses a key deficiency in the field with respect to the use of cyclooctyne terminal groups in flat Au SAMs that will allow for faster and simpler preparation of functionalized and biofunctionalized SAMs.

3.2 Methods

3.2.1 PM-IRRAS Setup and Measurements

PM-IRRAS measurements were carried out using a Thermo Scientific Nicolet 6700 FTIR Spectrometer and a custom-built optical setup featuring a ZnSe photoelastic modulator (PEM-90 Model II, Hinds Instruments, Inc.) oscillating at 74 kHz. A wire grid polarizer was used to select the p-polarized light incident on the PEM. All spectra were recorded at a spectral resolution of 4 cm^{-1} and an angle of incidence of 80° with the PEM set for maximum modulation efficiency at 2000 cm^{-1} or 2500 cm^{-1} to cover the entire mid-IR range. 2000 scans were performed for each sample. The polarization-modulated beam was directed at a liquid nitrogen-cooled Thermo Scientific photovoltaic mercury-cadmium-telluride A (MCT-A) detector and then separated into high frequency “AC” and low frequency “DC” signals by a Stanford Research Systems Model SR650 Dual Channel Electronic Filter. AC and DC are the accepted designations for these signals because the high frequency signal oscillates at a much faster rate than the low frequency signal, similar to alternating and direct current electricity. For each measurement, AC signal is modulated twice: once by the PEM, and once by the Michelson interferometer. Thus, after electronic filtering, the AC signal was demodulated by a Stanford Research Systems Model SR830 DSP Lock-in Amplifier (LIA). Following simultaneous acquisition of the low frequency and demodulated high frequency signals through the two channels of the spectrometer and subsequent Fourier transform, the high frequency and low frequency signals were ratioed to give normalized differential reflectance spectra. Spectra were further calibrated using the procedure described by Buffeteau *et al.*^{26, 28} Calibration spectra were acquired by inserting a wire grid linear polarizer between the sample and the detector. Details regarding the PM-IRRAS spectral calibration procedure can be found in Appendix A. The resulting calibrated PM-IRRAS spectra show the vibrational absorptions of surface species with absorbance values smaller than $\Delta A=10^{-4}$. An illustration of the PM-IRRAS setup is shown in Figure 3.1.

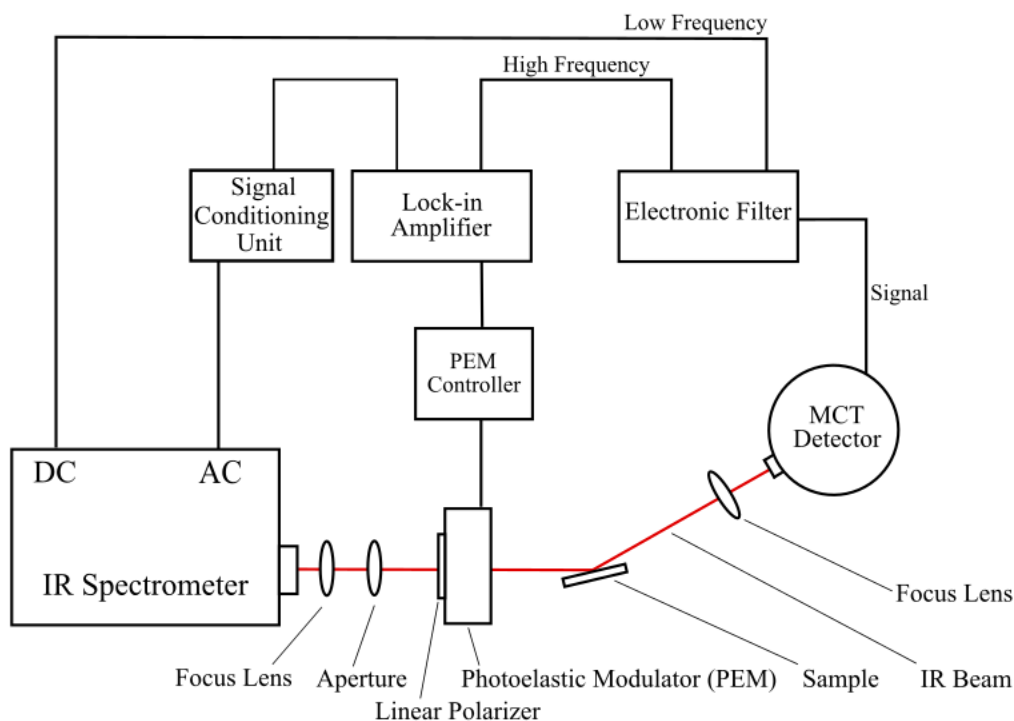


Figure 3.1: Schematic diagram of the PM-IRRAS optical setup and electronic processing.

3.2.2 Gold Substrate Fabrication

Gold mirror substrates were prepared via electrom beam evaporation of 150 nm of chromium followed by 100 nm of gold onto 3×1 -inch glass microscope slides. Prior to metal deposition, glass slides were cleaned with piranha solution (3:1 solution of concentrated $\text{H}_2\text{SO}_4/30\% \text{H}_2\text{O}_2$) and rinsed thoroughly with ultrapure water.

3.2.3 Synthesis of Organic Molecules

All reagents, unless otherwise stated, were purchased from Sigma-Aldrich and used as received. All common solvents, triethylamine (TEA), sodium sulfate anhydrous, and trifluoroacetic acid were purchased from Caledon. Azides A and B were synthesized according to a literature procedure.²⁹⁻³⁰ Azide C was synthesized according to a protocol previously developed in the Workentin group.³¹ Compound **1** was synthesized following a previously developed protocol.²²

FTIR spectra of model molecules were recorded using an attenuated total reflectance (ATR) attachment using a Bruker Vector 33 FTIR spectrometer. Characterization of each synthesized organic species by ^1H , $^{13}\text{C}\{^1\text{H}\}$, and $^{19}\text{F}\{^1\text{H}\}$ nuclear magnetic resonance (NMR) spectroscopy was carried out on Varian INOVA 400 (or 600) or Bruker AvIII HD 400 spectrometers using CDCl_3 or CD_3OD as solvent.

Cyclopropenone Thiol Precursor and Thiol

To a solution of **1** (1.19 g, 3.70 mmol) in dimethylformamide (DMF; 40 mL) was added compound **2** (3.37 g, 5.55 mmol). Next, portionwise was added K_2CO_3 (0.512 g, 3.70 mmol), then the solution was stirred and heated to 80 °C for 5 h (Scheme 3.2). The reaction was cooled to room temperature (r.t.), diluted with ethyl acetate (400 mL), washed 5 times with water (75 mL), brine (100 mL), and dried over MgSO_4 . The organic layer was then filtered, concentrated in vacuo, and purified via silica gel chromatography (hexanes: ethyl acetate 3:1 to CH_2Cl_2 : MeOH 30:1) to provide **3** (2.01 g, 72% yield) as a yellow oil. ^1H NMR (CDCl_3 , 400 MHz): δ 7.92 – 7.95 (m, 2H), 7.40 – 7.42 (m, 6H), 7.25 – 7.29 (m, 6H), 7.18 – 7.21 (m, 3H), 6.88 – 6.90 (m, 4H), 4.17 – 4.19 (t, $J = 4.7$ Hz, 2H), 4.03 – 4.06 (t, $J = 6.5$, 2H), 3.86 – 3.88 (t, $J = 4.7$ Hz, 2H), 3.71 – 3.73 (m, 2H), 3.64 – 3.65 (m, 2H), 3.57 – 3.60 (m, 2H), 3.45 – 3.347 (t, $J = 4.7$ Hz, 2H), 3.29 – 3.32 (m, 4H), 2.60 – 2.63 (d, $J = 10.7$ Hz, 2H), 2.41 – 2.44 (t, $J = 6.9$ Hz, 2H), 1.75 – 1.84 (m, 4H), 1.47 – 1.56 (m, 2H), 0.98 – 1.01 (t, $J = 7.4$ Hz, 3H). $^{13}\text{C}\{^1\text{H}\}$ NMR (CDCl_3 , 101 MHz): δ 162.8, 161.8, 154.0, 148.0, 148.0, 145.0, 142.6, 142.2, 136.0, 135.9, 129.8, 128.1, 126.9, 116.8, 116.6, 116.44, 116.39, 112.54, 112.45, 71.1, 70.9, 70.7, 70.4, 69.8, 69.7, 68.2, 67.9, 66.8, 37.38, 37.35, 31.9, 31.4, 19.4, 14.0. ESI-MS calculated for $\text{C}_{48}\text{H}_{51}\text{O}_6\text{S}$ [$\text{M} + \text{H}$] $^+$ 755.3401, found 755.3401.

Compound **3** (1.45 g, 1.92 mmol) was dissolved in CH_2Cl_2 (20 mL) and trifluoroacetic acid (TFA) (1.850 mL, 24.01 mmol). $^i\text{Pr}_3\text{SiH}$ (0.866 mL, 4.23 mmol) was added and the reaction mixture was stirred at r.t. under argon for 45 min (Scheme 3.2). The reaction was concentrated in vacuo and purified via silica gel chromatography (EtOAc:MeOH 95:5) to provide **4** (0.910 g, 92%) as a yellow oil. ^1H NMR (CDCl_3 , 400 MHz): δ 7.92 – 7.95 (d, $J = 8.7$ Hz, 2H), 6.88 – 6.92 (m, 4H), 4.20 – 4.23 (m, 2H), 4.03 – 4.06 (t, $J = 6.5$ Hz, 2H),

3.88 – 3.91 (m, 2H), 3.74 – 3.76 (m, 2H), 3.59 – 3.71 (m, 8H), 3.32 – 3.35 (d, $J = 10.6$, 2H), 2.61 – 2.64 (d, $J = 10.7$ Hz, 2H), 2.87 – 2.72 (m, 2H), 1.77 – 1.84 (m, 2H), 1.58 – 1.63 (t, $J = 7.4$ Hz, 1H), 1.47 – 1.56 (m, 2H), 0.98 – 1.01 (t, 3H). $^{13}\text{C}\{^1\text{H}\}$ NMR (CDCl_3 , 101 MHz): δ 162.3, 161.8, 154.0, 148.0, 142.6, 142.2, 136.0, 135.9, 116.8, 116.6, 116.43, 116.37, 112.6, 112.5, 73.1, 71.1, 70.9, 70.8, 70.4, 69.7, 68.2, 67.9, 37.39, 37.36, 31.3, 24.5, 19.4, 14.0. ESI-MS calculated for $\text{C}_{29}\text{H}_{37}\text{O}_6\text{S}$ $[\text{M} + \text{H}]^+$ 513.2305, found 513.2303.

Cyclopropenone Model 6

To a solution of compound **1** (0.190 g, 0.593 mmol) in CH_3CN (8 mL) was added 1-iodo-2-(2-(2-methoxyethoxy)ethoxy)ethane **5** (0.179 mg, 0.652 mmol) and K_2CO_3 at r.t. while stirring. The resulting suspension was heated to 55°C and left to stir for 16 h. After, the mixture was cooled to r.t. and CH_2Cl_2 (ca. 20 mL) was added (Scheme 3.2). Solids were removed by gravity filtration and the filtrate was concentrated by evaporation in vacuo. The residue was purified by column chromatography on silica gel using 7.5% CH_3OH in EtOAc as the eluent to afford compound **6** as a pale yellow oil (0.242 g, 87%). ^1H NMR (CDCl_3 , 600 MHz): δ 7.93 – 7.88 (m, 2H), 6.93 – 6.83 (m, 4H), 4.20 (t, $J = 5.3$ Hz, 2H), 4.02 (t, $J = 6.6$ Hz, 2H), 3.87 (t, $J = 4.8$ Hz, 2H), 3.75 – 3.71 (m, 2H), 3.69 – 3.66 (m, 2H), 3.66 – 3.63 (m, 2H), 3.56 – 3.52 (m, 2H), 3.36 (s, 3H), 3.35 – 3.25 (m, 2H), 2.65 – 2.54 (m, 2H), 1.82 – 1.74 (m, 2H), 1.53 – 1.46 (m, 2H), 0.98 (t, $J = 7.4$ Hz, 3H). $^{13}\text{C}\{^1\text{H}\}$ NMR (CDCl_3 , 151 MHz): δ 162.0, 161.5, 153.6, 147.67, 147.66, 142.4, 142.0, 135.7, 135.6, 116.5, 116.3, 116.1, 112.3, 112.2, 71.8, 70.8, 70.6, 70.5, 69.4, 67.9, 67.6, 59.0, 37.10, 37.07, 31.1, 19.1, 13.7. ESI-MS calculated for $\text{C}_{28}\text{H}_{34}\text{NaO}_6$ $[\text{M} + \text{Na}]^+$ 489.2253, found 489.2267.

Alkyne Model 7

A solution of compound **6** (0.088 g, 0.189 mmol) in CH_3OH (94 mL, $[\mathbf{2}] = 2.0$ mM) was irradiated in a Luzchem (LZC-4V) photoreactor equipped with 14 UV-A (350 nm) lamps for 20 min at r.t. (Scheme 3.2). The solution was concentrated in vacuo and purified by column chromatography on silica gel using EtOAc as the eluent to afford compound **7** as a pale yellow oil (0.078 g, 95%). ^1H NMR (CDCl_3 , 600 MHz): δ 7.20 (d, $J = 8.2$ Hz, 1H), 7.19 (d, $J = 8.5$ Hz, 1H), 6.90 (d, $J = 2.6$ Hz, 1H), 6.88 (d, $J = 2.6$ Hz, 1H), 6.78 (dd, $J =$

8.5 Hz, $J = 2.6$ Hz, 1H), 6.76 (dd, $J = 8.2$ Hz, $J = 2.6$ Hz, 1H), 4.16 – 4.12 (m, 2H), 3.98 (t, $J = 6.4$ Hz, 2H), 3.88 – 3.85 (m, 2H), 3.76 – 3.73 (m, 2H), 3.70 – 3.68 (m, 2H), 3.68 – 3.64 (m, 2H), 3.57 – 3.54 (m, 2H), 3.38 (s, 3H), 3.23 – 3.13 (m, 2H), 2.48 – 2.38 (m, 2H), 1.81 – 1.74 (m, 2H), 1.55 – 1.46 (m, 2H), 0.99 (t, $J = 7.6$ Hz, 3H). $^{13}\text{C}\{^1\text{H}\}$ NMR (CDCl_3 , 151 MHz): δ 158.6, 158.2, 154.8, 154.7, 126.6, 126.5, 116.8, 116.6, 116.4, 115.9, 111.9, 111.7, 110.5, 110.2, 71.9, 70.8, 70.6, 70.5, 69.6, 67.7, 67.5, 59.0, 36.58, 36.57, 31.2, 19.2, 13.8. EI-MS calculated for $\text{C}_{27}\text{H}_{34}\text{O}_5$ $[\text{M}]^+$ 438.2406, found 438.2408.

Click Model 8a/8b

To a solution of compound **7** (0.021 g, 0.048 mmol) in CH_2Cl_2 (2 mL) was added **azide A** (10.7 mg, 0.048 mmol) at r.t. while stirring. This mixture was left to stir for 16 h (Scheme 3.2). After, the solution was concentrated in vacuo and purified by column chromatography on silica gel using EtOAc as the eluent to afford compounds **8a** and **8b** as a mixture of regioisomers (0.030 g, 95%). ^1H NMR (CDCl_3 , 400 MHz): δ 7.46 – 7.37 (m, 1H), 7.17 – 7.08 (m, 1H), 6.95 – 6.65 (m, 4H), 5.74 – 5.62 (m, 1H), 5.47 – 5.35 (m, 1H), 4.22 – 4.04 (m, 2H), 4.04 – 3.78 (m, 4H), 3.78 – 3.59 (m, 6H), 3.59 – 3.48 (m, 2H), 3.43 – 3.25 (m, 4H), 3.12 – 2.95 (m, 2H), 2.90 – 2.77 (m, 1H), 1.83 – 1.68 (m, 2H), 1.56 – 1.40 (m, 2H), 1.03 – 0.92 (m, 3H). $^{13}\text{C}\{^1\text{H}\}$ NMR (CDCl_3 , 101 MHz): δ 160.2, 159.9, 158.8, 158.4, 146.3, 146.2, 143.4, 143.3, 139.2, 139.1, 134.0, 133.8, 132.8, 130.2, 122.4, 122.0, 118.0, 117.5, 116.5, 116.3, 116.1, 115.9, 112.8, 112.7, 112.4, 112.3, 108.9, 71.9, 70.81, 70.77, 70.64, 70.62, 70.55, 70.53, 69.64, 69.55, 67.73, 67.47, 67.24, 59.0, 39.6, 36.4, 36.3, 33.0, 31.3, 31.2, 29.7, 19.2, 13.79, 13.77. ESI-MS calculated for $\text{C}_{34}\text{H}_{36}\text{F}_5\text{N}_3\text{NaO}_5$ $[\text{M} + \text{Na}]^+$ 684.2473, found 684.2483.

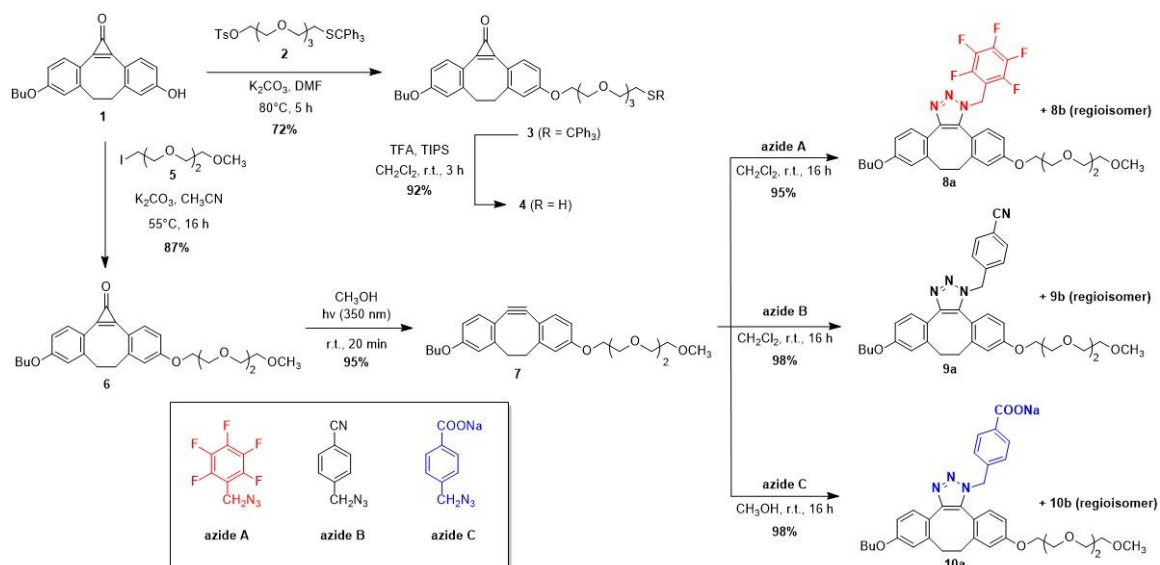
Click Model 9a/9b

To a solution of compound **7** (0.021 g, 0.048 mmol) in CH_2Cl_2 (2 mL) was added **azide B** (7.6 mg, 0.048 mmol) at r.t. while stirring. This mixture was left to stir for 16 h (Scheme 3.2). After, the solution was concentrated in vacuo and purified by column chromatography on silica gel using EtOAc as the eluent to afford compounds **9a** and **9b** as a mixture of regioisomers (0.028 g, 98%). ^1H NMR (CDCl_3 , 400 MHz): δ 7.63 – 7.55 (m, 2H), 7.50 – 7.43 (m, 1H), 7.27 – 7.16 (m, 2H), 6.99 – 6.90 (m, 1H), 6.87 – 6.64 (m,

4H), 5.60 (s, br, 2H), 4.18 – 4.03 (m, 2H), 4.01 – 3.79 (m, 4H), 3.78 – 3.61 (m, 6H), 3.59 – 3.50 (m, 2H), 3.42 – 3.35 (m, 3H), 3.35 – 3.20 (m, 1H), 3.08 – 2.92 (m, 1H), 2.87 – 2.61 (m, 2H), 1.83 – 1.67 (m, 2H), 1.56 – 1.42 (m, 2H), 1.03 – 0.92 (m, 3H). $^{13}\text{C}\{^1\text{H}\}$ NMR (CDCl_3 , 101 MHz): δ 160.2, 159.8, 158.8, 158.4, 147.0, 146.9, 143.2, 143.1, 140.69, 140.65, 138.9, 138.8, 133.7, 133.6, 132.9, 132.48, 132.47, 129.81, 129.79, 128.0, 122.3, 121.9, 118.2, 118.1, 117.6, 116.5, 116.4, 115.8, 115.6, 112.8, 112.7, 112.4, 112.3, 112.13, 112.12, 71.9, 70.79, 70.76, 70.62, 70.59, 70.53, 70.50, 69.6, 69.5, 67.7, 67.5, 67.4, 67.2, 58.99, 58.97, 51.48, 51.46, 36.55, 36.53, 32.81, 32.80, 31.23, 31.16, 29.6, 19.2, 13.8. EI-MS calculated for $\text{C}_{35}\text{H}_{40}\text{N}_4\text{O}_5$ $[\text{M}]^+$ 596.3000, found 596.3002.

Click Model 10a/10b

To a solution of compound **7** (0.026 g, 0.059 mmol) in CH_3OH (2 mL) was added **azide C** (11.8 mg, 0.059 mmol) at r.t. while stirring. This mixture was left to stir for 16 h (Scheme 3.2). After, the solution was concentrated in vacuo to afford compounds **10a** and **10b** as a mixture of regioisomers (0.028 g, 98%). ^1H NMR (CD_3OD , 600 MHz): δ 7.91 – 7.85 (m, 2H), 7.32 – 7.26 (m, 1H), 7.11 – 7.04 (m, 3H), 6.85 – 6.67 (m, 4H), 5.66 – 5.63 (m, 2H), 4.10 – 4.02 (m, 2H), 3.94 – 3.85 (m, 2H), 3.80 – 3.73 (m, 2H), 3.68 – 3.62 (m, 2H), 3.61 – 3.54 (m, 4H), 3.48 – 3.45 (m, 2H), 3.290 (s, 1.5H), 3.287 (s, 1.5H), 3.17 – 3.09 (m, 1H), 3.00 – 2.90 (m, 1H), 2.67 (t, $J = 7.0$ Hz, 2H), 1.73 – 1.64 (m, 2H), 1.49 – 1.40 (m, 2H), 0.95 (t, $J = 7.3$ Hz, 1.5H), 0.93 (t, $J = 7.3$ Hz, 1.5H). $^{13}\text{C}\{^1\text{H}\}$ NMR (CD_3OD , 151 MHz): δ 169.5, 162.0, 161.6, 160.7, 160.4, 148.2, 148.0, 144.6, 144.5, 142.0, 141.3, 141.2, 136.0, 135.8, 133.54, 133.50, 132.2, 131.6, 131.2, 128.6, 123.5, 123.1, 119.3, 118.9, 117.6, 117.5, 117.0, 116.9, 114.3, 114.1, 113.9, 113.8, 73.1, 71.85, 71.84, 71.68, 71.67, 71.5, 70.91, 70.85, 68.9, 68.8, 68.6, 59.2, 53.1, 37.3, 37.2, 34.1, 32.6, 32.5, 20.4, 14.3.



Scheme 3.2: Synthesis of thiol 4 and model molecules.

3.2.4 SAM Assembly

Prepared gold mirror substrates were cut into approximately 1 × 2 cm pieces and then cleaned by immersion in a 3% (weight/volume) solution of Nochromix (Godax Laboratories, Inc.) in concentrated H₂SO₄ at 80 °C for 30 min. Cleaned substrates were rinsed thoroughly with ultrapure water followed by absolute ethanol and then dried under a stream of N₂ gas. Substrates were then immersed in a deoxygenated methanolic solution of thiol **4** (2 mM) for 16 h at room temperature. Afterward, substrates were removed from the thiol solution, washed generously with methanol and dried on the benchtop.

3.2.5 Photo-Click Modification of SAMs

Cyclopropenone SAMs on gold substrates were immersed in a 2 mM deoxygenated solution of azide in CH₃OH (azide A or C), CH₃OH/H₂O (azide B), or H₂O (RGD peptide) followed by irradiation in a Luzchem LZC-4V photoreactor equipped with 14 UVA (350 nm) 8 W lamps for 12 min at room temperature. Afterward, substrates were left to react for 12 h. Modified SAMs were washed with H₂O and CH₃OH then left to dry on the benchtop.

3.2.6 Photopatterning of SAMs

Cyclopropanone SAMs on Au substrates were irradiated in a H₂O:methanol solution of azide-PEG3-biotin (CAS 875770-34-6 from Millipore Sigma) with a 400 mesh copper grid (FCF400-Cu from Electron Microscopy Sciences) placed gently on the surface as a photomask. Following irradiation, SAMs were immersed in a solution of streptavidin Alexa Fluor 488 dye conjugate in PBS for 20 min to allow biotin-streptavidin complexation, then washed with PBS. Fluorescence microscopy of the photopatterned substrates was performed using a Nikon ECLIPSE ITi2 Inverted Research Microscope.

3.2.7 Contact Angle Measurements

Contact angles were measured with deionized water using a Kruss Drop Shape Analysis (DSA) 100 goniometer with DSA software, at room temperature (22°C). All the static water contact angles were determined by averaging values measured for 10 μ L droplets at three different spots on each substrate. The Laplace-Young fitting method was used to calculate all the static contact angles.

3.2.8 Cell Adhesion Studies

Primary fibroblasts were derived from surgically resected palmar fascia tissues of Dupuytren's disease patients. Fibroblast cultures were incubated in Dulbecco's Modified Eagle Medium (D-MEM) supplemented with 10% fetal bovine serum albumin (Invitrogen), 1% L-glutamine and antibiotic-antimycotic solution (Sigma-Aldrich). Cell cultures were serially passaged at confluency up to 6 passages for analysis; otherwise, cells were discarded. Primary fibroblast cells were plated (about 250,000 cells) onto SAMs on gold modified with Cyclo[Arg-Gly-Asp-D-Phe-Lys(Azide)] (RGDFK) peptide (Peptides International; RGD-3749-PI) overnight. After gentle washing with phosphate-buffered saline (PBS) to remove loosely bound cells, substrates were immersed in 2 mM Calcein AM (Abcam; ab141420) solution in PBS. After 30 min, cells were imaged live using a Nikon ECLIPSE ITi2 Inverted Research Microscope set to the FITC channel ($\lambda_{\text{ex}} = 488 \text{ nm}$) to monitor esterase activity.

3.3 Results and Discussion

3.3.1 Cyclopropenone SAM Assembly and Characterization

SAMs of cyclopropenone thiols were prepared via immersion of clean gold substrates into 2 mM solutions of thiol **4** in methanol at room temperature overnight, as illustrated in Figure 3.2a. Model compound **6** (Scheme 3) was synthesized to allow comparison of the cyclopropenone SAM to corresponding FTIR spectroscopic data. PM-IRRAS measurements of the functionalized gold surface, shown in Figure 3.2b, displayed the characteristic absorption at 1841 cm^{-1} of the cyclopropenone C=O stretch.^{22, 32} Furthermore, comparison of the PM-IRRAS data with an FTIR spectrum of cyclopropenone model **6** revealed that the same peaks were present in the fingerprint regions of both the model and the SAM, confirming proper SAM assembly. An overlay of PM-IRRAS and FTIR spectra is shown in Figure 3.2b. Detailed assignments of the IR peaks are presented in Table 3.1.

These findings were validated by contact angle measurements taken using water on the gold substrate surface before and after functionalization. The greater the spreading of the droplet on the surface, the larger the contact angle that is made at the interface. The spreading of water at the surface of a given sample is directly related to the wettability of the surface, thus contact angle measurements are direct indicators of surface wettability and hydrophilicity. Significant change in the contact angle from 63° to 74° , as seen in Figure 3.2a, was observed upon SAM formation, indicating successful functionalization as organic SAMs are expected to increase surface hydrophobicity.

While the peak positions of model **6** and the cyclopropenone SAM align well, there are significant differences in the relative intensities of some peaks. For example, the signal at 1841 cm^{-1} , corresponding to the cyclopropenone C=O stretch, appears less intense in the spectrum of the SAM than in the spectrum of the model molecule relative to other prominent peaks in each spectrum. This is likely due to the surface selection rule of PM-IRRAS, which states that only vibrational modes with a component of the transition dipole moment aligned perpendicular to the substrate surface can contribute to the absorbance spectrum.³³ As a result, PM-IRRAS is sensitive to the orientation of bonds in

a monolayer. The direct consequence of this is that lower absorbances will be observed for vibrational modes that are parallel to the surface. Thus, disparities in relative peak intensities between the SAM and the model, such as that observed for the cyclopropanone C=O stretch at 1841 cm^{-1} , may indicate that, within the SAM, this functional group is oriented parallel or near parallel to the substrate surface.

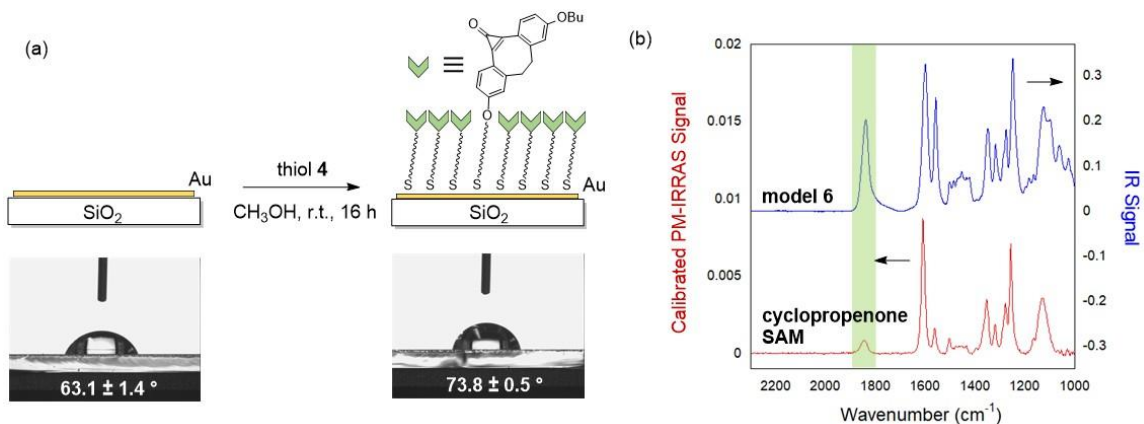


Figure 3.2: (a) Assembly of cyclopropanone SAMs. Water contact angles were measured in triplicate and reported as an average. (b) Overlaid PM-IRRAS spectrum of cyclopropanone SAM and FTIR spectrum of model compound 6; blue spectrum designates FTIR spectrum of model molecule; red spectrum designates PM-IRRAS spectrum of SAM. Arrow indicates respective scale.

Table 3.1: List of important vibrational modes and mode assignments for the PM-IRRAS spectrum of a SAM of cyclopropanone thiol 4 on gold.

Frequency (cm^{-1})	Assignment
1844	C=O stretch of cyclopropanone
1610	C=C stretch of cyclopropanone
1562	Aromatic ring vibrations
1504	Aromatic ring vibrations
1354	Alkyl C-H bend
1321	Alkyl ether
1278	C-O-C stretch of alkyl aryl ether (PEG chain)
1257	C-O-C stretch of alkyl aryl ether (tert-butyl aryl ether)

3.3.2 Tuning Surface Hydrophobicity by SAM Modification

Following successful cyclopropanone SAM formation, we sought to investigate our ability to specifically control the surface properties of gold substrates by chemically modifying these SAMs via photo-enabled interfacial SPAAC reactions. Gold mirror substrates were functionalized with SAMs of **4**, immersed in a solution of the target azide, then irradiated with UV light to deprotect the cyclooctyne *in situ*, with complete decarbonylation achieved within a few hundred picoseconds.³⁴⁻³⁵ The uncaged strained alkyne is then able to react with azides in solution to form the triazole linkage. In the absence of UV irradiation, SAMs of **4** do not react with azides at the surface as the cyclopropanone-masked DIBO moiety is very stable at room temperature and under ambient light conditions.²³⁻²⁴ Azides A-C (Scheme 3) were selected as model reagents for SAM modification, as they serve as a gradient of increasing hydrophilicity that may be monitored through contact angle measurements in conjunction with PM-IRRAS characterization (Figure 3.3). Additionally, azides B and C contain functional groups C≡N and C=O, respectively, that feature prominent characteristic IR stretches (C≡N at 2220 cm⁻¹ and C=O at 1720 cm⁻¹) that can be probed with PM-IRRAS. Separately, model cyclopropanone **6** was irradiated to afford alkyne model **7**, which was then reacted to azides A-C to yield model molecules **8a/8b**, **9a/9b**, and **10a/10b** (Scheme 3) for comparison of PM-IRRAS spectra of SAMs to FTIR data of the models.

PM-IRRAS analysis of the three modified SAMs on gold showed in each case complete disappearance of the cyclopropanone C=O peak at 1841 cm⁻¹ as well as the presence of characteristic IR signals associated with the key functional groups within each of the corresponding azides, as evidenced in Figure 3.3. PM-IRRAS spectra of SAMs “clicked” with azide A contained IR signals consistent with a polyfluorinated ring.³⁶ PM-IRRAS spectra of SAMs comprising azide B featured the nitrile C≡N stretch at 2220 cm⁻¹, and those modified with azide C showed the characteristic C=O stretch at 1720 cm⁻¹. Furthermore, in spectra of all three modified SAMs there is no trace of any peaks in the 2120 cm⁻¹ region. This is significant, as a signal in or near this position would correspond to an azide N=N=N stretch. The absence of such a peak indicates that the observed signals that appear to correspond to azides A-C are in fact due to the product of the

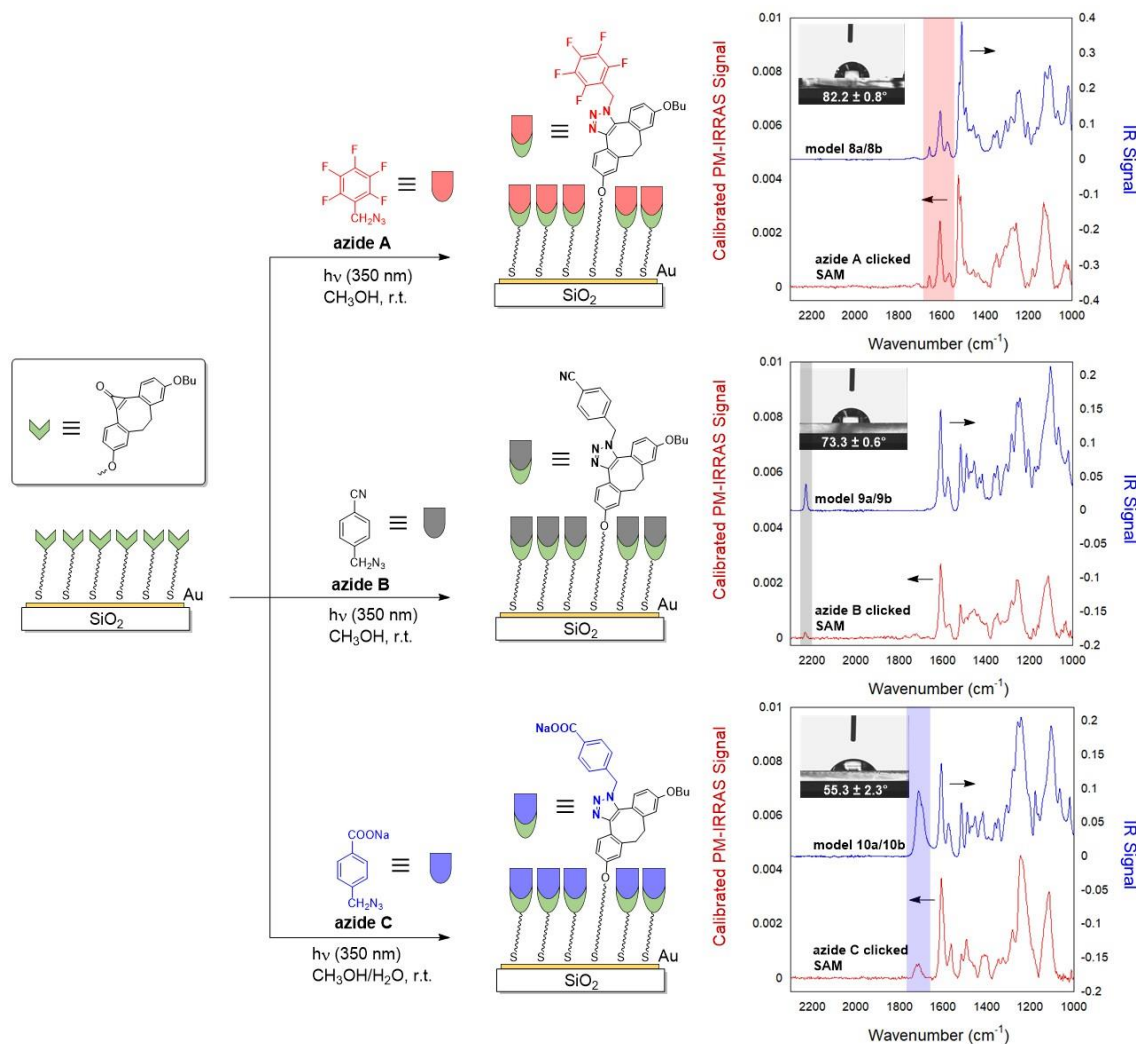


Figure 3.3: Modification of SAMs via photo-enabled click chemistry with azides A-C. Water contact angles were measured in triplicate and reported as an average. Blue spectra designate FTIR spectra of model molecules; red spectra designate PM-IRRAS spectra of SAMs. Arrow indicates respective scale.

surface SPAAC click reaction, and are not due to excess unreacted azides trapped in the SAM or resting on the surface of the gold substrate. Lastly, comparison of PM-IRRAS spectra of the SAMs with FTIR spectra of the model compounds **8a/8b**, **9a/9b**, and **10a/10b** for azides A-C, respectively, was used to verify successful SAM modification. Overlays of each pair of FTIR and PM-IRRAS data, shown in Figure 3.3, display nearly identical peaks in the fingerprint regions of each set of spectra. This direct comparison

not only confirms successful SAM reactivity but also indicates that this surface SPAAC reaction is likely a clean process that does not generate undesirable side products.

PM-IRRAS characterization of each SAM was accompanied by contact angle measurements of the chemically modified surfaces in order to illustrate how our unique chemical system can be used to selectively tune surface properties such as hydrophilicity simply through choice of azide. As expected, incorporation of the chosen target azides onto the functionalized gold surfaces induced changes in the surface hydrophilicity in an increasing manner from azides A to C. SAMs modified with azide A were found to have the highest contact angle at 82° , SAMs reacted with azide B had on average a contact angle of 73° , and SAMs containing azide C possessed the lowest contact angle, 55° . This observed surface tension gradient showing increasing hydrophilicity from azide A to C demonstrates the ability of this photo-enabled interfacial SPAAC reaction to dictate the properties of metallic surfaces through easily achieved chemical modification.

3.3.3 Photopatterning of Cyclopropenone SAMs

After confirming that Au SAM modifications could be readily achieved via photo-enabled SPAAC, we investigated the use of a photomask to afford spatially resolved derivatization of the SAM. In this photopatterning experiment, a cyclopropenone SAM substrate was irradiated in a solution of azide-PEG3-biotin with a 400 mesh copper grid placed gently on the surface as a photomask, illustrated in Figure 3.4. The resulting partially derivatized SAM was then exposed to a solution of streptavidin Alexa Fluor 488 dye conjugate in PBS to allow for biotin-streptavidin complexation, followed by washing with PBS. Fluorescence microscopy of the photopatterned SAM revealed the copper grid pattern (Figure 3.4); however, poor contrast was observed. We believe this may have been due to the inherent difficulties associated with taking fluorescence measurements on an opaque and highly reflective surface, or potentially due to quenching of the fluorescence as a result of proximity to the gold surface.³⁷ It is also possible that the pattern was simply transferred poorly due to limitations of the experiment.

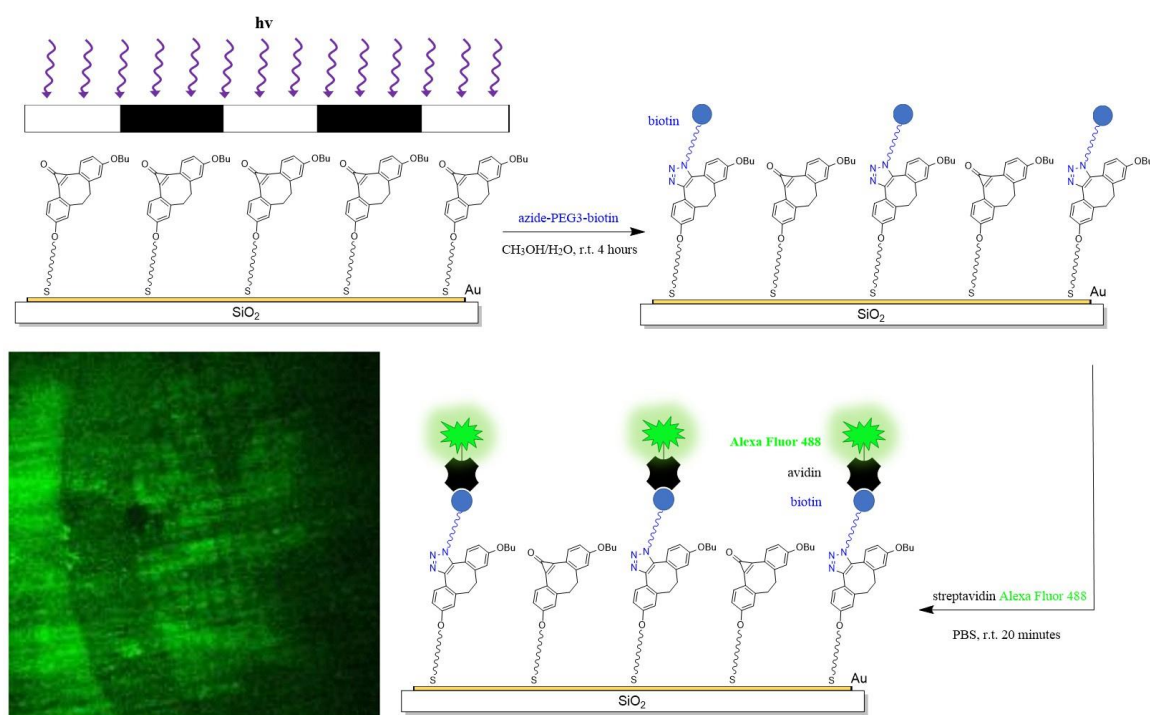


Figure 3.4: Photopatterning of SAMs on gold using biotin-N₃ and streptavidin Alexa Fluor 488.

3.3.4 Cell Adhesion Studies on Modified SAMs

Once it was established that the photo-enabled SPAAC was a viable means for surface modification of SAMs on gold, the compatibility of this approach with biochemical applications was investigated. One gold substrate functionalized with a SAM of cyclopropanone thiol **4** was irradiated and clicked with an azide-modified RGDFK peptide (Figure 3.5a/b), a common cyclic cell adhesion peptide found in the extracellular matrix that is known to bind the $\alpha_v\beta_3$ integrin cell membrane receptors that populate the surfaces of many different cell types.^{11-12, 38} Separately, another gold substrate functionalized with **4** was left in the dark and immersed in a solution of the same peptide to act as a negative control sample (Figure 3.5c/d); the cyclopropanone would not be decarbonylated and thus no subsequent SPAAC reaction could occur. After thoroughly rinsing each substrate to remove unreacted RGDFK-N₃ peptide, both SAMs were incubated in cultures of live human fibroblast cells (approximately 250,000 cells)

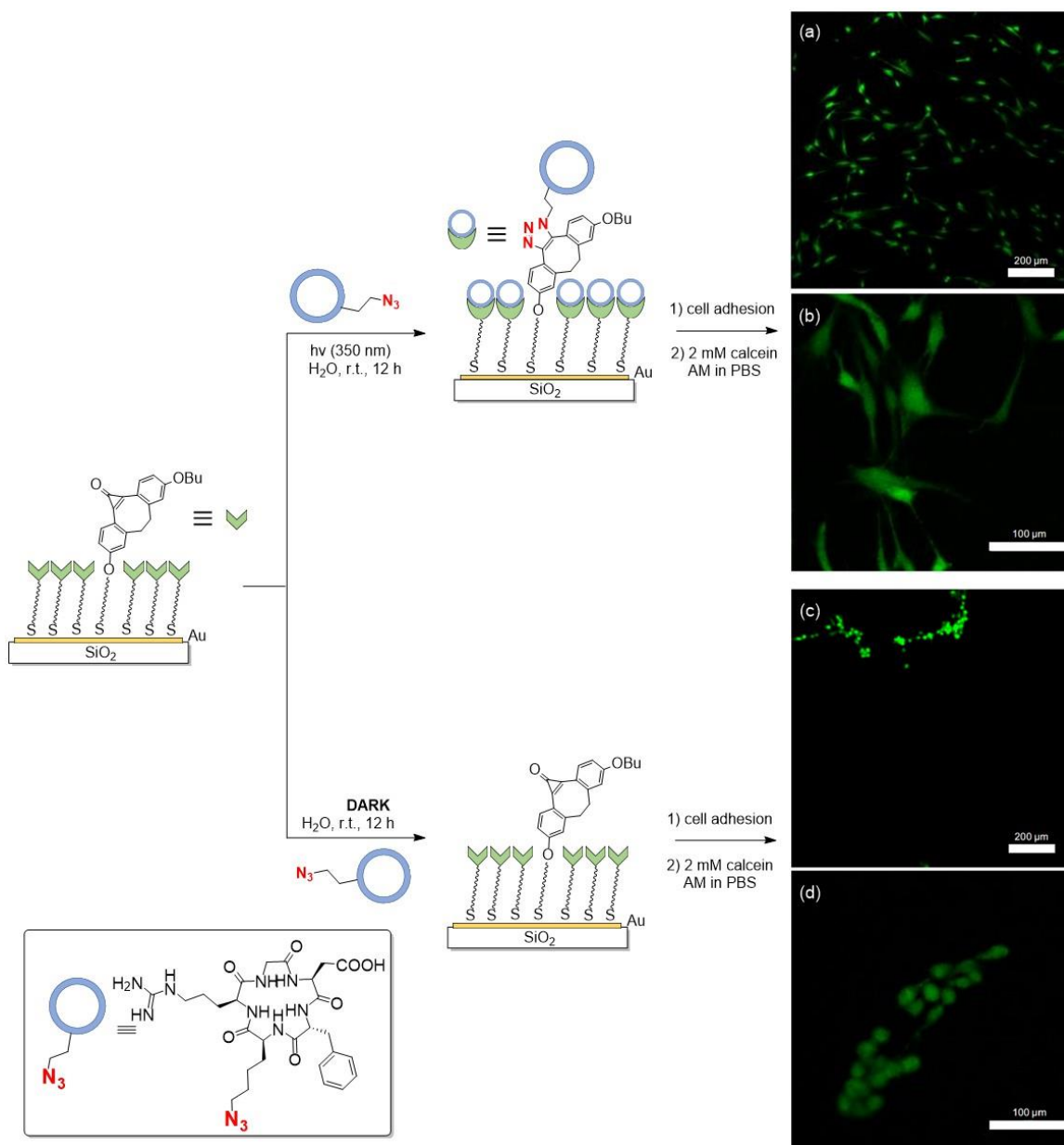


Figure 3.5: Cell adhesion studies using cyclopropanone SAMs; (a) fluorescence microscopy image of the substrate irradiated and derivatized with cyclic RGDFK peptide at a lower magnification and (b) at a higher magnification; (c) fluorescence microscopy image of the substrate not irradiated in the presence of cyclic RGDFK peptide at a lower magnification and (d) at a higher magnification.

overnight to promote adhesion. After incubation, loosely bound cells were gently washed away with PBS solution and the rinsed SAMs were immersed in a solution of calcein AM, which is taken up by cells and metabolized by intracellular esterases into the

fluorescent dye calcein. This allowed for imaging of the adhered cells by fluorescence microscopy and also served as a means to test for cell viability. We hypothesized that this would present fewer challenges related to quenching of the fluorescent dye, as the cells extend microns above the gold surface.

Although fluorescence microscopy of each substrate revealed living cells present on both the peptide-derivatized and negative control SAMs, there were two key differences between the samples. First, the adhesion density of human fibroblast cells on the RGDFK-bearing SAM was higher and much more equally distributed across the substrate surface (Figure 3.5a/b), whereas there were fewer adhered cells on the control substrate, and cells were tightly packed into confined areas (Figure 3.5c/d). We attribute this effect to defect sites in the control SAM. Second and most notable, the spindle-shaped and elongated morphology exhibited by typical human fibroblast cells in their native environment was retained on the peptide-modified SAM (Figure 3.5a/b). Conversely, cells adhered on the negative control SAM adopted a spherical and clustered formation, which may indicate less favorable, non-specific interactions between the cell membranes and the SAM of molecule **4** (Figure 3.5c/d). These crucial differences highlight the need for peptide modification facilitated by the photo-enabled click chemistry methodology presented here in order to properly study live human fibroblast cells in their native morphology on metallic substrates.

3.4 Conclusions

In this research we have developed an improved methodology for controlling and modifying the surface properties of flat metallic substrates through photo-enabled interfacial SPAAC reactions. The challenges associated with incorporating thiolated strained alkynes onto metal surfaces have been overcome by utilizing a photochemical alkyne precursor, an approach that has not been previously realized. PM-IRRAS was used to characterize SAMs of cyclopropanone-masked cyclooctynes, as well as to probe the progress of several SPAAC reactions with SAMs designed to specifically tune the substrate surface properties at the monolayer level. Furthermore, we demonstrated the suitability of this process for biochemical applications such as cell adhesion studies. By employing a system of alkyne-terminated SAMs and azide reagents – unlike the more

common azide SAMs and alkyne reagents – we have been able to both eliminate the presence of cytotoxic Cu(I) catalysts as well as increase the versatility and utility of the SPAAC reaction, as azide reagents are far more commercially available and easier to synthesize. The ease-of-synthesis and rapid commercialization of azide reagents ranging from small molecules to large biomolecules, like the azide-RGDFK peptide in this work, reinforces the applicability and generality of this strategy such that SAM modifications are readily achieved with target molecules designed for many different applications.

3.5 References

1. Love, J. C.; Estroff, L. A.; Kriebel, J. K.; Nuzzo, R. G.; Whitesides, G. M. *Chem. Rev.* **2005**, *105*, 1103-69.
2. Yeung, S. Y.; Ederth, T.; Pan, G.; Cicenaitis, J.; Cardenas, M.; Arnebrant, T.; Sellergren, B. *Langmuir* **2018**, *34*, 4107-4115.
3. Vijayamohanan, K.; Aslam, M. *Appl. Biochem. Biotechnol.* **2001**, *96*, 25-39.
4. Arya, S. K.; Solanki, P. R.; Datta, M.; Malhotra, B. D. *Biosens. Bioelectron.* **2009**, *24*, 2810-7.
5. Choi, S.; Murphy, W. L. *Langmuir* **2008**, *24*, 6873-80.
6. Islam, N.; Gurgel, P. V.; Rojas, O. J.; Carbonell, R. G. *J. Phys. Chem. C* **2014**, *118*, 5361-5373.
7. Patel, N.; Davies, M. C.; Hartshorne, M.; Heaton, R. J.; Roberts, C. J.; Tendler, S. J. B.; Williams, P. M. *Langmuir* **1997**, *13*, 6485-6490.
8. Samanta, D.; Sarkar, A. *Chem. Soc. Rev.* **2011**, *40*, 2567-92.
9. Rostovtsev, V. V.; Green, L. G.; Fokin, V. V.; Sharpless, K. B. *Angew. Chem. Int. Ed.* **2002**, *41*, 2596-9.
10. Tornøe, C. W.; Christensen, C.; Meldal, M. *J. Org. Chem.* **2002**, *67*, 3057-64.

11. Hudalla, G. A.; Murphy, W. L. *Langmuir* **2009**, *25*, 5737-46.
12. Hudalla, G. A.; Murphy, W. L. *Langmuir* **2010**, *26*, 6449-56.
13. Choi, I.; Kim, Y. K.; Min, D. H.; Lee, S.; Yeo, W. S. *J. Am. Chem. Soc.* **2011**, *133*, 16718-21.
14. Shakiba, A.; Jamison, A. C.; Lee, T. R. *Langmuir* **2015**, *31*, 6154-63.
15. Yaakov, N.; Chaikin, Y.; Wexselblatt, E.; Tor, Y.; Vaskevich, A.; Rubinstein, I. *Chem. Eur. J.* **2017**, *23*, 10148-10155.
16. Lallana, E.; Riguera, R.; Fernandez-Megia, E. *Angew. Chem. Int. Ed.* **2011**, *50*, 8794-804.
17. Li, S.; Cai, H.; He, J.; Chen, H.; Lam, S.; Cai, T.; Zhu, Z.; Bark, S. J.; Cai, C. *Bioconjugate Chem.* **2016**, *27*, 2315-2322.
18. Li, S.; Wang, L.; Yu, F.; Zhu, Z.; Shobaki, D.; Chen, H.; Wang, M.; Wang, J.; Qin, G.; Erasquin, U. J.; Ren, L.; Wang, Y.; Cai, C. *Chem. Sci.* **2017**, *8*, 2107-2114.
19. Agard, N. J.; Prescher, J. A.; Bertozzi, C. R. *J. Am. Chem. Soc.* **2004**, *126*, 15046-7.
20. Golkowski, M.; Ziegler, T. *Synthesis* **2013**, *45*, 1207-1214.
21. van Geel, R.; Pruijn, G. J. M.; van Delft, F. L.; Boelens, W. C. *Bioconjugate Chem.* **2012**, *23*, 392-398.
22. Luo, W.; Gobbo, P.; McNitt, C. D.; Sutton, D. A.; Popik, V. V.; Workentin, M. S. *Chem. Eur. J.* **2017**, *23*, 1052-1059.
23. Orski, S. V.; Poloukhine, A. A.; Arumugam, S.; Mao, L.; Popik, V. V.; Locklin, J. J. *Am. Chem. Soc.* **2010**, *132*, 11024-6.

24. Poloukhine, A. A.; Mbua, N. E.; Wolfert, M. A.; Boons, G. J.; Popik, V. V. *J. Am. Chem. Soc.* **2009**, *131*, 15769-76.
25. Ulman, A. *Chem. Rev.* **1996**, *96*, 1533-1554.
26. Buffeteau, T.; Desbat, B.; Blaudez, D.; Turlet, J. M. *Appl. Spectrosc.* **2000**, *54*, 1646-1650.
27. Rajalingam, K.; Hallmann, L.; Strunskus, T.; Bashir, A.; Woll, C.; Tuczek, F. *Phys. Chem. Chem. Phys.* **2010**, *12*, 4390-9.
28. Ramin, M. A.; Le Bourdon, G.; Daugey, N.; Bennetau, B.; Vellutini, L.; Buffeteau, T. *Langmuir* **2011**, *27*, 6076-84.
29. Demko, Z. P.; Sharpless, K. B. *Angew. Chem. Int. Ed.* **2002**, *41*, 2110-3.
30. Liu, M.; Reiser, O. *Org. Lett.* **2011**, *13*, 1102-5.
31. Luo, W.; Gobbo, P.; Gunawardene, P. N.; Workentin, M. S. *Langmuir* **2017**, *33*, 1908-1913.
32. Luo, W.; Luo, J.; Popik, V. V.; Workentin, M. S. *Bioconjugate Chem.* **2019**, *30*, 1140-1149.
33. Greenler, R. G. *J. Chem. Phys.* **1966**, *44*, 310-315.
34. Poloukhine, A.; Popik, V. V. *J. Phys. Chem. A* **2006**, *110*, 1749-57.
35. Takeuchi, S.; Tahara, T. *J. Chem. Phys.* **2004**, *120*, 4768-76.
36. Brown, P. J. N.; Mooney, E. F. *Spectrochim. Acta A* **1968**, *24*, 1317-1320.
37. Ishida, A.; Majima, T. *Analyst* **2000**, *125*, 535-540.
38. Guzzetti, I.; Civera, M.; Vasile, F.; Arosio, D.; Tringali, C.; Piarulli, U.; Gennari, C.; Pignataro, L.; Belvisi, L.; Potenza, D. *ChemistryOpen* **2017**, *6*, 128-136.

Chapter 4

4 Plasmon-Mediated Grafting of Diazonium Salts on AuNP-Patterned Surfaces

Chemical reactions can be catalyzed on the surfaces of metallic nanostructures by transfer of hot charge carriers generated through excitation of localized surface plasmon resonance. This chapter first explores the design and fabrication of substrates patterned with metallic nanostructures using soft lithography techniques, and then validates their utility as plasmonically active platforms suitable for SERS and for plasmon-mediated catalysis. Finally, aryl thin films are chemically grafted onto the patterned substrates via the plasmon-mediated reduction of aryl diazonium salts.

4.1 Introduction

Molecular plasmonics utilizes metallic nanostructures to confine light to subwavelength regions, enabling the ability to manipulate interactions between light and molecules located at the surface of nanoscale metallic structures.¹ Metallic nanoparticles exhibit collective oscillations of free electrons in the conduction band, called plasmons, which can be excited by light of a wavelength that corresponds to the frequency of oscillation.² Plasmon excitation on the surface of a metallic nanostructure generates localized surface plasmon resonance (LSPR), described as the confinement of an external electric field to nanoscale areas on a nanostructure surface resulting in hotspots of intense near-field enhancement. Surface-enhanced Raman spectroscopy (SERS) and other plasmon-enhanced spectroscopies, such as surface-enhanced fluorescence and surface-enhanced infrared reflection-absorption spectroscopy, take advantage of this strong electromagnetic near-field enhancement, providing powerful tools for the identification and characterization of chemical species in the vicinity of these hotspots yielding sensitivity down to the single molecule.³⁻⁵

In recent advancements in the field of plasmonics, LSPR excitation has been used to catalyze a variety of chemical processes. As the LSPR decays, high energy hot electrons and hot holes are often generated at the nanostructure surface, followed subsequently by

localized heating of the nanostructure and surrounding medium. When molecules are in the vicinity of a plasmonic nanostructure, LSPR excitation may be used to initiate or catalyze a chemical reaction through localized electric field enhancement, local heating, or the injection of hot charge carriers into chemical species.⁶⁻⁷ Reactions may also be driven by two or more of these effects working synergistically. Numerous examples of plasmon-driven chemical reactions have been reported, including H₂ dissociation,⁸ N₂ dissociation,⁹ conversion of aldehydes to esters,¹⁰ polymerization reactions,¹¹⁻¹² decomposition of organic molecules,¹³⁻¹⁵ and catalytic oxidation reactions such as ethylene epoxidation, CO oxidation, and NH₃ oxidation.¹⁶

Rising interest in plasmon-mediated chemistry has brought about the emergence of a new research area stemming from the integration of plasmonics into the field of surface chemistry. Upon LSPR excitation, metallic nanoparticles exhibit near-field enhancements, hot electron production, and elevated temperatures at highly localized hotspots on the nanostructure surface that can be used to photo-control surface reactions. Thus, plasmon-mediated chemistry offers the possibility to site-selectively catalyze surface functionalization or modification reactions at specific localized reactive areas on nanostructure surfaces with a high degree of spatial control down to the nanoscale. For example, Kadodwala *et al.* presented a novel strategy for the spatially selective plasmon-mediated functionalization of nanomaterials by using chiral plasmonic gold nanostructures as nanosources of heat at the LSPR hotspots.¹⁷ In this strategy, the chiral plasmonic structures were coated with thermally responsive PEG-thiol SAMs that, at higher temperatures (above ~330 K), undergo a conformational change from a helical to an elongated form,¹⁸ freeing up space on the plasmonic structure to allow adsorption of other ligands or biomolecules.¹⁷ Though LSPR decay is known to induce uniform heating of metal nanostructures as a result of rapid heat dissipation from hotspots, it can also cause the formation of localized temperature gradients in surrounding aqueous medium. Chiral plasmonic substrates coated with PEG-thiol SAMs were immersed in water and irradiated with an 8-nanosecond pulse laser, causing localized water heating at the plasmonic hotspots which induced the conformational change of the PEG molecules from helical to elongated at specifically at the hotspots on the nanostructures.¹⁷ This change subsequently promoted the self-assembly of nitrilotriacetic acid ligands in the exposed

regions.¹⁷ This plasmon-mediated spatially selective surface modification methodology highlights and demonstrates the potential for nanoscale control over surface functionalization using plasmon-mediated chemistry.

Currently, alkanethiol SAMs remain one of the most popular choices for functionalizing metal surfaces. However, metal surface functionalization via the reduction of diazonium salts is becoming an increasingly promising alternative to SAMs. Grafting aryl diazonium salts to metallic surfaces allows the covalent immobilization of strong, stable organic layers (Au–C bond strength of $\sim 37 \text{ kcal mol}^{-1}$)¹⁹ that can be customized to display a wide array of terminal functional groups.²⁰ Further, aryl diazonium salt chemistry is highly compatible with plasmon-mediated surface functionalization, as diazonium salts are well-known for their ability to graft onto various types of surfaces by electron transfer.²¹⁻²² Several groups have recently demonstrated the plasmon-mediated grafting of aryl diazonium salts to plasmonic nanoparticles via hot electron donation. Felidj, Mangeney, and coworkers pioneered this approach to surface functionalization, reporting the plasmon-mediated grafting of aryl thin films onto gold nanostripes in the regions of maximum near-field enhancement by submerging gold nanostripe arrays in an aqueous solution of 4-(2-hydroxyethyl)-benzene diazoniumtetrafluoroborate salt and irradiating with a laser for several minutes.²³ This was shortly followed up with a similar study by the same groups wherein gold nanorods were site-specifically functionalized at each of their ends, corresponding to the LSPR hotspots of the nanorods, via plasmon-mediated aryl diazonium salt grafting.²⁴ In each case, laser irradiation of the gold nanostructures immersed in diazonium salt solution regioselectively triggered the grafting of aryl thin films to the nanostructure surfaces at the locations of LSPR hotspots, where hot electrons are generated as a result of LSPR decay. As described briefly in Chapter 1.2.2, Lacroix *et al.* also employed this strategy to demonstrate the localized hot electron-driven reduction of aryl diazonium salts, resulting in the grafting of aryl films specifically at the vertices of triangular gold nanostructures, in alignment with the plasmonic hotspots of the structures.²⁵ Furthermore, the excitation of different plasmon modes on a given metallic nanostructure may allow the opportunity for multi-functionalization. For example, Felidj *et al.* have reported the regiospecific grafting of two distinct diazonium-derived molecules with different terminal functional groups to separate sides of gold nanodisks

by altering the polarization of the incident laser used for grafting, thus changing the locations of the hotspots.²⁶

Chemical attachment of diazonium salts can also occur spontaneously on some surfaces, and can be promoted by heating. However, very thin layers (less than 4 nm) typically form, and the thickness of the film and efficiency of the grafting process depend on the nature of the diazonium salt.²⁵ Additionally, spontaneous grafting of diazonium salts most often requires relatively high solution concentrations and can take several hours to complete.²⁷⁻²⁹ Conversely, the plasmon-mediated grafting of diazonium salts on a plasmonic surface takes place in a matter of seconds or minutes under light irradiation, and can result in thin or thicker polyphenylene layers (up to 30 nm) using much lower diazonium salt concentrations.²³ Furthermore, plasmon-mediated grafting enables localization and spatial control over the grafted areas. Plasmonically grafted aryl thin films can be exploited for many applications, such as adhesion primers³⁰ and antifouling coatings.³¹ Because of their ease of preparation, compatibility with a wide range of materials, strong covalent bonding to metal surfaces, and customizability and large diversity of choices available for terminal functional groups on aryl diazonium salts, these plasmon-grafted thin films also have the potential to be used in the fabrication of interfaces for molecular sensors and biosensors.³²⁻³³ The regiospecificity of the approach may even serve to improve detection for biosensing applications using SERS, as the grafted receptor molecules, and consequently the analytes, would be concentrated in hotspots where the SERS enhancement is strongest.²⁴ The plasmon-mediated grafting of diazonium salts is also of great interest for the development of ensemble molecular junctions in nanoelectronic devices.³⁰ An ensemble molecular junction can easily be generated by plasmonically grafting aryl layers directly between two metal electrodes.^{25,34}

In this work, the plasmon-mediated grafting of diazonium salts is investigated on plasmonic substrates patterned with gold nanoparticles (AuNPs). Patterning is achieved using microcontact printing (μ CP), a simple, versatile, and cost effective soft lithography technique for chemically patterning surfaces.³⁵⁻³⁶ μ CP delivers large-scale surface area coverage (up to several tens of cm^2) with precise and well-defined microscale and sub-

micron patterning.³⁵⁻³⁶ It utilizes elastomeric polydimethylsiloxane (PDMS) “stamps” to transfer a pattern of functionalization onto a substrate with a solution of the target substance acting as the “ink”. μ CP is most often employed for biochemical applications, and has been shown to effectively pattern DNA,³⁷⁻³⁸ proteins,³⁹⁻⁴⁰ cell adhesion components,⁴¹⁻⁴³ and SAMs of organic molecules⁴⁴⁻⁴⁶ on a variety of substrates. There are also some reported instances wherein μ CP has been used to pattern metallic nanoparticles, with suspensions of the metallic nanoparticles used as the ink patterned directly onto the target substrate surface.⁴⁷⁻⁴⁹ Reproducible, controllable, structured, dense, and non-aggregated assemblies of metallic nanoparticles are of fundamental interest as they promise intriguing physicochemical properties with a broad range of applications across several research fields, such as biosensing and biomedicine,⁵⁰⁻⁵¹ information storage,⁴⁹ optics,⁵² electronics,⁵³⁻⁵⁴ and plasmon-enhanced spectroscopies.⁵⁵

When using AuNP solution directly as the ink for μ CP, several extra steps often have to be taken to concentrate AuNPs or arrange them into uniform arrays before they are applied to the stamp, otherwise it can be difficult to achieve uniform patterning and consistent spacing of the nanoparticles over a sufficiently large area of the target substrate.⁴⁸⁻⁴⁹ An alternative approach to the direct patterning of AuNPs is to instead pattern an organic molecular monolayer or thin film onto the substrate as an adhesion template to spatially guide the adsorption of the AuNPs onto the pattern from solution. One ideal candidate for directing the adsorption of well-ordered arrays of nanostructures onto a surface is the self-assembly of block copolymer (BCP) thin films.⁵⁶⁻⁶⁰ Although the binding of the BCP to the surface is not covalent, the multiple interactions between the polymer and the substrate surface collectively yield high stability and surface coverage.⁵⁷ Furthermore, the immiscibility of the polymer blocks causes microphase separation of the blocks in thin films, resulting in the formation of nanoscale hydrophilic and hydrophobic domains of high uniformity and long-range order that can be used to control nanoparticle adsorption.^{57,61}

In the present work, plasmonic platforms are fabricated by patterning substrates with microscale parallel lines, modelled after a diffraction grating, using μ CP of polystyrene-*block*-poly(4-vinylpyridine) (PS-*b*-P4VP) and subsequent adsorption of AuNPs. The

LSPR activity of the AuNP-patterned substrates is probed through SERS imaging of substrates functionalized with 4-nitrothiophenol (4-NTP). The plasmon-mediated grafting of 4-nitrobenzenediazonium (4-NBD) onto the patterned substrates is explored.

4.2 Methods

All purchased reagents and materials were used as received. Gold(III) chloride trihydrate, sodium citrate, hydroquinone, 4-NTP, and 4-NBD tetrafluoroborate were purchased from Sigma-Aldrich. Concentrated HCl and H₂SO₄ were purchased from Caledon Laboratories, and concentrated HNO₃ was purchased from Anachemia Canada. The solvent tetrahydrofuran (THF) was purchased from Thermo Fisher Scientific, and anhydrous ethanol was purchased from Greenfield Global.

4.2.1 Synthesis of AuNPs

Gold nanoparticles were synthesized using a seeded growth approach. Seed AuNP solutions were prepared by a standard sodium citrate reduction method.⁶² First, a 1% (w/v) chloroauric acid solution was prepared by dissolving 0.25 g of H₂AuCl₄ • 3H₂O in 25 mL of ultrapure water. A 1% (w/v) solution of sodium citrate was then prepared by dissolving 0.05 g of sodium citrate in 5 mL of ultrapure water. Next, 300 μL of the 1% H₂AuCl₄ solution were placed into a 250 mL Erlenmeyer flask with 30 mL of ultrapure water and heated to a boil with vigorous stirring. As soon as the solution was boiling, 900 μL of 1% sodium citrate solution were added to the flask. The solution was kept at a boil with stirring until a colour change to deep wine red was observed, about 10 minutes after the addition of sodium citrate. The flask was then removed from heat and cooled at room temperature with gentle stirring.

From the seed particles, 10 mL batches of AuNPs approximately 100 nm in diameter and with a raspberry-like morphology were synthesized using a protocol adapted from Yang *et al.*⁶³ First, a 1% sodium citrate solution and a 1% H₂AuCl₄ solution were each prepared as previously described. A 0.03 M solution of hydroquinone was also prepared by dissolving 16.52 mg of hydroquinone in 5 mL of ultrapure water. Then, 9.42 mL of ultrapure water, 100 μL of 1% H₂AuCl₄ solution, and 30 μL of the seed AuNP solution were placed in a 20 mL scintillation vial and stirred rapidly at room temperature for 5

minutes. Next, 22 μL of 1% sodium citrate solution were added to the vial, immediately followed by the addition of 250 μL of the 1% hydroquinone solution. The mixture was stirred vigorously at room temperature for 1 hour to allow the complete formation of the raspberry-like AuNPs. The resulting AuNP solution was dark blue in colour.

4.2.2 Fabrication of PDMS Stamps

Magnetic microstructured PDMS stamps were fabricated by molding PDMS (Sylgard™ 184, The Dow Chemical Company) over a 600 lines/mm diffraction grating (Edmund Optics, Inc.). PDMS prepolymer solution was prepared by combining the polymer base and curing agent in a 10:1 ratio, mixing thoroughly, and then degassing for 15 minutes. The degassed prepolymer was poured over the grating, used as the master pattern, in a Teflon dish so that there was a 1-3 mm thick layer of PDMS covering the surface of the grating. This was degassed once more for 10 minutes and then partially cured in a 60 °C oven for 1 hour. To make the magnetic layer, PDMS prepolymer was mixed with iron powder (Goodfellow Cambridge, Ltd., 60 μm diameter Fe particles) in a 50:50 (w/w) ratio. This mixture was alternately stirred for 5 minutes then degassed for 15 minutes for three cycles. The degassed Fe-PDMS mixture was then poured over the partially cured PDMS in a 1-3 mm thick layer. Once poured, it was degassed for another 10 minutes and then fully cured in a 60 °C oven overnight.

4.2.3 Patterning of Glass Substrates via Microcontact Printing

Patterned substrates were fabricated via μCP using the InnoStamp 40™ (Innopsys) instrument. The InnoStamp 40™ is a fully automated magnetic-field-assisted microcontact printer that utilizes a movable head containing a set of four magnets (NdFeB magnets, 25 mm \times 25 mm \times 12 mm) to manipulate the position of an Fe-PDMS stamp in order to carry out all of the steps in a standard μCP process. A typical μCP experiment consists of five steps: stamp loading, inking, drying, printing, and stamp unloading. To set up a μCP experiment, an Fe-PDMS stamp was placed, with the patterned side facing down and magnetic side facing up, in the centre of the stamp loading area in the InnoStamp 40™. A clean substrate, in this case a 22 x 22 mm (thickness #1) glass coverslip, was placed at the centre of the printing area and secured in

place with copper tape at two opposite corners of the coverslip. Prior to printing, the glass coverslips were cleaned by immersion in a 3% (w/v) solution of Nochromix (Godax Laboratories, Inc.) in concentrated H_2SO_4 at 80°C for 30 minutes. Cleaned substrates were rinsed five times with ultrapure water and then dried under a stream of N_2 gas. Lastly, an ink platform was placed in the inking area of the InnoStamp 40TM and the molecular ink was loaded onto the platform. For the fabrication of substrates patterned with AuNPs, a clean glass microscope slide was used as the ink platform, and the ink used was a 0.05 mg/mL solution of PS-*b*-P4VP ($M_n(\text{PS}) = 41 \text{ kg/mol}$, $M_n(\text{P4VP}) = 20 \text{ kg mol}^{-1}$, M_w/M_n (total) = 1.18, Polymer Source, Inc.) in THF. A 0.5 mg/mL stock solution of PS-*b*-P4VP was prepared by placing 7.5 mg of solid PS-*b*-P4VP in 15 mL of THF, gently sonicating too dissolve, and then filtering successively through 0.45 μm and 0.2 μm polytetrafluoroethylene filters (Chromspec). The 0.05 mg/mL PS-*b*-P4VP solutions were then prepared as needed by diluting portions of the 0.5 mg/mL solution using THF. To load the ink, a few mL of the 0.05 mg/mL PS-*b*-P4VP solution were pipetted onto the microscope slide in the inking area such that the surface of the solution was visibly convex, resulting in a layer of solution that reached 2-3 mm above the surface of the microscope slide. A schematic of the InnoStamp 40TM working areas and their contents preceding a μCP experiment are shown in Figure 4.1.

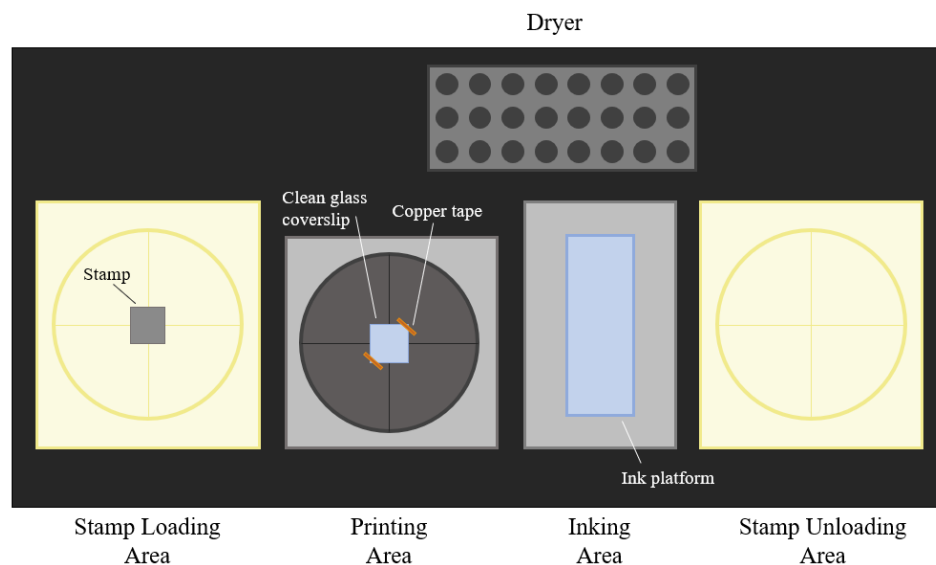


Figure 4.1: Top view schematic of the InnoStamp 40TM working areas and experimental apparatus.

For each μ CP experiment, the InnoStamp 40™ instrument followed a custom protocol to move the stamp through each step of the printing process. In the loading step of a μ CP experiment, the InnoStamp 40™ stamp head is lowered to the magnetic surface of the Fe-PDMS stamp to pick it up. The stamp head then moves the stamp over to the inking area, where the stamp is lowered toward the ink platform until the patterned surface of the stamp is in full contact with the surface of the PS-*b*-P4VP ink. The patterned side of the stamp is held immersed in the ink solution for one minute. After inking, the stamp is moved to the dryer area, where it is dried with air using a turbine for 3 minutes. Once dried, the stamp is moved and slowly lowered over the centre of the clean glass coverslip in the printing area, and the stamp is released onto the substrate. A set of magnets underneath the printing area generate a magnetic field to bring the stamp into conformal contact with the substrate and apply stamping pressure, ensuring a homogenous printed pattern. During the printing step, these magnets move closer to the printing platform to increase the force of the stamp pressing down on the substrate. In the stamping protocol used here, the magnets move to their maximum position and remain for 4 minutes. The magnets then lower, and the stamp head removes the stamp from the substrate, leaving behind thin films of PS-*b*-P4VP only in areas on the substrate that were in contact with the stamp. The stamp head then deposits the stamp in the stamp unloading area, concluding the μ CP process.

Following patterning with PS-*b*-P4VP via μ CP, the substrates were coated with 100 nm raspberry-like AuNPs over the PS-*b*-P4VP thin films. Glass coverslips patterned with PS-*b*-P4VP were placed in 20 mL beakers such that they were propped up at an angle in the beaker, and a stir bar was placed in the bottom of each beaker in the space below the coverslip. Coverslips were then fully immersed in 10 mL of AuNPs suspended in ultrapure water, as synthesized. Coverslips remained immersed in AuNP solution with gentle stirring for 2 hours, then were rinsed three times with ultrapure water and dried under a stream of N₂ gas.

4.2.4 Visible – Near-Infrared Absorption Measurements

Visible – near-infrared (vis-NIR) absorption measurements were performed to determine the plasmon resonance positions of the lines of AuNPs patterned onto glass coverslips.

These measurements were carried out using a home-built setup featuring a halogen lamp (HL-2000, Ocean Optics, Inc.) passed through a polarizer and connected by a 100 μm optical fibre to a Nikon Diaphot inverted optical microscope. The beam from the halogen lamp was first expanded by a 10 \times objective (numerical aperture (NA) = 0.25), and then recollimated by a 20 \times objective (NA = 0.40) onto the sample, resulting in a spot with a diameter around 50 μm . The light was transmitted through the sample and collected by a 20 \times objective (NA = 0.50, UPlanFL N, Olympus Corporation). A pinhole size of 200 μm and a diffraction grating of 600 lines/mm were used. Scattered light was analyzed using a USB 4000-VIS-NIR-ES spectrometer (Ocean Optics, Inc.). Spectra were collected in the 400-1000 nm range, with an acquisition time of 1 second per spectrum and at least 50 accumulations to improve the signal-to-noise ratio.

4.2.5 SAM Formation on AuNP-Patterned Surfaces

Patterned substrates were functionalized with SAMs of 4-NTP by immersion in a 5 mM solution of 4-NTP in ethanol for 1 hour. Functionalized substrates were rinsed three times with ethanol and blown dry with nitrogen gas.

4.2.6 Plasmon-Mediated Grafting of Aryl Diazonium Salts

In order to demonstrate that LSPR excitation on the plasmonic substrates patterned with AuNPs can locally activate and enhance surface functionalization, patterned coverslips were covered with a solution of 4-NBD and irradiated using a laser source to induce the plasmon-mediated reduction of the diazonium salt, resulting in the grafting of 4-NBD to the surfaces of the AuNPs in the irradiated spot. To achieve this, the surfaces of the substrates were first examined using an inverted optical microscope (IX71, Olympus Corporation) to locate the patterned areas. Substrates were placed with the patterned face upwards, and when a patterned area was located, a Teflon O-ring (1 cm diameter) was placed over the area. A 5 mM solution of 4-NBD tetrafluoroborate was prepared by dissolving 11.95 mg in 10 mL of ultrapure water. Then, 45 μL of the 5 mM 4-NBD solution were pipetted into the Teflon ring on the patterned surface of the substrate. The area was illuminated with a 632.8 nm laser, polarized parallel to the lines of AuNPs and focused using a 20 \times objective (NA = 0.50, UPlanFL N, Olympus Corporation) in

transmission, for 2-5 seconds. Irradiation was carried out with the laser slightly out of focus to reduce the power density at the surface and to induce grafting over a larger area than would be possible with a focused laser spot. Following the grafting procedure, coverslips were rinsed three times with ultrapure water. The setup configuration used for grafting is shown in Figure 4.2.

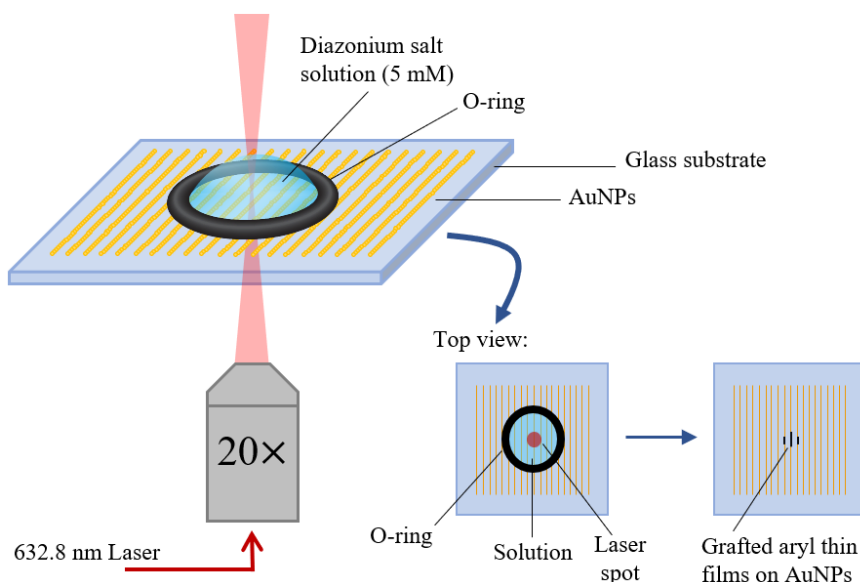


Figure 4.2: Schematic diagram representing the setup and procedure for plasmon-mediated grafting of diazonium salts under laser irradiation.

4.2.7 Surface-Enhanced Raman Spectroscopy

Raman and SERS spectra were obtained using a Horiba HR LabRAM Raman spectrometer connected to an inverted optical microscope (IX71, Olympus Corporation). A 100 \times optical objective (NA = 0.9, MPlanFL N, Olympus Corporation) was used to focus the 632.8 nm excitation laser onto the sample from below, and the same objective was used to collect the Raman-scattered light. The Raman signal was detected by a liquid nitrogen-cooled charge-coupled device (CCD; Horiba, Symphony), with the fundamental laser line removed by a notch filter. The temperature of the CCD was typically -119 $^{\circ}$ C. The signal was collected with a 600 lines/mm grating and the spectrometer pinhole set to a width of 200 μ m. Spectra were recorded in the range of 800 – 1800 cm^{-1} with an acquisition time of 5 seconds per spectrum. For SERS mapping experiments of 4-NTP or

4-NBD on AuNP-patterned substrates, an acquisition time of 1 second was used. A schematic diagram of the setup used for SERS measurements is shown in Figure 4.3.

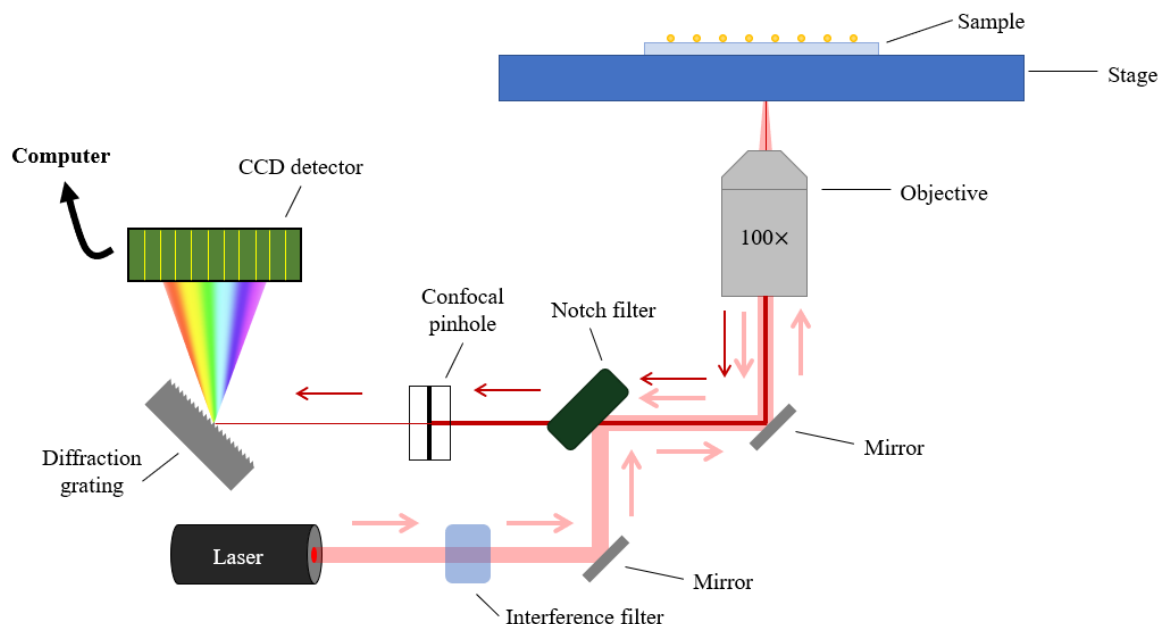


Figure 4.3: Schematic diagram of the setup for the measurement of SERS spectra.

4.2.8 Scanning Electron Microscopy

A LEO Zeiss 1530 scanning electron microscope (SEM) was used for imaging micropatterned substrates, and for imaging areas where the plasmon-mediated grafting of diazonium salts had occurred. A 3 nm layer of osmium was deposited onto the substrates before imaging.

4.3 Results and Discussion

4.3.1 Fabrication of AuNP-Patterned Substrates

To construct unique plasmonic platforms, AuNPs were synthesized and patterned onto glass substrates via μ CP. AuNPs were grown using a seeding method with hydroquinone as the reducing agent.⁶³ The resulting nanoparticles were approximately 100 nm in diameter and had a bumpy, “raspberry-like” surface morphology. The size and shape of the AuNPs were characterized by SEM imaging, shown in Figure 4.4.

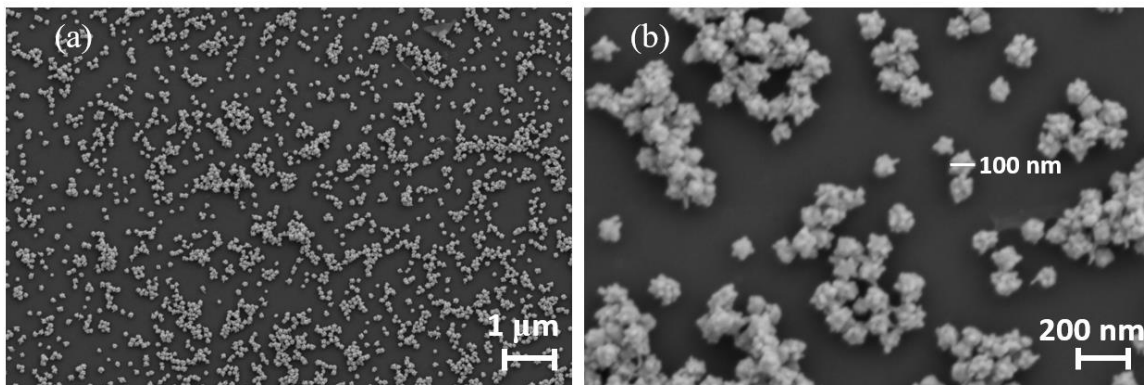


Figure 4.4:(a) SEM image of raspberry-like AuNPs; (b) SEM image at a higher magnification, to show more accurately the size and morphology of the AuNPs.

Non-spherical and textured nanoparticles are a subject of interest in plasmonics because, as discussed in Chapter 2.4.2, the optical and electronic properties of metallic nanoparticles depend not only on the size but also the shape of the nanoparticles.⁶⁴⁻⁶⁵ Plasmonic nanoparticles are highly sensitive to changes in geometry, and thus variations in shape and surface structure may be used to control their LSPR properties. Gold nanoparticles have been formed in a wide variety of shapes, including rods,⁶⁶ cubes,⁶⁷ stars,⁶⁸ plates,⁶⁹ and prisms.⁷⁰ Each unique geometry produces LSPR hotspots in different locations and with different levels of enhancement compared to spherical particles due to the anisotropic distribution of the electric field at the nanoparticle surfaces.⁶³ Raspberry-like AuNPs were desired for the present application as it has been reported that particularly intense near-field enhancement exists at the tips of branched AuNPs, generating strong LSPR activity.^{68,71-72}

Following AuNP synthesis, microscale parallel lines of AuNPs were patterned onto glass coverslips. A PDMS stamp was molded using a 600 lines/mm diffraction grating as the master pattern, and then μ CP was used to transfer lines of PS-*b*-P4VP thin films onto clean glass coverslips. Coverslips were then immersed in AuNP solution, and adsorption of the AuNPs onto the substrates was guided by the patterned copolymer thin films, resulting in glass substrates patterned with lines of AuNPs. The fabricated substrates were characterized by SEM imaging, shown in Figure 4.5a and b. The patterned lines were found to be approximately 0.2 μ m thick with a periodicity of 1.7 μ m.

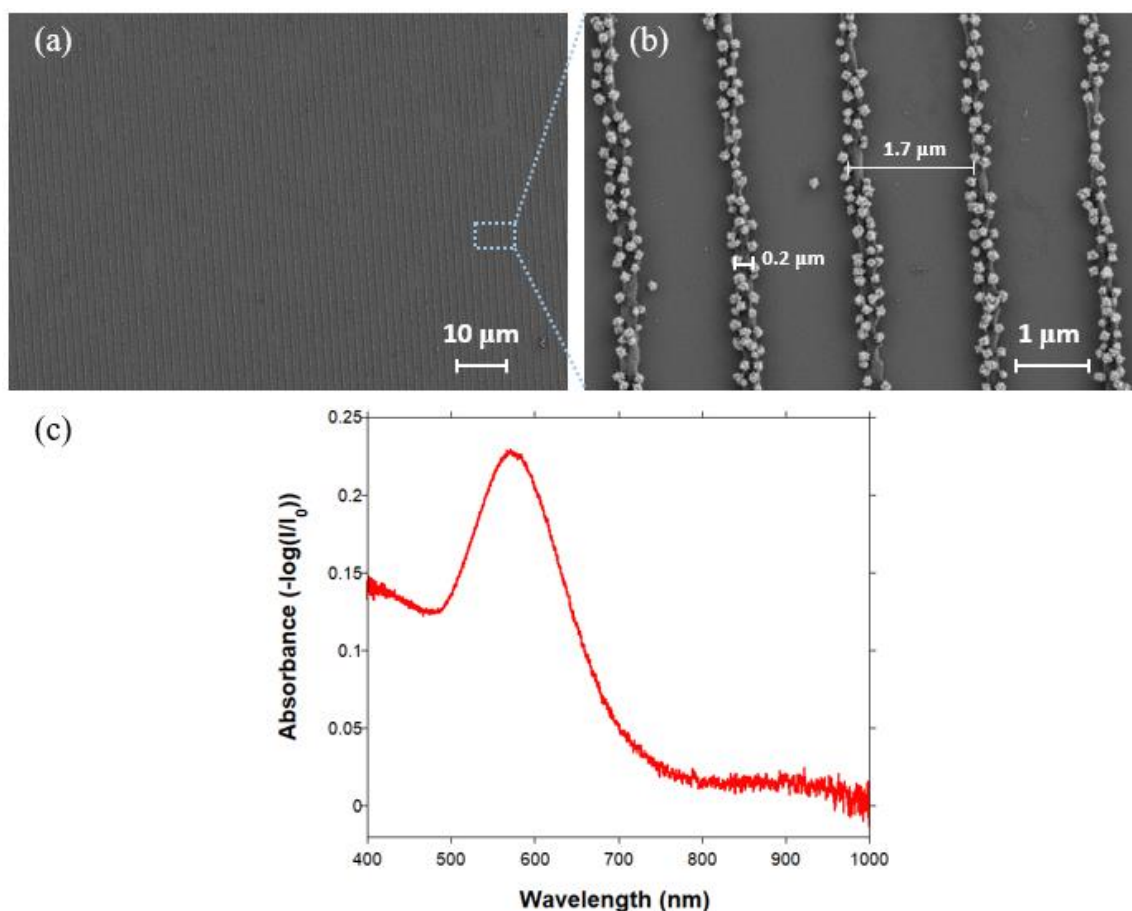


Figure 4.5: (a) SEM image of the AuNP-patterned substrate; (b) SEM image of the AuNP-patterned substrate at a higher magnification to show AuNP distribution and line periodicity; (c) Absorbance spectrum of the AuNP-patterned substrate.

LSPR occurs when the collective oscillation of free electrons in a metallic nanoparticle interacts with and absorbs incident electromagnetic radiation. Plasmonic nanoparticles only couple with light at specific wavelengths that correspond to the frequency of electron oscillation, which is dependent on the nanoparticle size, shape, and chemical composition.⁶⁴⁻⁶⁵ These select wavelengths can be analyzed with absorption spectroscopy. Absorption spectra are often used to determine the wavelengths of maximum absorbance for a plasmonic material, referred to as its plasmon resonances. The plasmon resonance positions are important to identify as they reveal which wavelengths should be used in order to most efficiently excite the LSPR mode of a given nanostructure. To find the optimal excitation wavelength for SERS and for the plasmon-

mediated grafting of diazonium salts, an absorption spectrum was collected of an AuNP-patterned substrate, shown in Figure 4.5c. Vis-NIR absorption measurements were carried out in transmission mode through the sample. The detected signal was compared to that of a clean “blank” coverslip, and the extinction spectrum was obtained by calculating their ratio. The resonance position of the AuNP-patterned substrate was found to be 580 nm. Thus, a 632.8 nm excitation wavelength was chosen for subsequent SERS measurements and plasmon-mediated surface reactions.

4.3.2 Validation of AuNP-Patterned Substrates as Plasmonically Active Platforms

Prior to pursuing the plasmon-mediated grafting of diazonium salts, the LSPR activity of the AuNP-patterned substrates was first examined by probing their SERS capabilities. The AuNPs were functionalized with SAMs of 4-NTP by immersion of the patterned substrates in a 5 mM solution of 4-NTP for 1 hour, followed by thorough rinsing with ethanol. SERS mapping was then performed on the functionalized sample in a 7.0×4.1 μm area using a 632.8 nm excitation laser. 20×10 data points were collected with a 1 second acquisition time per point. Separately, a few milligrams of 4-NTP powder were placed on a clean glass coverslip and the Raman spectrum was acquired to act as a reference. 4-NTP was chosen for this experiment as it is a widely studied model molecule and the assignments for its Raman modes have been extensively reported in literature.⁷³ The acquired reference spectrum of bulk 4-NTP is shown in Figure 4.6d. The dominant peaks in the reference spectrum are located at 1575, 1344, 1116, and 1087 cm^{-1} , corresponding to C=C ring stretching, the NO₂ symmetric stretching, C–H bending, and C–H bending coupled with C–S stretching, respectively, in agreement with values reported in literature.⁷³⁻⁷⁵ As the strongest signal in the spectrum of 4-NTP, the SERS map of the patterned substrate was generated using the peak arising from the NO₂ symmetric stretch. The resulting map is displayed in Figure 4.6a, alongside an SEM image in Figure 4.6b of an area on a patterned substrate similar to the mapped area, shown for comparison. Peak assignments for the 4-NTP SAMs are listed in Table 4.1.

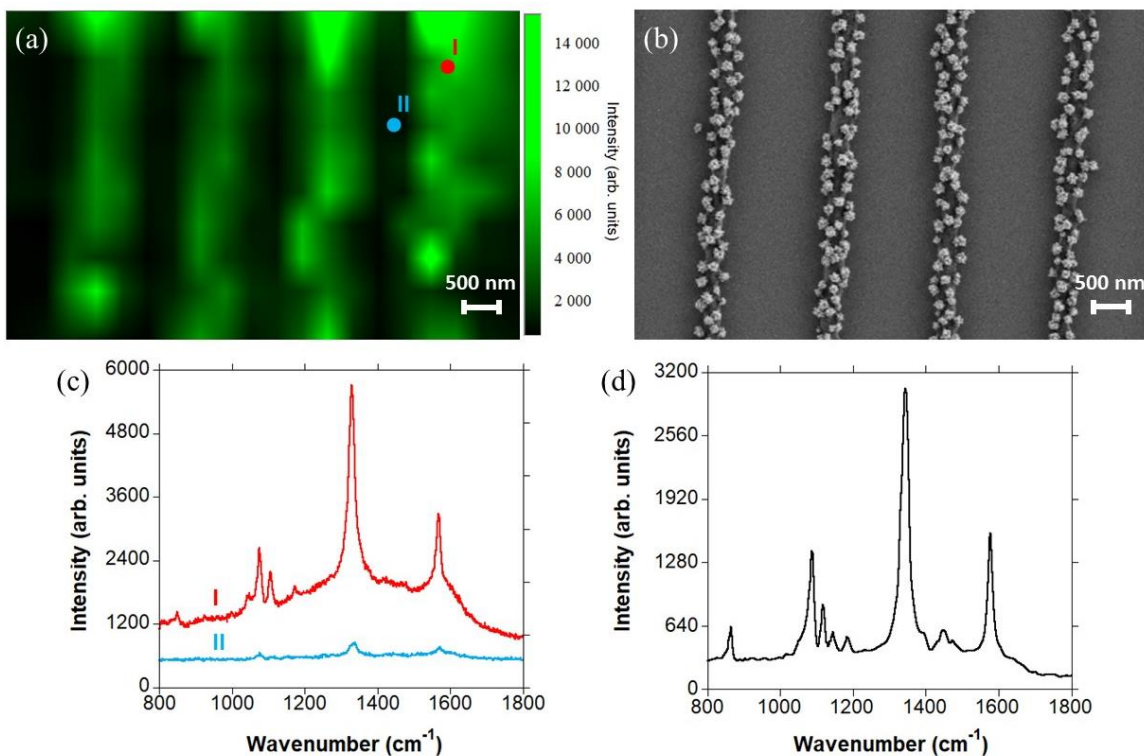


Figure 4.6: (a) SERS mapping composed of 20×10 spectra on the AuNP-patterned substrate, showing variation of the SERS peak intensity at 1332 cm^{-1} for 4-NTP SAMs; (b) SEM image of a similar region as the mapped area; (c) SERS spectra from the positions I and II indicated in (a); (d) Raman spectrum of 4-NTP powder on a glass coverslip.

Table 4.1: SERS spectral peak assignments for the SAMs of 4-NTP on AuNP-patterned substrates.

Frequency (cm ⁻¹)	Assignment
1572	C=C ring stretch
1332	NO ₂ symmetric stretch
1107	C-H bend
1077	C-H bend coupled with C-S stretch

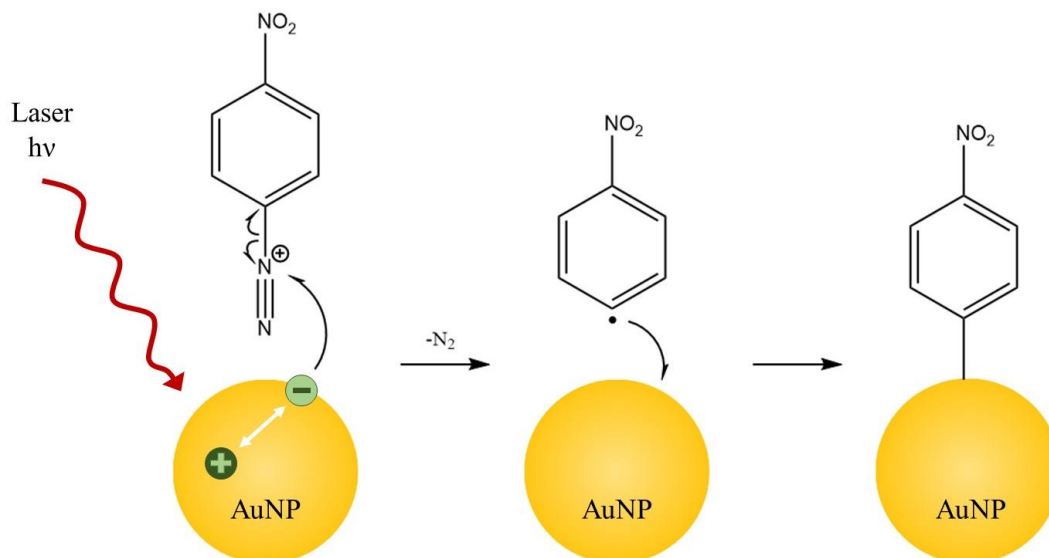
SERS mapping of the AuNP-patterned substrate functionalized with SAMs of 4-NTP revealed patterned SERS enhancement of the 4-NTP signal across the substrate, with the areas of maximum SERS intensity along the lines of AuNPs (Figure 4.6a). Figure 4.6c shows a comparison of two SERS spectra taken from different points in the map, one on a line of AuNPs (point I) and one in the space between two lines (point II). Point I shows strong SERS enhancement of the 4-NTP signals. The feature peaks of 4-NTP appear at 1572, 1332, 1107, and 1077 cm^{-1} , in agreement with values reported in literature for SAMs of 4-NTP on gold nanostructures.⁷⁵⁻⁷⁷ This represents a slight shift in the peak positions compared to the bulk 4-NTP reference spectrum, as is occasionally seen in SERS measurements of 4-NTP.⁷⁵⁻⁷⁷ Point II also contains the key peaks corresponding to 4-NTP, but with significantly weaker signal intensity and lower signal-to-noise ratio. The spectrum obtained at point I, on the AuNPs, is approximately 15 \times more intense than the spectrum obtained at point II, away from the nanoparticles. It might be expected that SERS measurements taken in between the lines of AuNPs would show no trace of 4-NTP; however, because the AuNP lines are only 1.5 μm apart and the laser spot used for SERS is ~ 1 μm in diameter, it is likely that even for measurements seemingly taken on bare regions of the substrate, some nanoparticles are still irradiated, resulting in a very weak SERS signal of 4-NTP at point II and in similar areas.

Successful SERS mapping of the functionalized AuNP-patterned substrates serves to demonstrate their patterned LSPR activity and confirm their suitability for SERS applications. The LSPR activity displayed by these substrates also indicates their potential applicability for plasmon-mediated chemistry.

4.3.3 Plasmon-Mediated Grafting of 4-Nitrobenzenediazonium onto AuNP-Patterned Substrates

In order to show that LSPR excitation on the AuNP-patterned substrates may be exploited to catalyze surface functionalization reactions, the plasmon-mediated grafting of aryl diazonium salts was investigated. The mechanism for this surface reaction is shown in Scheme 4.1. Although there is still some debate, the plasmon-mediated reduction is predominantly considered to proceed via charge transfer. In this process, hot electrons are donated from the AuNPs to the diazonium cations, resulting in the loss of

N_2 gas and the formation of an aryl radical species.^{20,23,27} The highly reactive aryl radicals are then able to bind to the gold surface, forming a covalently linked aryl thin film.



Scheme 4.1: : General reaction mechanism for the plasmon-mediated reduction of 4-NBD by hot electron donation and subsequent grafting of the aryl radical species onto an AuNP.

Grafting was performed by depositing a droplet of 5 mM 4-NBD solution onto the AuNP-patterned coverslip, and then irradiating the sample with a 632.8 nm laser, polarized parallel to the lines of AuNPs, for 5 seconds. The laser power at the surface was ~ 5 mW. Following the grafting, the substrate was rinsed thoroughly with ultrapure water. SERS mapping was carried out using a 632.8 nm excitation laser in a $10 \times 10 \mu\text{m}$ square covering the grafted area. 20×12 data points were collected with a 1 second acquisition time per point. The resultant SERS map is shown in Figure 4.7a. Once SERS maps were acquired, the substrate surface was further characterized via SEM imaging, displayed in Figure 4.7b. A reference Raman spectrum of 4-NBD was collected from a few milligrams of 4-NBD powder placed on a clean glass coverslip. 4-NBD was selected for these experiments over other diazonium salts because, like 4-NTP, it contains an NO_2 group with strong Raman signals. The reference spectrum is presented in Figure 4.7d. The dominant peaks in the reference spectrum are located at 1575, 1355, 1104, and 1066 cm^{-1} , which have been assigned to C=C ring stretching, NO_2 symmetric stretching, and two C-H bending modes, respectively.

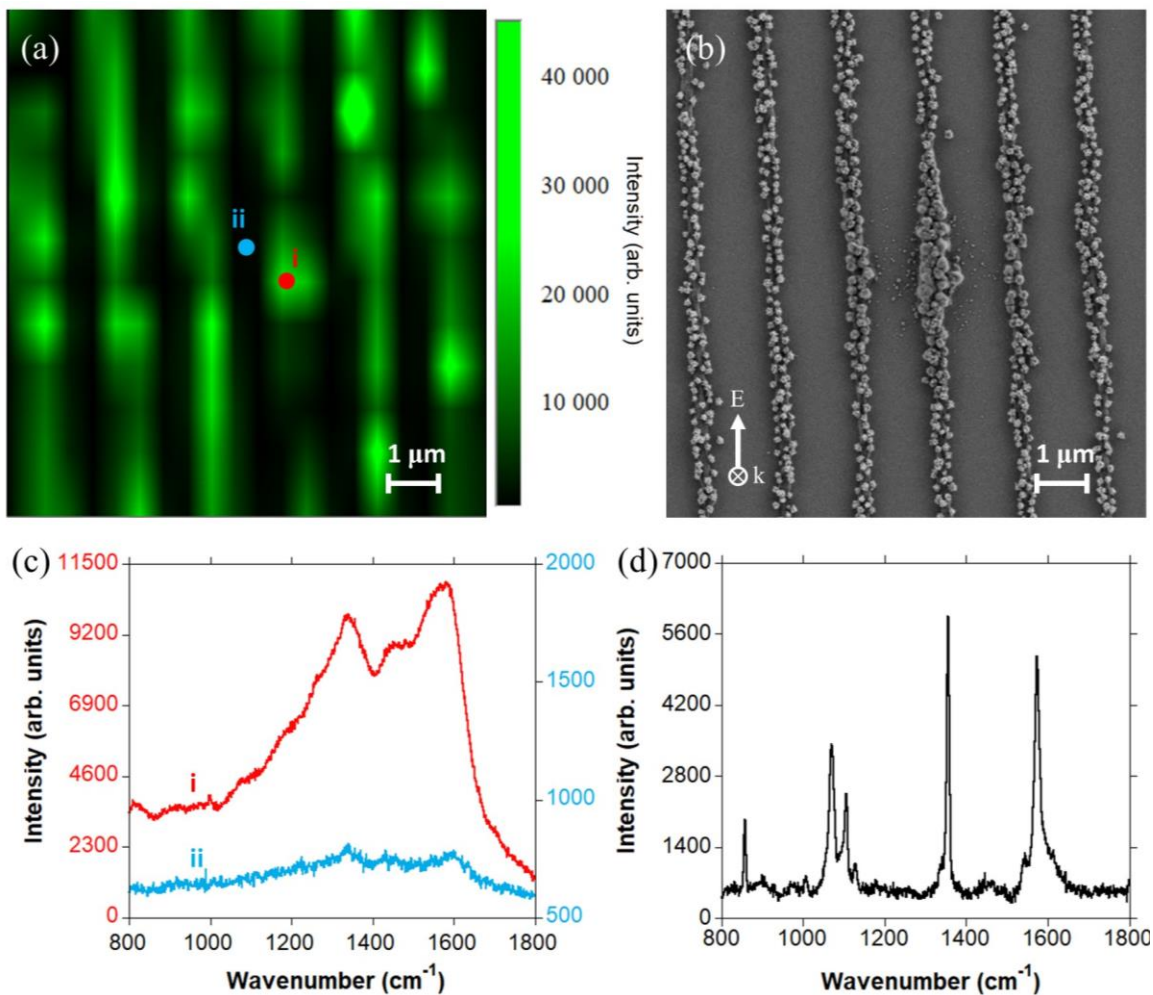


Figure 4.7: (a) SERS mapping composed of 20×12 spectra on the grafted substrate, showing variation of the SERS intensity at 1575 cm^{-1} ; (b) SEM image of the grafted region; (c) SERS spectra from the positions i and ii indicated in (a); (d) Raman spectrum of 4-NBD powder on a glass coverslip.

Table 4.2: Raman peak assignments for bulk 4-NBD.

Frequency (cm^{-1})	Assignment
1575	C=C ring stretch
1355	NO_2 symmetric stretch
1104	C-H bend
1066	C-H bend

The SEM image of the grafted substrate in Figure 4.7b shows a buildup of material preferentially along the AuNP lines within the irradiated area, indicating successful plasmon-mediated functionalization of the AuNPs. The aryl thin films appear to encase each nanoparticle within the laser spot reaching across an approximately $5 \times 5 \mu\text{m}$ area, with film thickness decreasing away from the centre of the spot where the laser intensity is greatest. Interestingly, some scattered specks of material are also seen adsorbed to the glass substrate between the AuNP lines, suggesting that the grafting may also in part be heat- or photo-induced.

As expected, SERS mapping of the grafted region (Figure 4.7a) showed overall increased SERS intensity along the lines of AuNPs compared to the spaces between the lines. Figure 4.7c shows a comparison of two SERS spectra taken from different points in the map, one on a line of AuNPs where significant grafting was observed (point i) and one in the space between two lines (point ii). Surprisingly, the expected peaks of 4-NBD were not detected at either point. Instead, the spectrum at point i contains two large, broad signals at 1341 and 1575 cm^{-1} . For this reason, the SERS map in Figure 4.7a was generated using the variation in intensity of the broad peak at 1570 cm^{-1} . Point ii contains these same peaks, but at an intensity about $20\times$ lower than that at point i. This spectrum was observed across the entire mapped area. Rather than aligning with the reference spectrum of 4-NBD, these broad peaks at 1575 and 1340 cm^{-1} are instead highly consistent with the typical G-band and disorder-induced D-band, respectively, of amorphous carbon.⁷⁸⁻⁸⁰ This strongly suggests that the sample was damaged by burning, either during SERS mapping or during the grafting process, caused by overexposure to the laser.

To lessen the adsorption of diazonium salts to the glass between the lines of AuNPs and potentially reduce burning of the aryl layers, the plasmon-mediated grafting was repeated with the irradiation time reduced from 5 seconds to 2 seconds. SEM images of the grafted region is shown in Figure 4.8.

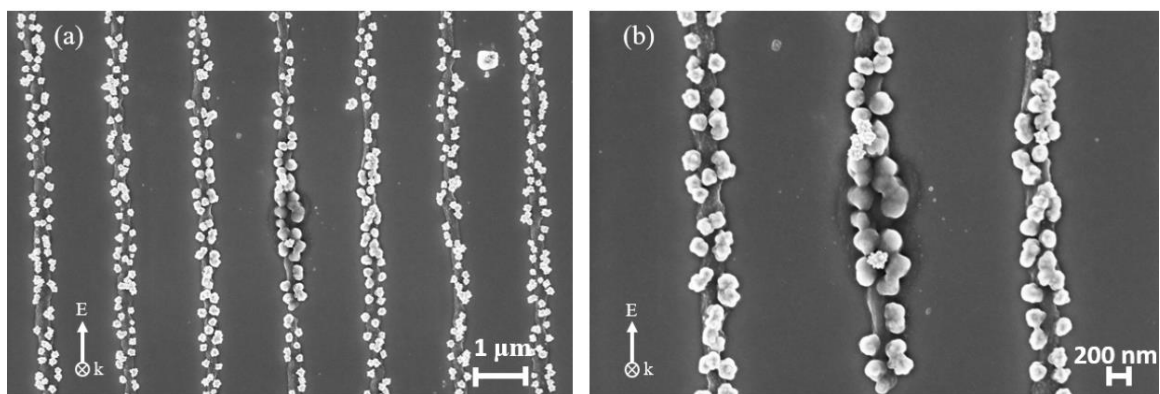


Figure 4.8: SEM images of (a) an AuNP-patterned substrate grafted with 4-NBD using a 2-second irradiation time; (b) the grafted area at a higher magnification.

Decreasing the irradiation time used for the plasmon-mediated grafting of 4-NBD significantly reduced non-plasmon-mediated absorption of the diazonium salts to the glass between AuNP lines. As with the previous sample, plasmon-induced grafting of 4-NBD has resulted in a buildup of aryl thin films preferentially along the AuNP lines within the irradiated area, encasing each particle with thin films decreasing in thickness farther away from the centre of the laser spot. For further characterization, SERS mapping parameters must be optimized to prevent burning of the sample while maintaining sufficient signal intensity to produce quality spectra.

4.4 Conclusions

In this work, a new methodology was developed for fabricating robust and reproducible micropatterned LSPR platforms via μ CP of block copolymer thin films and subsequent adsorption of raspberry-like AuNPs. As a proof-of-concept experiment to establish the SERS capabilities of these LSPR platforms, SERS mapping of AuNP-patterned substrates functionalized with SAMs of 4-NTP was performed. The patterned substrates were then employed for the plasmon-mediated reduction of diazonium salts, resulting in the grafting of aryl thin films to the surfaces of the AuNPs, visualized by SEM.

Although SEM images of the AuNP-patterned substrates functionalized with 4-NBD appear to suggest successful plasmon-mediated grafting of the diazonium salts, SERS mapping did not reveal the corresponding Raman peaks for 4-NBD. Instead, evidence of

partial transformation of the aryl layers into carbonaceous materials is observed, an indication of local overheating. In future experiments, the laser power and exposure time for both grafting and SERS mapping must be optimized in order to properly achieve surface functionalization and characterization without damaging the aryl layers. If successful, this method of plasmon-mediated grafting would not only represent a means for functionalizing plasmonic nanoparticles, but also provide a potential strategy to site-specifically immobilize a range of diazonium-derived species that may be used in the fabrication of nanoelectronic devices, the development of protective coatings, or as localized receptor molecules for improved molecular sensing and biosensing.

4.5 References

1. Mayer, K. M.; Hafner, J. H. *Chem. Rev.* **2011**, *111*, 3828-3857.
2. Willets, K. A.; Van Duyne, R. P. *Annu. Rev. Phys. Chem.* **2007**, *58*, 267-297.
3. Kherbouche, I.; Luo, Y.; Félidj, N.; Mangeney, C. *Chem. Mater.* **2020**, *32*, 5442-5454.
4. Mun, J.; Lee, D.; So, S.; Badloe, T.; Rho, J. *Appl. Spectrosc. Rev.* **2019**, *54*, 142-175.
5. Fort, E.; Grésillon, S. *J. Phys. D: Appl. Phys.* **2007**, *41*, 013001.
6. Brongersma, M. L.; Halas, N. J.; Nordlander, P. *Nat. Nanotechnol.* **2015**, *10*, 25-34.
7. Kale, M. J.; Avanesian, T.; Christopher, P. *ACS Catal.* **2014**, *4*, 116-128.
8. Mukherjee, S.; Libisch, F.; Large, N.; Neumann, O.; Brown, L. V.; Cheng, J.; Lassiter, J. B.; Carter, E. A.; Nordlander, P.; Halas, N. J. *Nano Lett.* **2013**, *13*, 240-247.
9. Martirez, J. M. P.; Carter, E. A. *J. Am. Chem. Soc.* **2017**, *139*, 4390-4398.
10. Zhang, Y.; Xiao, Q.; Bao, Y.; Zhang, Y.; Bottle, S.; Sarina, S.; Zhaorigetu, B.; Zhu, H. *J. Phys. Chem. C* **2014**, *118*, 19062-19069.

11. Walker, J. M.; Gou, L.; Bhattacharyya, S.; Lindahl, S. E.; Zaleski, J. M. *Chem. Mater.* **2011**, *23*, 5275-5281.
12. Wang, Y.; Wang, S.; Zhang, S.; Scherman, O. A.; Baumberg, J. J.; Ding, T.; Xu, H. *Nano Res.* **2018**, *11*, 6384-6390.
13. Boerigter, C.; Aslam, U.; Linic, S. *ACS Nano* **2016**, *10*, 6108-6115.
14. Boerigter, C.; Campana, R.; Morabito, M.; Linic, S. *Nat. Commun.* **2016**, *7*, 10545.
15. Suh, J. S.; Jang, N. H.; Jeong, D. H.; Moskovits, M. *J. Phys. Chem.* **1996**, *100*, 805-813.
16. Christopher, P.; Xin, H.; Linic, S. *Nat. Chem.* **2011**, *3*, 467-472.
17. Jack, C.; Karimullah, A. S.; Tullius, R.; Khorashad, L. K.; Rodier, M.; Fitzpatrick, B.; Barron, L. D.; Gadegaard, N.; Laphorn, A. J.; Rotello, V. M.; Cooke, G.; Govorov, A. O.; Kadodwala, M. *Nat. Commun.* **2016**, *7*, 10946.
18. Norman, A. I.; Fei, Y.; Ho, D. L.; Greer, S. C. *Macromolecules* **2007**, *40*, 2559-2567.
19. Berisha, A.; Combellas, C.; Kanoufi, F.; Médard, J.; Decorse, P.; Mangeney, C.; Kherbouche, I.; Seydou, M.; Maurel, F.; Pinson, J. *Langmuir* **2018**, *34*, 11264-11271.
20. Betelu, S.; Tijunelyte, I.; Boubekour-Lecaque, L.; Ignatiadis, I.; Ibrahim, J.; Gaboreau, S.; Berho, C.; Toury, T.; Guenin, E.; Lidgi-Guigui, N.; Felidj, N.; Rinnert, E.; Lamy de la Chapelle, M. *J. Phys. Chem. C* **2016**, *120*, 18158-18166.
21. Bakas, I.; Salmi, Z.; Gam-Derouich, S.; Jouini, M.; Lépinay, S.; Carbonnier, B.; Khelifi, A.; Kalfat, R.; Geneste, F.; Yagci, Y.; Chehimi, M. M. *Surf. Interface Anal.* **2014**, *46*, 1014-1020.
22. Heimbürger, D.; Gam-Derouich, S.; Decorse, P.; Mangeney, C.; Pinson, J. *Langmuir* **2016**, *32*, 9714-9721.

23. Nguyen, M.; Lamouri, A.; Salameh, C.; Lévi, G.; Grand, J.; Boubekeur-Lecaque, L.; Mangeney, C.; Felidj, N. *Nanoscale* **2016**, *8*, 8633-8640.
24. Nguyen, M.; Kherbouche, I.; Gam-Derouich, S.; Ragheb, I.; Lau-Truong, S.; Lamouri, A.; Lévi, G.; Aubard, J.; Decorse, P.; Felidj, N.; Mangeney, C. *Chem. Commun.* **2017**, *53*, 11364-11367.
25. Nguyen, V.-Q.; Ai, Y.; Martin, P.; Lacroix, J.-C. *ACS Omega* **2017**, *2*, 1947-1955.
26. Tijunelyte, I.; Kherbouche, I.; Gam-Derouich, S.; Nguyen, M.; Lidgi-Guigui, N.; Lamy de la Chapelle, M.; Lamouri, A.; Lévi, G.; Aubard, J.; Chevillot-Biraud, A.; Mangeney, C.; Felidj, N. *Nanoscale Horiz.* **2018**, *3*, 53-57.
27. Mesnage, A.; Lefèvre, X.; Jégou, P.; Deniau, G.; Palacin, S. *Langmuir* **2012**, *28*, 11767-11778.
28. Barrière, F.; Downard, A. J. *J. Solid State Electrochem.* **2008**, *12*, 1231-1244.
29. Lehr, J.; Williamson, B. E.; Flavel, B. S.; Downard, A. J. *Langmuir* **2009**, *25*, 13503-13509.
30. Santos, L. M.; Ghilane, J.; Fave, C.; Lacaze, P.-C.; Randriamahazaka, H.; Abrantes, L. M.; Lacroix, J.-C. *J. Phys. Chem. C* **2008**, *112*, 16103-16109.
31. Zou, Q.; Kegel, L. L.; Booksh, K. S. *Anal. Chem.* **2015**, *87*, 2488-2494.
32. Hetemi, D.; Noel, V.; Pinson, J. *Biosensors* **2020**, *10*, 4.
33. Cao, C.; Zhang, Y.; Jiang, C.; Qi, M.; Liu, G. *ACS Appl. Mater. Interfaces* **2017**, *9*, 5031-5049.
34. Bléteau, P.; Bastide, M.; Gam-Derouich, S.; Martin, P.; Bonnet, R.; Lacroix, J.-C. *ACS Appl. Nano Mater.* **2020**.
35. Zhao, X.-M.; Xia, Y.; Whitesides, G. M. *J. Mater. Chem.* **1997**, *7*, 1069-1074.

36. Qin, D.; Xia, Y.; Whitesides, G. M. *Nature Protoc.* **2010**, *5*, 491-502.
37. Fredonnet, J.; Foncy, J.; Cau, J. C.; Severac, C.; Francois, J. M.; Trevisiol, E. *Microarrays* **2016**, *5*.
38. Lange, S. A.; Benes, V.; Kern, D. P.; Hörber, J. K. H.; Bernard, A. *Anal. Chem.* **2004**, *76*, 1641-1647.
39. Coyle, B. L.; Baneyx, F. *Chem. Commun.* **2016**, *52*, 7001-7004.
40. Hu, S.; Chen, T. H.; Zhao, Y.; Wang, Z.; Lam, R. H. W. *Langmuir* **2018**, *34*, 1750-1759.
41. Khadpekar, A. J.; Khan, M.; Sose, A.; Majumder, A. *Sci. Rep.* **2019**, *9*, 1024.
42. Kilian, K. A.; Bugarija, B.; Lahn, B. T.; Mrksich, M. *Proc. Natl. Acad. Sci. USA* **2010**, *107*, 4872-4877.
43. Hondrich, T. J. J.; Deussen, O.; Grannemann, C.; Brinkmann, D.; Offenhausser, A. *Micromachines* **2019**, *10*, 659.
44. Vonhoren, B.; Roling, O.; Buten, C.; Korsgen, M.; Arlinghaus, H. F.; Ravoo, B. J. *Langmuir* **2016**, *32*, 2277-2282.
45. Lee, S. H.; Rho, W. Y.; Park, S. J.; Kim, J.; Kwon, O. S.; Jun, B. H. *Sci. Rep.* **2018**, *8*, 16763.
46. Benor, A.; Tamang, A.; Wagner, V.; Salleo, A.; Knipp, D. *MRS Adv.* **2019**, *4*, 2441-2451.
47. Zhuang, J.-L.; Zhang, Y.; Liu, X.-Y.; Wang, C.; Mao, H.-L.; Du, X.; Tang, J. *Appl. Surf. Sci.* **2019**, *469*, 90-97.
48. Santhanam, V.; Andres, R. P. *Nano Lett.* **2004**, *4*, 41-44.

49. Han, S.-T.; Zhou, Y.; Xu, Z.-X.; Huang, L.-B.; Yang, X.-B.; Roy, V. A. L. *Adv. Mater.* **2012**, *24*, 3556-3561.
50. Anker, J. N.; Hall, W. P.; Lyandres, O.; Shah, N. C.; Zhao, J.; Van Duyne, R. P. *Nat. Mater.* **2008**, *7*, 442-453.
51. Dreaden, E. C.; Alkilany, A. M.; Huang, X.; Murphy, C. J.; El-Sayed, M. A. *Chem. Soc. Rev.* **2012**, *41*, 2740-2779.
52. Vogele, K.; List, J.; Pardatscher, G.; Holland, N. B.; Simmel, F. C.; Pirzer, T. *ACS Nano* **2016**, *10*, 11377-11384.
53. Li, Y.; Zhang, W.; Hu, J.; Wang, Y.; Feng, X.; Du, W.; Guo, M.; Liu, B.-F. *Adv. Funct. Mater.* **2017**, *27*, 1606045.
54. Atwater, H. A.; Polman, A. Plasmonics for improved photovoltaic devices. In *Materials for Sustainable Energy*, Co-Published with Macmillan Publishers Ltd, UK: 2010; pp 1-11.
55. Matricardi, C.; Hanske, C.; Garcia-Pomar, J. L.; Langer, J.; Mihi, A.; Liz-Marzán, L. M. *ACS Nano* **2018**, *12*, 8531-8539.
56. Zhu, H.; Lussier, F.; Ducrot, C.; Bourque, M.-J.; Spatz, J. P.; Cui, W.; Yu, L.; Peng, W.; Trudeau, L.-É.; Bazuin, C. G.; Masson, J.-F. *ACS Appl. Mater. Interfaces* **2019**, *11*, 4373-4384.
57. Zhu, H.; Masson, J.-F.; Bazuin, C. G. *Langmuir* **2019**, *35*, 5114-5124.
58. Aizawa, M.; Buriak, J. M. *Chem. Mater.* **2007**, *19*, 5090-5101.
59. Liu, Z.; Chang, T.; Huang, H.; He, T. *RSC Adv.* **2013**, *3*, 20464-20470.
60. Onses, M. S.; Wan, L.; Liu, X.; Kiremitler, N. B.; Yilmaz, H.; Nealey, P. F. *ACS Macro Lett.* **2015**, *4*, 1356-1361.

61. Lee, W.; Lee, S. Y.; Briber, R. M.; Rabin, O. *Adv. Funct. Mater.* **2011**, *21*, 3424-3429.
62. Frens, G. *Nat. Phys. Sci.* **1973**, *241*, 20-22.
63. Li, J.; Wu, J.; Zhang, X.; Liu, Y.; Zhou, D.; Sun, H.; Zhang, H.; Yang, B. *J. Phys. Chem. C* **2011**, *115*, 3630-3637.
64. Khlebtsov, B. N.; Khlebtsov, N. G. *J. Phys. Chem. C* **2007**, *111*, 11516-11527.
65. Nehl, C. L.; Hafner, J. H. *J. Mater. Chem.* **2008**, *18*, 2415-2419.
66. Kim, F.; Song, J. H.; Yang, P. *J. Am. Chem. Soc.* **2002**, *124*, 14316-14317.
67. Huang, C.-J.; Wang, Y.-H.; Chiu, P.-H.; Shih, M.-C.; Meen, T.-H. *Mater. Lett.* **2006**, *60*, 1896-1900.
68. Senthil Kumar, P.; Pastoriza-Santos, I.; Rodríguez-González, B.; Javier García de Abajo, F.; Liz-Marzán, L. M. *Nanotechnology* **2007**, *19*, 015606.
69. Shao, Y.; Jin, Y.; Dong, S. *Chem. Commun.* **2004**, 1104-1105.
70. Millstone, J. E.; Park, S.; Shuford, K. L.; Qin, L.; Schatz, G. C.; Mirkin, C. A. *J. Am. Chem. Soc.* **2005**, *127*, 5312-5313.
71. Nehl, C. L.; Liao, H.; Hafner, J. H. *Nano Lett.* **2006**, *6*, 683-688.
72. Hao, F.; Nehl, C. L.; Hafner, J. H.; Nordlander, P. *Nano Lett.* **2007**, *7*, 729-732.
73. Skadtchenko, B. O.; Aroca, R. *Spectrochim. Acta A* **2001**, *57*, 1009-1016.
74. Yang, J.; Wang, X.-Y.; Zhou, L.; Lu, F.; Cai, N.; Li, J.-M. *J. Saudi Chem. Soc.* **2019**, *23*, 887-895.

75. Wallace, G. Q.; Tabatabaei, M.; Lagugné-Labarthe, F. *Can. J. Chem.* **2013**, *92*, 1-8.
76. Liebig, F.; Sarhan, R. M.; Prietzel, C.; Thünemann, A. F.; Bargheer, M.; Koetz, J. *Langmuir* **2018**, *34*, 4584-4594.
77. Sarhan, R. M.; Koopman, W.; Schuetz, R.; Schmid, T.; Liebig, F.; Koetz, J.; Bargheer, M. *Sci. Rep.* **2019**, *9*, 3060-3060.
78. Veres, M.; Füle, M.; Tóth, S.; Koós, M.; Pócsik, I. *Diam. Relat. Mater.* **2004**, *13*, 1412-1415.
79. Kudelski, A.; Pettinger, B. *Chem. Phys. Lett.* **2000**, *321*, 356-362.
80. Zhang, X.; Zhang, J.; Quan, J.; Wang, N.; Zhu, Y. *Analyst* **2016**, *141*, 5527-5534.

Chapter 5

5 Conclusions and Outlook

In this thesis, two projects were presented, each exploring key approaches to the functionalization, chemical modification, and spectroscopic characterization of gold surfaces. First, a new methodology was presented for controllably altering the surface chemistry of functionalized gold substrates through photo-enabled interfacial SPAAC reactions. Separately, novel LSPR-supporting substrates micropatterned with AuNPs were designed and fabricated, and the plasmon-mediated reduction of aryl diazonium salts was investigated.

A general introduction to surface chemistry research and its far-reaching applications is provided. The relevance of both click reactions and plasmon-mediated reactions with respect to their utility in modifying and controlling surface chemistry are discussed with examples, highlighting prominent recent works within the field. Following this discussion, comprehensive descriptions and background are given for select surface modification methodologies including self-assembled monolayers, microcontact printing, click chemistry, and plasmon-mediated chemistry. Further, the fundamental physical and theoretical principles of plasmonics, Raman spectroscopy, SERS, and PM-IRRAS are explained.

The third chapter of this thesis sees several SPAAC reactions applied as tools for fine-tuning the surface chemistry of flat gold substrates, supported by characterization using PM-IRRAS and contact angle measurements. An improved methodology was developed for modifying and controlling the surface properties of these gold substrates through photo-enabled interfacial SPAAC reactions. Using this chemical system, SAMs on flat gold substrates were successfully derivatized with a series of model azides with varied hydrophobicities to specifically induce changes in the surface hydrophobicity of the gold substrates. These changes were reflected in both PM-IRRAS measurements and contact angle measurements. Additionally, the same methodology was employed to functionalize flat gold substrates with azide-modified peptides for use in cell adhesion studies. Cells

were found to adhere well to the modified gold substrates while retaining the spindle-shaped and elongated morphology exhibited by typical human fibroblast cells in their native environment. This acts as a proof-of-concept experiment to demonstrate the general suitability of the interfacial SPAAC reaction process for biochemical applications.

In Chapter 4, the plasmon-driven grafting of aryl diazonium salts onto gold nanostructure surfaces is investigated. Microcontact printing was used to fabricate LSPR-supporting platforms by patterning AuNPs into microscale parallel lines modelled after a diffraction grating. To confirm their plasmon activity, patterned substrates were functionalized with 4-NTP and their surfaces were mapped using SERS, showing strong Raman signals associated with 4-NTP in regions of the substrate covered with AuNPs. Aryl thin films were then locally grafted onto the patterned AuNPs via plasmon-mediated reduction of 4-NBD under laser irradiation. Grafting of the thin films was confirmed by SEM.

The newly devised interfacial SPAAC reaction methodology for functionalizing planar gold surfaces presented here can potentially find use in more widespread applications. Future work may seek to incorporate into this SPAAC reaction system a “double-click” functionality similar to the reaction sequence previously proposed by the Workentin group,¹ wherein the SPAAC click reaction is used in tandem with a modified Staudinger reaction²⁻³ between aryl phosphines and perfluoroaryl azides to accomplish multiple ligations within a single moiety. This would allow even greater control over surface chemistry.

While in this thesis the surface SPAAC reaction system was used to functionalized gold substrates with RGD peptides for cell adhesion experiments, this click methodology going forward could ostensibly be employed to prepare metal surface for a range of biochemical or sensing applications. For example, AuNPs functionalized with carbohydrate molecules, referred to as “glyco-gold nanoparticles” or GAuNPs, are often used to study carbohydrate-carbohydrate and carbohydrate-protein interactions, and associated biological processes.⁴⁻⁵ Recently, alkyne-azide click chemistry has become an attractive approach to synthesizing GAuNPs, and the interfacial SPAAC reaction system

reported here could lend itself very well to this purpose while also helping to overcome some of the drawbacks associated with the CuAAC, such as nanoparticle aggregation.^{4,6-7}

The plasmon-mediated grafting of diazonium salts to surfaces patterned with gold nanostructures requires further in-depth investigation. This includes optimizing grafting parameters to prevent burning and control thin film growth, improving characterization through SERS and other detection methods, as well as pursuing more detailed elucidation of the grafting mechanism. To fully understand the mechanistic reaction pathway, it is important to determine the contributions of hot electron donation, local EM field enhancements, and local heating effects to the progress of the reaction, as any combination of these plasmonic effects may play a role in the overall grafting process.

It is also a possibility to explore the grafting of diazonium salts onto AuNPs stamped in a variety of different patterns. This is interesting because the locations of the plasmonic hot spots can be manipulated by changes to the interparticle distances and to the polarization of the excitation laser. Numerous variations of patterns are achievable with microcontact printing, down to 500 nm resolution.⁸ Thus, by utilizing different patterns and varying the incident laser polarization, the grafting can be controllably localized to different areas of a patterned substrate. This also presents the opportunity for multi-functionalization of AuNP-patterned substrate surfaces. As mentioned in Chapter 4.1, multi-functionalization of metallic nanostructures via the plasmon-mediated reduction of diazonium salts has been previously demonstrated by Felidj *et al.*, who were able to graft two different diazonium-derived molecules in a regiospecific manner to different sides of gold nanodisks simply by changing the polarization of the incident laser used for grafting.⁹ Similarly, in the work presented in this thesis, the aim moving forward is to fabricate patterned substrates suitable for multi-functionalization, and to graft multiple different diazonium-derived chemical species to the surface. One possibility is to fabricate a substrate with AuNPs patterned in a grid configuration by printing the surface with a grating stamp twice, turning the stamp 90° before printing the second time to create perpendicular crisscrossing lines on the surface. Such grid-patterned substrates, along with substrates patterned with concentric rings created using a circular grating as the master pattern, have in fact already been successfully constructed, as shown in Figure

5.1. Hypothetically, by aligning the polarization of the grafting laser with only one set of lines in the grid at a time, it may be possible to graft different molecules along the lines in different directions.

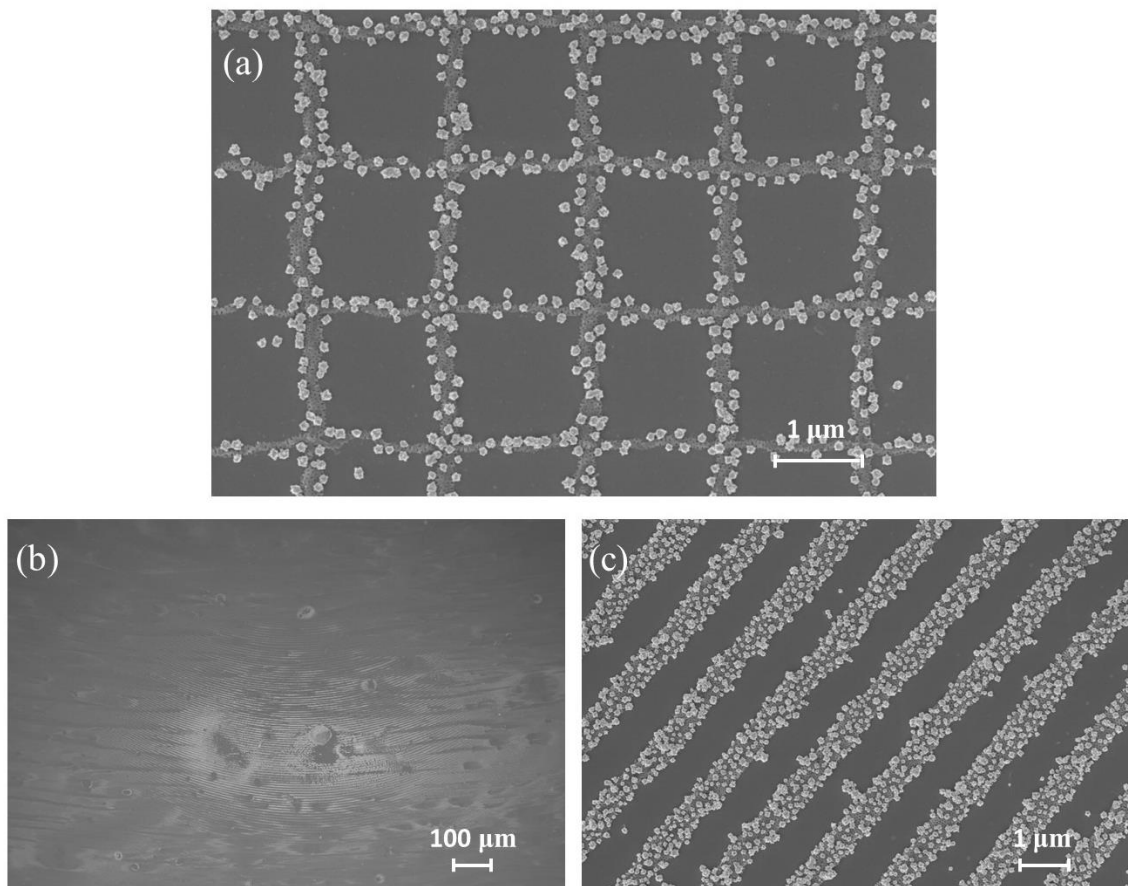


Figure 5.1: (a) SEM image of a substrate with raspberry-like AuNPs printed into a grid pattern; SEM images of a substrate with raspberry-like AuNPs printed into a pattern of concentric rings (b) at a low magnification, to show the curvature of the rings, and (c) at a higher magnification.

Such multi-functionalized surfaces have potential applications in molecular sensing and biosensing. The grafted films may be further modified with receptor molecules designed to recognize a specific target analyte. This may also serve to improve SERS detection as the grafting, and subsequently the analyte binding, would only occur in regions that align with plasmonic hot spots, where SERS sensitivity is greatest.⁹ One possible approach toward post-functionalization of the diazonium-derived thin films could be to use azide-

terminated diazonium salts that, once plasmonically grafted, may undergo alkyne-azide click reactions with alkyne-containing organic or biological molecules. In this way, plasmon-mediated chemistry and click chemistry may be combined for the spatially controlled chemical surface modification and, potentially, multi-functionalization of plasmonically active metallic nanoparticles. This idea represents another promising direction for the future of this research.

Control over surface chemistry is critical to many fields in science and in industry, such as electronics,¹⁰ molecular sensing,¹¹ surface protective coatings,¹² medical technology,¹³ and more. Ultimately, this work seeks to diversify and expand upon the current repository of surface modification techniques and strategies.

5.1 References

1. Luo, W.; Luo, J.; Popik, V. V.; Workentin, M. S. *Bioconjugate Chem.* **2019**, *30*, 1140-1149.
2. Sundhoro, M.; Jeon, S.; Park, J.; Ramström, O.; Yan, M. *Angew. Chem. Int. Ed.* **2017**, *56*, 12117-12121.
3. Lin, F.L.; Hoyt, H.M.; van Halbeek, H.; Bergman, R.G.; Bertozzi, C.R. *J. Am. Chem. Soc.* **2005**, *127*, 2686-2695.
4. Poonthiyil, V.; Lindhors, T.K.; Golovko, V.B.; Fairbanks, A.j. *Beilstein J. Org. Chem.* **2018**, *14*, 11-24.
5. Compostella, F.; Pitirollo, O.; Silvestri, A.; Polito, L. *Beilstein J. Org. Chem.* **2017**, *13*, 1008-1021.
6. He, X.-P.; Hu, X.-L.; Jin, H.-Y.; Gan, J.; Zhu, H.; Li, J.; Long, Y.-T.; Tian, H. *Anal. Chem.* **2015**, *87*, 9078-9083.
7. Gobbo, P.; Mossman, Z.; Nazemi, A.; Niaux, A.; Biesinger, M.C.; Gillies, E.R.; Workentin, M.S. *J. Mater. Chem. B* **2013**, *2*, 1764-1769.

8. Perl, A.; Reinhoudt, D.N.; Huskens, J. *Adv. Mater.* **2009**, *21*, 2257-2268.
9. Tijunelyte, I.; Kherbouche, I.; Gam-Derouich, S.; Nguyen, M.; Lidgi-Guigui, N.; Lamy de la Chapelle, M.; Lamouri, A.; Lévi, G.; Aubard, J.; Chevillot-Biraud, A.; Mangeney, C.; Felidj, N. *Nanoscale Horiz.* **2018**, *3*, 53-57.
10. Schmitz, J. *Surf. Coat. Tech.* **2018**, *343*, 83-88.
11. D'Orazio, P. *Clin. Chim. Acta* **2003**, *334*, 41-69.
12. Hong, S.H.; Hond, S.; Ryou, M.-H.; Choi, J.W.; Kang, S.M.; Lee, H. *Adv. Mater. Interfaces* **2016**, *3*, 1500857.
13. Lopes, T.S.; Gomes, A.; Pereira, M.R.; Granjeiro, J.M.; Leite, P.E.C. *J. Cell. Biochem.* **2019**, *120*, 16370-16378.

Appendix A – Details for PM-IRRAS Spectral Calibration

The PM-IRRAS calibration procedure used in this thesis is adapted from the protocol developed by Buffeteau *et al.*¹⁻³ For each PM-IRRAS measurement, the experimental PM-IRRAS signal received by the detector is sent to an electronic filter that splits the signal into two distinct sets of data, given by:

$$I_{DC} = \frac{C_{DC}I_0^p(\omega_i)}{2} \times \left[\left(R_p(d) + R_s(d) \right) + \left(R_p(d) - R_s(d) \right) J_0(\varphi_0) \right] \quad (S1)$$

which describes the low frequency component of the signal that is modulated only at the Fourier frequencies ω_i introduced by the Michelson interferometer, and

$$I_{AC} = C_{AC}I_0^p(\omega_i) \times \left[\left(R_p(d) - R_s(d) \right) \times J_2(\varphi_0) \times \cos(2\omega_m t) \right] \quad (S2)$$

which describes the high frequency component of the signal that is modulated at the Fourier frequencies ω_i as well as the frequencies ω_m introduced by the photoelastic modulator (PEM), which modulates the polarization of incident light.² Here, $R_p(d)$ and $R_s(d)$ are the reflectances of the substrate with p-polarized light and s-polarized light, respectively, at film thickness d ; $J_0(\varphi_0)$ and $J_2(\varphi_0)$ represent the zero- and second-order Bessel functions of the maximum dephasing φ_0 introduced by the PEM; $I_0^p(\omega_i)$ is the intensity of the p-polarized IR beam of frequency ω_i after passing through the polarizer attached to the PEM; and C_{DC} and C_{AC} are constants that account for the gain and demodulation adjustments applied during electronic processing of the signal. “AC” and “DC” are the accepted designations for the electronically filtered signals because the high frequency signal oscillates at a much faster rate than the low frequency signal, analogous to alternating and direct current electricity.

After electronic filtering, the doubly modulated AC signal is demodulated by a lock-in amplifier (LIA). Demodulation of the I_{AC} signal by the removes the $\cos(2\omega_m t)$ term from equation (S2), and then the I_{DC} signal and the demodulated I_{AC} signal are plotted as two separate spectra. To obtain from these data the “theoretical” PM-IRRAS signal, the ratio of the two spectra are taken by dividing equation (S2) by equation (S1):

$$S_{PM-IRRAS} = \frac{I_{AC}}{I_{DC}} = \frac{2G \cdot |(R_p(d) - R_s(d)) \cdot J_2(\varphi_0)|}{(R_p(d) + R_s(d)) + (R_p(d) - R_s(d)) \cdot J_0(\varphi_0)} \quad (S3)$$

where $G = \frac{c_{AC}}{c_{DC}} = 10 \left(\frac{G_{AC}}{S \cdot G_{DC}} \right) [\exp(-2V\bar{\nu}\tau)]$ is a gain factor that accounts for the different amplifications, G_{AC} and G_{DC} , on the two channels, the sensitivity, S , the optical mirror velocity, V , the wavenumber, $\bar{\nu}$, and the time constant, τ .²⁻³

Highly reflective gold mirror substrates are used for all PM-IRRAS experiments in this study, so in this case $[R_p(d) + R_s(d)]$ is much greater than $[R_p(d) - R_s(d)]$, $R_s(d)$ is greater than $R_p(d)$, and the term $J_0(\varphi_0)$ is less than 1. Therefore, it is reasonable to neglect $[R_p(d) - R_s(d)] \cdot J_0(\varphi_0)$ and equation (S3) becomes:³

$$S_{PM-IRRAS} = 2GJ_2(\varphi_0) \frac{R_s(d) - R_p(d)}{R_p(d) + R_s(d)} \quad (S4)$$

From equation (S4), Buffeteau *et al.* were able to derive the following expression of the theoretical PM-IRRAS signal:

$$S_{PM-IRRAS} = S_{sub} + S_{film} = 2GJ_2(\varphi_0) \frac{R_s(0) - R_p(0)}{R_p(0) + R_s(0)} + GJ_2(\varphi_0) \frac{16\pi\bar{\nu}k d \sin^2\theta}{n^3 \cos\theta} \quad (S5)$$

where $R_p(0)$ and $R_s(0)$ are the reflectances of the bare substrate with p- and s-polarized light, respectively, k is the extinction coefficient of the film, θ is the angle of the incident light, and n is the refractive index of the film.³

The expression of the PM-IRRAS signal represented in equation (S5) contains two terms, the first of which, $S_{sub} = 2GJ_2(\varphi_0) \frac{R_s(0) - R_p(0)}{R_p(0) + R_s(0)}$, corresponds to the contribution of the gold substrate to the PM-IRRAS spectrum, and the second of which, $S_{film} = GJ_2(\varphi_0) \frac{16\pi\bar{\nu}k d \sin^2\theta}{n^3 \cos\theta}$, corresponds to the contribution of the thin film to the PM-IRRAS spectrum.³

It is essential to account for the Bessel functions introduced during I_{AC} demodulation with the LIA by applying the PM-IRRAS calibration procedure. As previously mentioned, the calibration procedure is designed to allow the complex PM-IRRAS signal to be expressed

as the more conventional IRRAS spectrum, which is often represented as a *pseudo*-absorption spectrum of the thin film, according to the following equation:¹⁻⁴

$$A(d) = 1 - \frac{R_p(d)}{R_p(0)} \quad (\text{S6})$$

where $A(d)$ represents the absorbance of the sample with film thickness d .

From equation (S5), the PM-IRRAS *pseudo*-absorption spectrum may be expressed by the following equation:³

$$A(d) = 1 - \frac{R_p(d)}{R_p(0)} = \frac{16\pi\bar{\nu}kd\sin^2\theta}{n^3\cos\theta} = \frac{S_{film}}{GJ_2(\varphi_0)} \quad (\text{S7})$$

The contribution of the thin film to the PM-IRRAS spectrum can be calculated from rearrangement of equation (S5): $S_{film} = S_{PM-IRRAS} - S_{sub}$. Following this calculation, the calibration spectra C_{pp} and C_{ps} must be obtained. These calibration spectra are obtained by placing a linear polarizer between the bare substrate and the detector. C_{pp} is obtained by orienting the polarizer to select for p-polarized light, and C_{ps} is obtained by orienting the polarizer to select for s-polarized light. C_{pp} and C_{ps} are expressed by equating $R_s(d)$ and then $R_p(d)$, respectively, to 0 in equation (S3).³ This yields:

$$C_{pp} = \frac{2G' \cdot |J_2|}{1+J_0} \quad (\text{S8a})$$

and

$$C_{ps} = \frac{2G' \cdot |J_2|}{1-J_0} \quad (\text{S8b})$$

where G' is the gain factor for the calibration spectra. G and G' differ because calibration measurements and normal PM-IRRAS measurements typically require different experimental conditions. Equations (S8a) and (S8b) can be combined and then multiplied by G in order to calculate GJ_2 :


$$GJ_2(\varphi_0) = \frac{G}{G'} \cdot \frac{C_{pp}C_{ps}}{C_{pp}+C_{ps}} \quad (\text{S9})$$

To obtain the final calibrated PM-IRRAS absorption spectrum, the calculated value for S_{film} is divided by equation (S9), in accordance with equation (S7).

References

1. Buffeteau, T.; Desbat, B.; Turlet, J.M. *Appl. Spec.* **1991**, *45*, 380-389.
2. Buffeteau, T.; Desbat, B.; Blaudez, D.; Turlet, J.M. *Appl. Spec.* **2000**, *54*, 1646-1650.
3. Ramin, M.A.; Le Bourdon, G.; Daugey, N.; Bennetau, B.; Vellutini, L.; Buffeteau, T. *Langmuir* **2011**, *27*, 6076-6084.
4. Tolstoy, V.P.; Chernyshova, I.V.; Skrychevsky, V.A. *Handbook of Infrared Spectroscopy of Ultrathin Films*; John Wiley & Sons, Inc.: New Jersey, 2003, 377-378.

Appendix B – Copyrights



ACS Publications
Most Trusted. Most Cited. Most Read.

Tuning Surface Wettability at the Submicron-Scale: Effect of Focused Ion Beam Irradiation on a Self-Assembled Monolayer

Author: Yutaka Yamada, Koji Takahashi, Tatsuya Ikuta, et al

Publication: The Journal of Physical Chemistry C

Publisher: American Chemical Society

Date: Jan 1, 2016

Copyright © 2016, American Chemical Society


PERMISSION/LICENSE IS GRANTED FOR YOUR ORDER AT NO CHARGE

This type of permission/license, instead of the standard Terms & Conditions, is sent to you because no fee is being charged for your order. Please note the following:

- Permission is granted for your request in both print and electronic formats, and translations.
- If figures and/or tables were requested, they may be adapted or used in part.
- Please print this page for your records and send a copy of it to your publisher/graduate school.
- Appropriate credit for the requested material should be given as follows: "Reprinted (adapted) with permission from (COMPLETE REFERENCE CITATION). Copyright (YEAR) American Chemical Society." Insert appropriate information in place of the capitalized words.
- One-time permission is granted only for the use specified in your request. No additional uses are granted (such as derivative works or other editions). For any other uses, please submit a new request.

If credit is given to another source for the material you requested, permission must be obtained from that source.

BACK
CLOSE WINDOW



ACS Publications
Most Trusted. Most Cited. Most Read.

Dual-Bioorthogonal Molecular Tool: "Click-to-Release" and "Double-Click" Reactivity on Small Molecules and Material Surfaces

Author: Wilson Luo, Johnny Luo, Vladimir V. Popik, et al

Publication: Bioconjugate Chemistry

Publisher: American Chemical Society

Date: Apr 1, 2019

Copyright © 2019, American Chemical Society

PERMISSION/LICENSE IS GRANTED FOR YOUR ORDER AT NO CHARGE

This type of permission/license, instead of the standard Terms & Conditions, is sent to you because no fee is being charged for your order. Please note the following:

- Permission is granted for your request in both print and electronic formats, and translations.
- If figures and/or tables were requested, they may be adapted or used in part.
- Please print this page for your records and send a copy of it to your publisher/graduate school.
- Appropriate credit for the requested material should be given as follows: "Reprinted (adapted) with permission from (COMPLETE REFERENCE CITATION). Copyright (YEAR) American Chemical Society." Insert appropriate information in place of the capitalized words.
- One-time permission is granted only for the use specified in your request. No additional uses are granted (such as derivative works or other editions). For any other uses, please submit a new request.

If credit is given to another source for the material you requested, permission must be obtained from that source.

BACK
CLOSE WINDOW

Regarding Incident 3680303 Request Permission to Reprint Published Material

support@services.acs.org <support@services.acs.org>

Thu 2020-07-16 12:48 PM

To: Sydney Marlise Legge <slegge4@uwo.ca>



Dear Sydney,

Your permission requested is granted and there is no fee for this reuse.

In your planned reuse, you must cite the ACS article as the source, add this direct link: <<https://pubs.acs.org/doi/abs/10.1021/acsomega.7b00394>>, and include a notice to readers that further permission related to the material excerpted should be directed to the ACS.

Please do not hesitate to contact me if you need any further assistance.

Regards,
Jawwad Saeed
ACS Customer Services & Information
<https://help.acs.org>

Incident Information:

Incident #: 3680303
Date Created: 2020-07-16T11:40:16
Priority: 3
Customer: Sydney Marlise Legge
Title: Request Permission to Reprint Published Material
Description: Dear Permissions Representative,

I am in the process of completing a Masters thesis at the University of Western Ontario. I am writing to request permission to reprint material from the following publication:

Nguyen, V.-Q.; Ai, Y.; Martin, P.; Lacroix, J.-C. Plasmon-induced nanolocalized reduction of diazonium salts ACS Omega 2017, 2, 1947-1955.
<https://pubs.acs.org/doi/abs/10.1021/acsomega.7b00394>

I intend to reuse one figure (Figure 4c on page 1951) from this work, to be printed (both in-print and electronic formats) in my M.Sc. thesis (requestor type: university/academic).

The requested permission extends to any future revisions and editions of my thesis, including non-exclusive world rights in all languages, and to the electronic publication of my thesis by the University of Western Ontario. These rights will in no way restrict republication of the material in any other form by you or by others authorised by you. If you do not control the copyright on the above mentioned material, I would appreciate any contact information you can give me regarding the proper rights holder(s). Otherwise, your permission confirms that you hold the right to grant the permission requested here. Please respond in writing to indicate whether permission is granted and inform me of any fees or conditions that may be required. In addition to the terms of agreement, please also indicate how you wish to be credited.

I would greatly appreciate your consent to my request. If you require any additional information, please do not hesitate to contact me. Thank you for your time and consideration of this request. I look forward to hearing back from you at your earliest convenience.

Best,

Sydney Legge
M.Sc. Candidate
University of Western Ontario



Two-Color Single Hybrid Plasmonic Nanoemitters with Real Time Switchable Dominant Emission Wavelength

Author: Xuan Zhou, Jérémie Wenger, Francesco N. Viscomi, et al

Publication: Nano Letters

Publisher: American Chemical Society

Date: Nov 1, 2015

Copyright © 2015, American Chemical Society

PERMISSION/LICENSE IS GRANTED FOR YOUR ORDER AT NO CHARGE

This type of permission/license, instead of the standard Terms & Conditions, is sent to you because no fee is being charged for your order. Please note the following:

- Permission is granted for your request in both print and electronic formats, and translations.
 - If figures and/or tables were requested, they may be adapted or used in part.
 - Please print this page for your records and send a copy of it to your publisher/graduate school.
 - Appropriate credit for the requested material should be given as follows: "Reprinted (adapted) with permission from (COMPLETE REFERENCE CITATION). Copyright (YEAR) American Chemical Society." Insert appropriate information in place of the capitalized words.
 - One-time permission is granted only for the use specified in your request. No additional uses are granted (such as derivative works or other editions). For any other uses, please submit a new request.
- If credit is given to another source for the material you requested, permission must be obtained from that source.

BACK

CLOSE WINDOW



Investigation of Au SAMs Photoclick Derivatization by PM-IRRAS

Author: Wilson Luo, Sydney M. Legge, Johnny Luo, et al

Publication: Langmuir

Publisher: American Chemical Society

Date: Feb 1, 2020

Copyright © 2020, American Chemical Society

PERMISSION/LICENSE IS GRANTED FOR YOUR ORDER AT NO CHARGE

This type of permission/license, instead of the standard Terms & Conditions, is sent to you because no fee is being charged for your order. Please note the following:

- Permission is granted for your request in both print and electronic formats, and translations.
- If figures and/or tables were requested, they may be adapted or used in part.
- Please print this page for your records and send a copy of it to your publisher/graduate school.
- Appropriate credit for the requested material should be given as follows: "Reprinted (adapted) with permission from (COMPLETE REFERENCE CITATION). Copyright (YEAR) American Chemical Society." Insert appropriate information in place of the capitalized words.
- One-time permission is granted only for the use specified in your request. No additional uses are granted (such as derivative works or other editions). For any other uses, please submit a new request.

BACK

CLOSE WINDOW

Curriculum Vitae

Name: Sydney Legge

Post-secondary Education and Degrees: University of Western Ontario
London, Ontario, Canada
2014-2018 Hons. B.Sc.

The University of Western Ontario
London, Ontario, Canada
2018-2020 M.Sc.

Honours and Awards: 102nd Canadian Chemistry Conference and Exhibition
Awarded First Place in the Graduate Student Poster Competition in the Surface Science Division
2019

46th Southern Ontario Undergraduate Student Chemistry Conference
Awarded First Place for Best Oral Presentation in the Physical, Theoretical, and Computational Chemistry Division
2018

Related Work Experience: Teaching Assistant
The University of Western Ontario
2018-2020

Undergraduate Research Assistant (NSERC USRA)
The University of Western Ontario
May-August 2016,2017,2018

Publications: Luo, W.; Legge, S.; Luo, J.; Lagagné-Labarthet, F.; Workentin, M. Investigation of Au SAMs photoclick derivatization by PM-IRRAS. *Langmuir* **2020**, *36*, 1014-1022.

Conference Contributions: International Conference on Enhanced Spectroscopies (2019)
University of Western Ontario, London, Ontario, Canada
Poster Presentation: Legge, S.; Luo, W.; Workentin, M.; Lagagné-Labarthet, F. PM-IRRAS Investigation of 'Photoclick' Reactions at the Monolayer Level

102nd Canadian Chemistry Conference and Exhibition (2019)

Québec City, Quebec, Canada

Poster Presentation: Legge, S.; Luo, W.; Workentin, M.; Lagagné-Labarhet, F. Probing Surface Click Reaction at the Monolayer Level

46th Southern Ontario Undergraduate Student Chemistry Conference (2018)

Wilfred Laurier University, Waterloo, Ontario, Canada

Oral Presentation (15 minutes): Legge, S.; Luo, W.; Workentin, M.; Lagagné-Labarhet, F. Probing Surface Chemistry at the Monolayer Level with PM-IRRAS